Jellyfish Inspired Underwater Systems and Technologies

COLIN FREDERICK SMITH

Thesis submitted to the faculty of the Virginia Polytechnic Institute and State University
in partial fulfillment of the requirements for the degree of

Master of Science
In
Mechanical Engineering

Committee Chair: Shashank Priya
Committee Member: Donald Leo
Committee Member: Timothy Long

November 18, 2011
Blacksburg, VA

Keywords: jellyfish, biomimetic, unmanned, underwater, vehicle, robotic

Jellyfish Inspired Underwater Systems and Technologies

Colin Frederick Smith

ABSTRACT

Unmanned underwater vehicles (UUVs) have long been in use but increasingly there has been a wave of biomimetic robots taking over the duties and functions of traditional vehicles. A robotic jellyfish, inspired by the species *Aurelia aurita* was developed and characterized. In addition to the body of the main robotic vehicle, supporting technologies were developed including polymeric artificial muscles, hydrogel-based artificial mesoglea, and an inclinometer inspired by the jellyfish statocyst organ. Through multiple versions, the vehicle was able to attain an order of magnitude increase in proficiency from 0.022 s^{-1} to 0.21 s^{-1} and robustness not found in initial prototypes. A polyvinyl alcohol hydrogel reinforced with ferritin nanoparticles was found to accurately mimic the stress and strain characteristics of natural *Aurelia* mesoglea while maintaining a high water content similar to the animal. In addition, the optical properties were shown to be controlled by water to DMSO ratio. A five layer PPy-Au-PVDF-Au-PPy actuator stored in 0.5M KCl solution actuated at 4 VDC potential and produced an impressive 90% tip deflection. In addition, the rate of change was extremely high at 50% deflection of initial actuator length per second. The artificial jellyfish statocyst was found to produce the required highly linear voltage divider output. This sensor will provide the vehicle with biomimetic self-awareness of its own body position. Future directions are proposed for the biomimetic robotic jellyfish such as on-board power and computing, multi-material mesoglea with a dermal layer, a MEMS-based statocyst, and polymeric muscles with increased force production and time response.

Acknowledgements

No body of work can be a sole effort and with that I would like to thank the multitude of people that helped me produce this document.

First of all I would like to thank my advisor Dr. Priya for his guidance and support over the last three years. None of this would have been possible without his vision and dedication to all of his students, including myself. Somehow you manage to have to time to help with research problems, edit papers, write proposals, and make sure everyone's personal lives are in order, all at once. For this I am grateful.

I would also like to thank my parents, Richard Smith and Marti Schweitzer, for their constant care throughout all of my graduate education. I know how much respect and admiration they have for academia and their advice and encouragement led me to where I am today.

My support network was always my friends and roommates when I needed to take a break from research and clear my head. With that I would like to thank Reza Soltan, Ryan Colby, Jackie Speier, Lera Oscherov, Tyler Satre, Carlos Guevara, and Brian Goode.

Over the years I collaborated with many people from the Center for Intelligent Material Systems and Structures including Alex Villanueva, Keyur Joshi, Colin Stewart, Yonas Tadesse, Su Chul Yang, Nick Thayer, Scott Bressers, Tony Marin and Aram Lee from the Center for Photonics Technology. I also had the pleasure of working with some very dedicated undergraduate students. Without the help of Zachery Vergiels, Jason Jones, Will Gerig, and Hilary McGown, many parts of this work would not have been possible.

Thank you!

Contents

List of figures

List of tables

Introduction

Unmanned underwater vehicles (UUVs) serve a valuable function in monitoring of animals, humans, and environmental activity. Several applications can be cited for small UUVs including monitoring of ocean currents and chemical agents, study of animal migration, depth measurements, and military functions. Current technologies deployed for many of these applications suffer from practical limitations including cost-effectiveness, lifetime, and range. Buoys deployed in deep ocean environments are normally tethered and thus have limited operation range. The typically passive, distributed, battery operated wireless sensor nodes are not desirable as they have limited station-keeping capability and fixed lifetime. Large vehicles such as submarines and boats require high operating costs. These large vehicles can also be intrusive to the natural habitat and disturb the course of the local environment.

The goal of our research is to develop an unmanned vehicle that is capable of conducting autonomous surveillance over large distances for extensive periods of time. The strategy adopted to accomplish this goal is to implement methods of undersea propulsion found in biological species. Nature is comprised of a variety of animal designs that show promise for surveillance of undersea environments. They can be mobile and small with various sensory functions, networked as nodes with other units, as well as possess adaptability, maneuverability, and intelligence. The concept of biomimetics has recently been used in the design and fabrication of a wide variety of underwater unmanned vehicles (UUVs). Vehicles have been developed using concepts of squid and jellyfish jet propulsion (Mehensi 2004), lobster and lamprey forms (Ayers 2000), Tadro4 modeled after an electric ray (Long 2011), a turtle "RT-I" (Kato 2011), manta rays (Clark 2006), autonomous robotic fish (Tan 2006), a four-finned vehicle based on the fish *Gomphosus varius* (Kato 2000), and robotic tuna (Triantafyllou 1995).

Out of the broad range of choices, jellyfish were selected due to attributes such as their ability to consume little energy owing to a lower metabolic rate than other marine species (Seibel and Drazen 2007), survivability in varying water conditions, and possession of adequate morphology for carrying payload. Jellyfish inhabit every major oceanic area of the world (Cook 2010) and are capable of withstanding a wide range of temperatures and salinities (Arai 1997). Most species are found in shallow coastal waters, but some have been found in depths of 7,000 meters (Kramp 1959). Furthermore, jellyfish have a wide variety of sizes ranging from a few millimeters to over 2 meters in diameter (Omori and Kitamura 2004) as well as display a multitude of shapes and colors. They have the ability to move vertically but depend mainly upon ocean currents for horizontal movement (Cook 2010). They possess an

elementary nervous system, which consists of receptors capable of detecting touch, light, inclination, and other stimuli (Arai 1997).

Bio-inspired materials and systems research has received significant attention in the last decade. Some examples that demonstrate desired functions and structures are self-cleaning (Bhushan et al. 2008), solar energy harvesting by replicating photosynthesis (Gust et al. 2001), strong adhesives (Lee et al. 2007) and silk including technology for fiber spinning (Lazaris et al. 2002), rapid locomotion in hard to reach places (Menciassi and Dario 2003), hard ceramics for armors (Yasrebi et al. 1990), and self-healing characteristics of the bones and tissue (Trask et al. 2007). These examples reflect upon the possibilities of achieving improved engineering functions by mimicking fundamental mechanisms adopted by nature. In our research, we combine bio-inspiration and biomimetics to achieve the desired combination of proficiency and efficiency.

Aurelia aurita is a type of Scyphozoa found in oceans around the world. The medusa is the adult stage in its life cycle which is commonly referred to as "jellyfish". Jellyfish can be separated into two categories based on their propulsion mechanism. These categories consist of "jetters" which exhibit proficient propulsion and "rowers" which are more efficient swimmers (Colin and Costello 2002). Jetting propulsion consists of water being squeezed out of the bell due to a decrease in volume. On the other hand, rowing propulsion relies on the interaction between starting and stopping vortices that allow a greater body of water to be displaced and therefore produce more thrust (Colin and Costello 2002). For this reason, rowers can reach much bigger dimensions. *A. aurita* is a rower which uses circular muscles located in its subumbrella (Chapman 1999). When the subumbrella muscles undergo deformation cycle (contraction followed by passive relaxation), the water flows out of the bell resulting in the formation of stopping vortex and a starting vortex which are essential to achieve high efficiency (Dabiri et al 2005). Bell diameter for *Aurelia* usually ranges between 5 and 26 cm (Dawson 2003). As discussed later in this paper, there are several structural features which also have significant influence on the propulsive efficiency of the jellyfish.

Advancement in smart material actuators has opened the possibility of designing new propulsion mechanisms that require large stroke for thrust generation. Shape memory alloy (SMA) wire has been shown to exhibit relevant behavior for serving the role of artificial muscles and has been proven in design of underwater vehicles. Some examples of underwater vehicles based on SMA include Jetsum (Villanueva et al. 2009), Micro jelly (Guo et al. 2003, Yang et al. 2007), and squid and fish robots (Wang et al. 2008). SMAs have also been used in design of air vehicles such as BATMAV (Bunget et al. 2008). Bio-inspired shape memory alloy composite (BISMAC) actuators are made of silicone, SMA wires, and

spring steel. These actuators can convert the standard SMA deformation of 4% into a large deflection which can be further tailored by varying design parameters. Recent results from Villanueva et al. (2010a) have shown that BISMAC actuators can reproduce the cross-sectional deformation profile of *A. aurita* In the first part of the chapter, efforts were focused on characterizing the BISMAC performance to achieve full understanding of its capability.

Chapter 1:

Multidirectional swimming control through artificial statocyst

In addition to unmanned underwater vehicles, many other systems need tilt sensors for applications such as vehicle security and safety. There are also multitude of applications of tilt sensor in mobile vehicles such as gold carts and modern personal transporters such as the Segway scooter. The quickly expanding field of mobile robots also has the need for cheap and effective means of measuring vehicle position, inclination, acceleration, and velocity. These needs are not only limited to robotics, but other mobile platforms as well such as underwater and aerial vehicles. Commonly tilt or inclination has been mathematically derived from accelerometers; however there is inherent error in any indirect measurement. As such, it will be extremely helpful to have direct measurement of tilt that the vehicle guidance system can use without extraneous calculations.

Many tilt sensors have been developed over the years using a variety of methods. Recently MEMS technology has been applied towards fabrication of tilt sensors allowing for an explosion of different inclinometer technologies. Figure 1.1 shows examples of tilt sensor technologies including the typical acceleration-based technology. Constandinou and Georgiou (2008) showed a sensor composed of one stationary and one moving part. The moving semicircular mass projects a shadow onto an array of optical sensors. The sensor has a 5 degree resolution up to 300 total degrees of tilt. Jung et al. (2007) described an electrolytic version with a MEMS micromachined cavity and a moving electrolyte. The degree of tilt determines how much of the solution contacts the electrodes producing a varying electrical signal. Tang et al. (2009) produced a structure that responds directly to gravity through the bending of extremely small piezoelectric beams. The sensor was able to achieve 0.025 mV per degree sensitivity. A novel device was constructed that had a single MEMS heater with a silicon bridge to sense the temperature by resistance changes on either side. Due to free convective flow, when the tilt of the sensor changes, so does the temperature felt by each silicon bridge thermometer (Billat et al 2002).

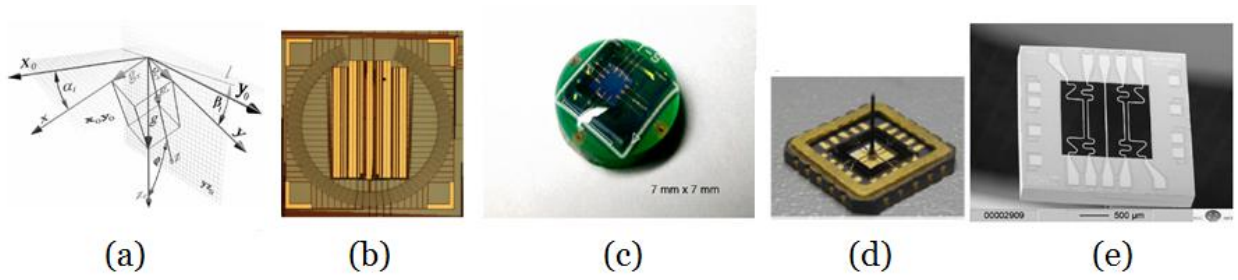

Figure 1.1: Current tilt sensor technologies such as (a) mathematically derived from acceleration (b) opto-mechanical (c) electrolytic (d) piezoresistive (e) thermo-convective

Bio-inspired materials and systems research has received significant attention in the last decade. Some examples that demonstrate desired functions and structures are self-cleaning (Bhushan et al. 2008), solar energy harvesting by replicating photosynthesis (Gust et al. 2001), strong adhesives (Lee et al. 2007) and silk including technology for fiber spinning (Lazaris et al. 2002), rapid locomotion in hard to reach places (Menciassi and Dario 2003), hard ceramics for armors (Yasrebi et al. 1990), and self-healing characteristics of the bones and tissue (Trask et al. 2007). Figure 1.2 shows some of the most well-known examples of biomimicry such as Velcro, sticky gecko feet, antimicrobial shark skin, and water repellant surfaces based on the lotus leaf. These examples reflect upon the possibilities of achieving improved engineering functions by mimicking fundamental mechanisms adopted by nature. Jellyfish (Cnidarians) have no central nervous system (CNS) and they only use a diffused nerve net to control movement. As such it is important for them to have sensory organs that can provide information to the nerve net and affect behaviors such as feeding, mating, and escape from predators. For instance, most jellyfish have simple light-sensors called ocelli. When this sensor sees changes in light intensity, the nerve net is programmed to assume that a predator has just passed over the jellyfish. It then initiates an escape mechanism. Similarly it possess inclinometer in the statocyst organ that can detect pitch or roll. In the center of a ring of cells, a statolith (mineralized ball) pushes against small sensing hairs called setae. This pressure creates a feedback for change in orientation and helps in maintaining the balance (Arai 1997).

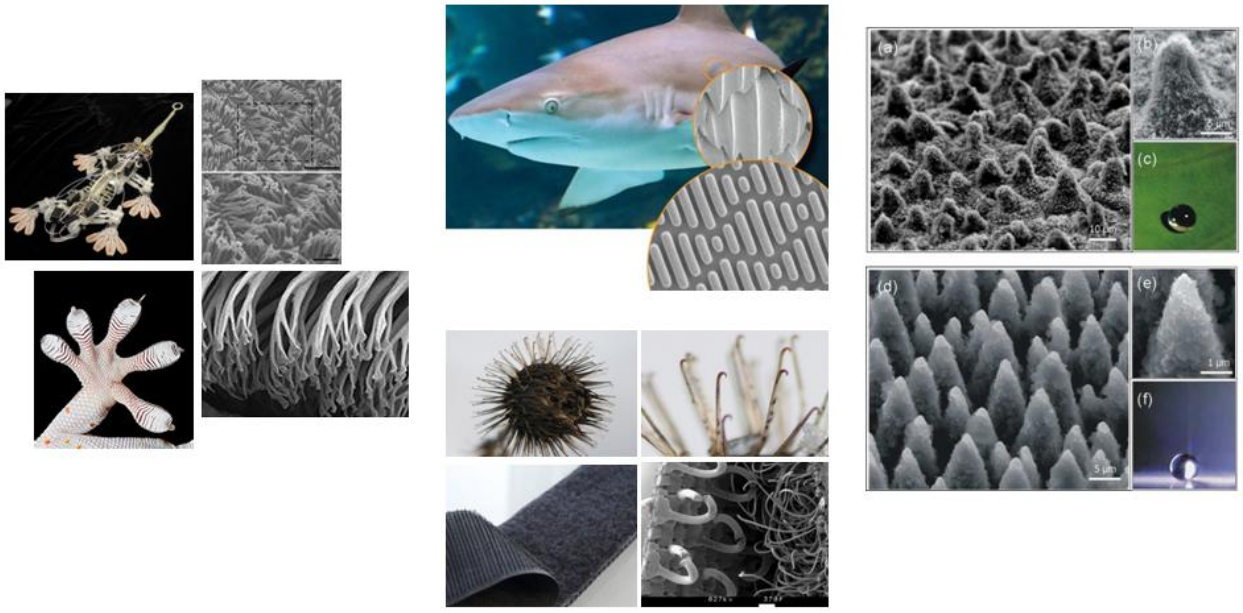

Figure 1.2: Successes of biomimetics such as a gecko robot, antimicrobial shark skin, water repellant lotus leaves, and Velcro based on the burr structure.

1.1 Multidirectional control using COTS compass

Since it was known that the robotic jellyfish vehicle would have to know its tilt and compass heading, a commercial off the shelf solution was first investigated. The Honeywell HMC6343 board was selected due to its small size and convenient I2C bus architecture. The compass works by leveraging 3-axis magneto-resistive sensors and 3-axis MEMS accelerometers. This provides heading, pitch, and roll in a 9 x 9 x 1.9 mm package size. The magnetic nature of this sensor could be considered bio-inspired since magnetoreception has been observed in turtles, lobsters, sharks, and stingrays.

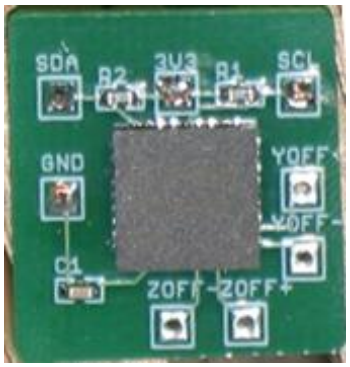

Figure 1.3: HMC6343 on custom created PCB

Figure 1.4 shows the flow diagram of how the data from the COTS sensor flows to the computer. First the tilt sensing occurs and data is stored momentarily in the chip. Then the data is transferred through an I2C bus to a converter that allows the computer to use USB protocol. This COM signal is then run into LabView where the raw data is collected. A LabView VI then stores the data, which can be displayed on the screen in a variety of ways.

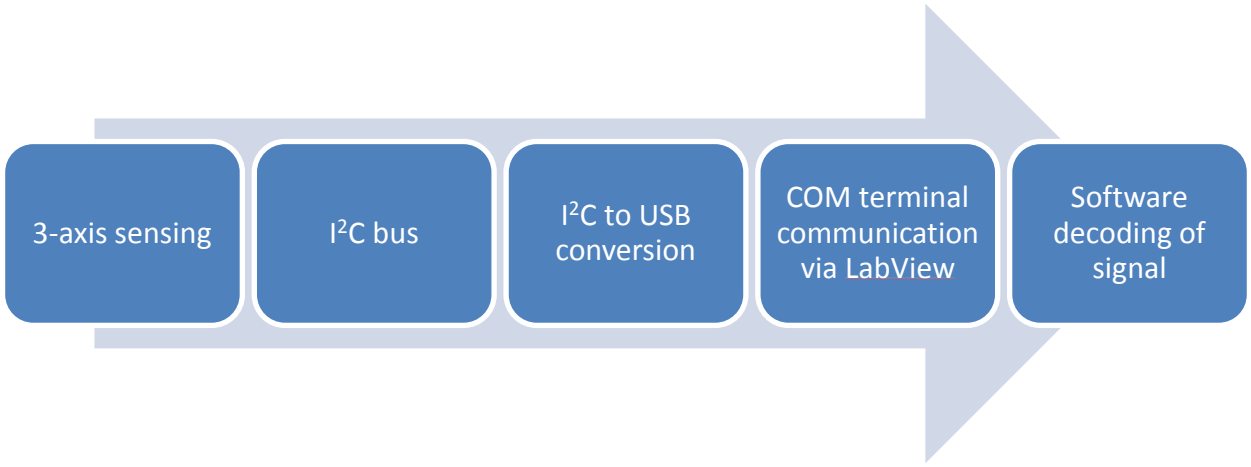

Figure 1.4: Flow chart of data transfer

One of the ways in which tilt, pitch, and yaw data can be displayed is through the use of a 3D jellyfish vehicle model developed as a LabView virtual instrument. On the screen a representation of the jellyfish is displayed with a triangle for north. This is a real time representation of what the vehicle is doing. Figure 1.5 shows a comparison of the actual vehicle and the real-time 3D representation. This data can now be used in off-board software, but the heading, pitch, and roll information could be used by on-board processors in the future.

Figure 1.5: 3D representation of actual vehicle movements

1.2 Artificial inclinometer based upon jellyfish statocyst organ

The COTS tilt sensor approach provided useful results that contributed towards the learning of jellyfish vehicle stability and control mechanism. The COTS tilt sensor performance provided baseline performance against which the results from bio-inspired tilt sensor can be compared and analysed. The natural statocyst of the jellyfish works in an interesting way, and this platform is simple enough to implement using the current fabrication techniques available in design of electronic circuits. Extremely small surface mount resistors (.012" in width) were used to mimic the "setae" and a metal ball was used to mimic the "statolith". The statolith ball rolls around inside a circular cavity and contacts the "setae" to complete the circuit with the base plate. The setae are sensors and in this case are represented by small surface mount resistors. As the jellyfish tilts, the metal ball will roll and contact various resistors – the resistance of the sensor is then measured through the terminals as a voltage divider. The input signal is a small 5V potential. The output is then an analog signal between 0 and 5V which linearly increases with tilt angle.

Figure 1.6 shows SEM images of the natural jellyfish statolith taken from an *Aurelia aurita* sample. This shows the analogous nature to the spherical metal ball. In nature the statolith is formed from bismuth or calcium carbonate.

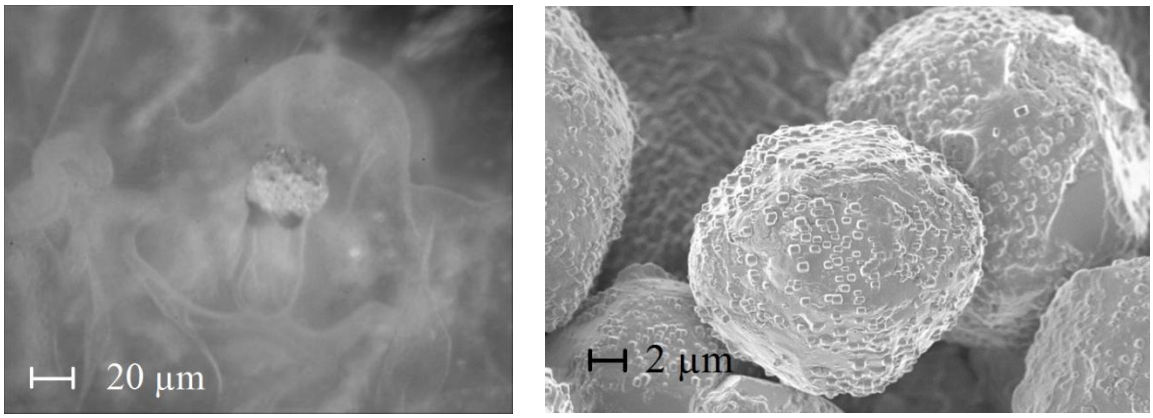

Figure 1.6: Microscopy of statocyst within rhopalia structure and up-close SEM of natural statolith ball

There was a steady progression from the natural jellyfish statolith seen in Figure 1.7 to all the way towards design of artificial statocyst. An electrical schematic is shown in Figure 1.8 that explains the artificial analog. Sixty 300 ohm surface mount resistors were connected in series. The initial prototype

can be seen at the far right of Figure 1.7. Figure 1.9 shows the slightly improved statocyst with gold plating to increase the conductivity. Initially some readings were not clear due to the thin layer of oxide on the conductive surfaces. Adding gold increases conductivity as well as insures a long lasting sensor due to its anti-corrosion properties.

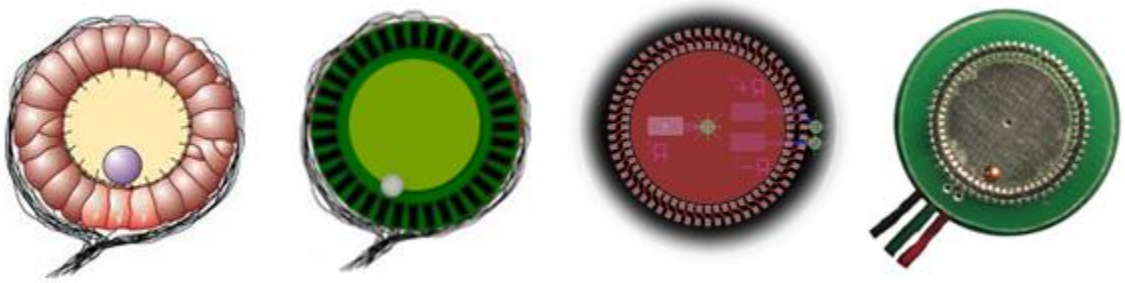

Figure 1.7: Progression of the macro-scale prototype from biology to final electronic prototype

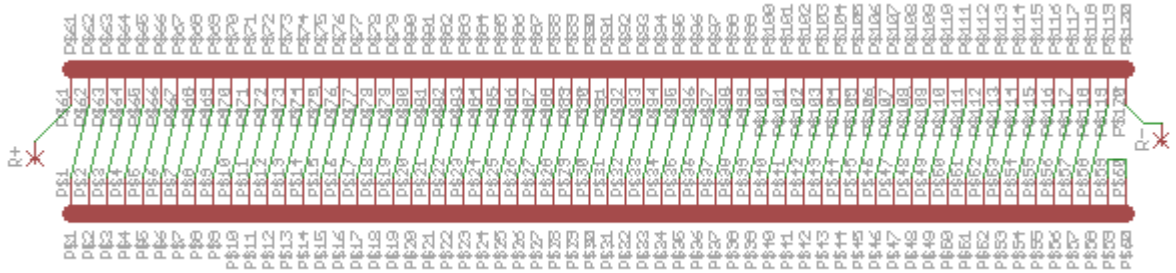

Figure 1.8: Circuit diagram of artificial jellyfish statocyst

The linearity of the sensor was investigated by checking each of the sixty connections individually with a multimeter. The analog voltage output was recorded and plotted against resistor number to visualize is the variation. This is a function of the changes in resistor value provided by the manufacture. It was found that the sensor was quite linear with a slope of 0.0831. If the sensor was perfectly linear the slope should be 0.0833 since we are chopping the 5V signal into 60 individual voltage dividers. Figure 1.10 shows the results of this test.

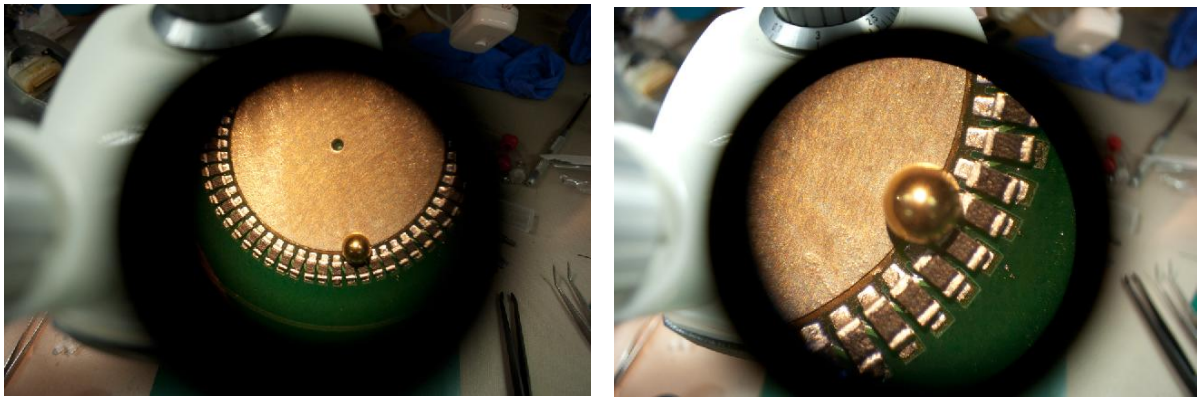

Figure 1.9: Microscope view of the improved artificial statocyst

Figures 1.11 and 1.12 represent the sensitivity and accuracy of the sensor, respectively. An automatically controlled tilt table was used to actuate the sensor. The angle at which the sensor initially responded was recorded as well as the final resting position of the artificial statolith. This test was run many times to ensure an even statistical distribution. The average angle needed for reading was found to be 4.21 degrees with a standard deviation of 1.77 degrees and the average deviation from the true reading was found to be approximately 4.85 degrees with a high standard deviation of 4.88 degrees. Since each resistor-sensor is equal to 6 degrees, this means that on average the sensor is accurate down to less than one fully resolved physical sensor position.

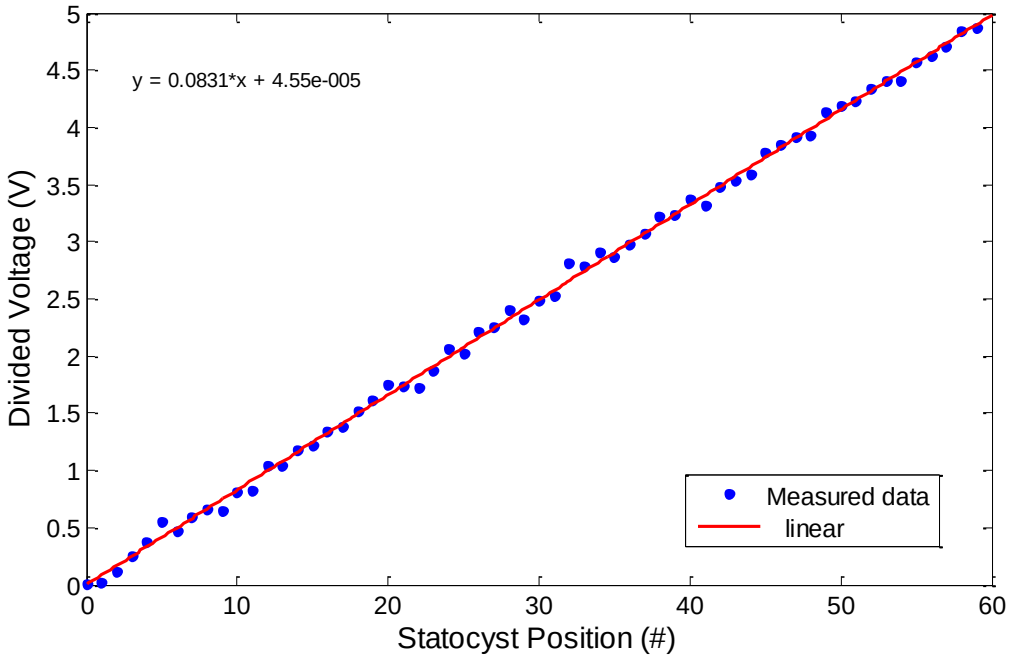

Figure 1.10: Statocyst position vs. voltage divider output

Figure 1.11: Describes the angle at which the sensor must tilt before a reading can be obtained

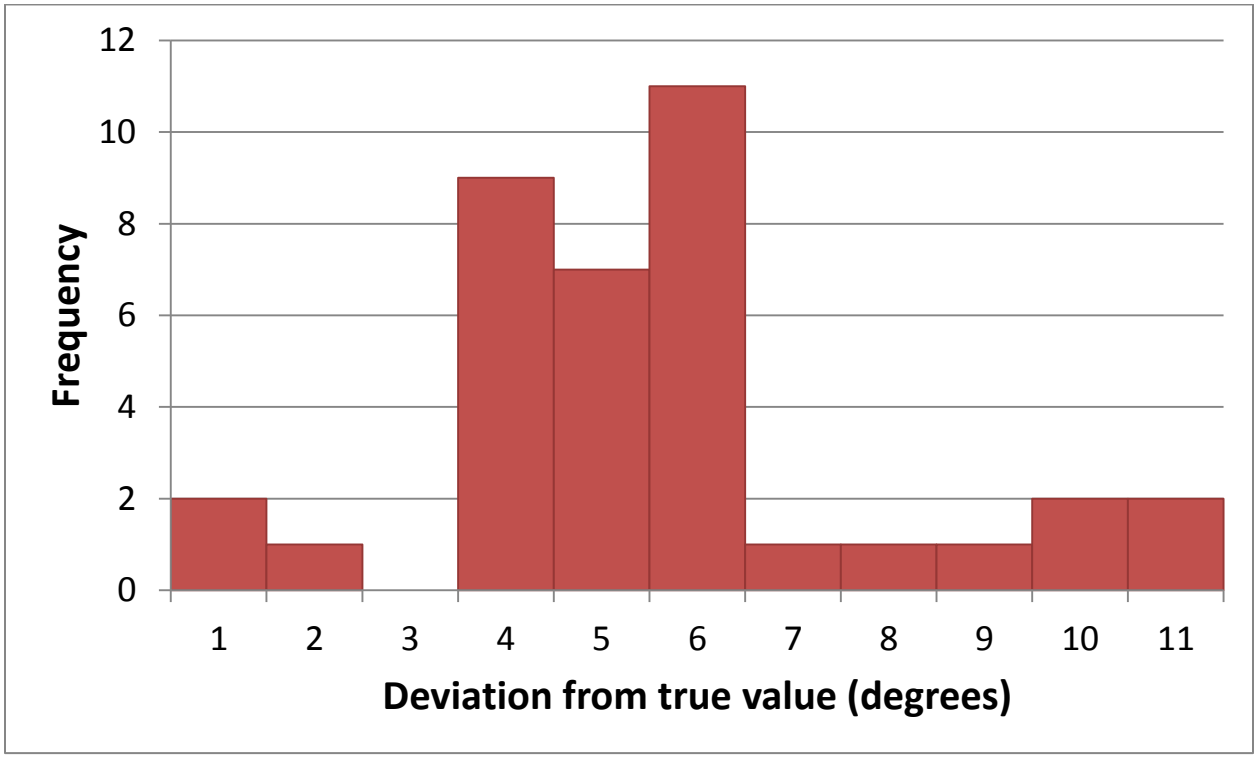

Figure 1.12: The accuracy of the sensor was measured over a variety of readings

We believe this is an excellent result given the simplicity in design of the sensor. By using better fabrication techniques one can incorporate highly dense packing of resistors and instead of using one metal ball one can use multiple of them. This will definitely lead to higher sensitivity. Artificial statocyst reduces the complexity involved in extracting the tilt angle as the voltage readings are directly obtained. However, a conventional off-the shelve sensor chip needs several intermediate steps before the final output can be obtained (such as Honeywell HMC634). In this case, first the tilt sensing occurs and data is stored momentarily on the chip. Then the data is transferred through an I2C bus to a converter that allows the computer to use USB protocol. This COM signal is then run into software such as LabView where the raw data is collected. A LabView VI then stores the data, which can be displayed on the screen in a variety of ways. In comparison, the data from artificial statocyst can be directly utilized in LabView.

1.3 Design and modeling of the Bio-inspired Multi-Axis MEMS Inclinometer

The objective in this section was to design the process for scaling the above mentioned macro-scale biomimetic tilt sensor by utilizing MEMS technology. Three significant improvements are expected by redesigning the sensor. First, the dimensions of sensor are greatly reduced. The current sensor is approximately 20 mm in diameter. With MEMS technology, it is expected that the final size would be less than 1 mm in diameter. This 99.75% reduction in surface area will allow the sensor to be used in smaller vehicles or robots where the current macro-scale prototype will not fit. Secondly, a capacitive sensing structure will be utilized to reduce the power consumption. Capacitive sensors use essentially zero power, as opposed to the current prototype which uses constant power at 5 V potential. This energy saving will allow the sensor even more applicability in small, untethered systems with limited power resources. Lastly, the current prototype only allows for direction of tilt to be measured. By using a cantilever structure with varying bending we can also measure some changes in degree of tilt. In fact, it has been calculated that we can obtain approximately a 3 degree resolution in this measurement. By increasing the number of radially arranged cantilevers, we can also greatly increase the heading angle sensitivity.

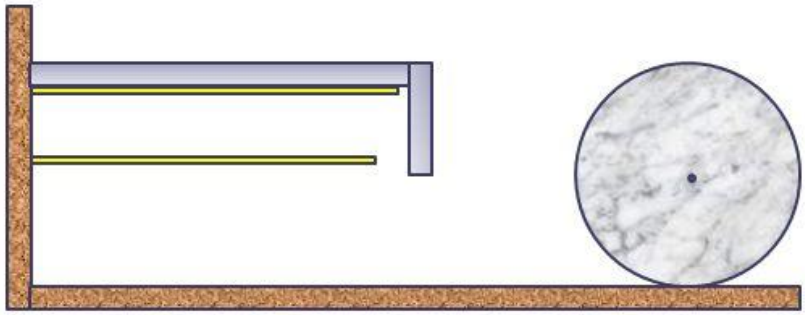

Figure 1.13: Basic concept of a mineralized ball pushing against a sensing hair (cantilever) with capacitive structures

Figure 1.13 shows a brief description of the cantilever structure. A horizontal beam is fixed on left side wall and a small vertical contacting surface is hung at the right end of horizontal beam. When the ball rolls down to the contacting surface and presses it, a clockwise moment presses the cantilever down and so the horizontal beam bends down. There are two conducting surfaces; one attached to right below the horizontal beam and another placed several microns down from the first conducting plate. When the entire structure is balanced evenly and the ball is not touching the contacting surface, the horizontal beam has no deflection and, therefore, the two conducting plates are parallel to each other. However, if the structure is tilted and the ball is pressing the contacting surface, the upper conducting plate bends down and the electrical conductance between the upper and bottom plates decreases. Because the amount of capacitance change is a function of structure's tilt angle, we can see how much the structure is tilted by measuring the electrical capacitance between the two conducting plates.

Using MEMS fabrication technology, the cantilever structure can be designed as small as several microns. However, dimension of the cantilever should be chosen carefully by taking into account magnitude of electric capacitance because the output electric capacitance output has to be measured by an external CDC (Capacitance to Digital Converter) chip and so its value should be in a detectable range of currently available IC-chip technology. In our simulation, we assumed that AD7147 CDC (Analog Devices, Inc.) will be used to measure the electric capacitance of the cantilever structure. This chip has input range of ∓ 8 pF and its resolution is 16 bits. In other words, the AD7147 CDC can measure small electric capacitance down to 0.244 fF which is quite high resolution and suitable for small capacitor structure.

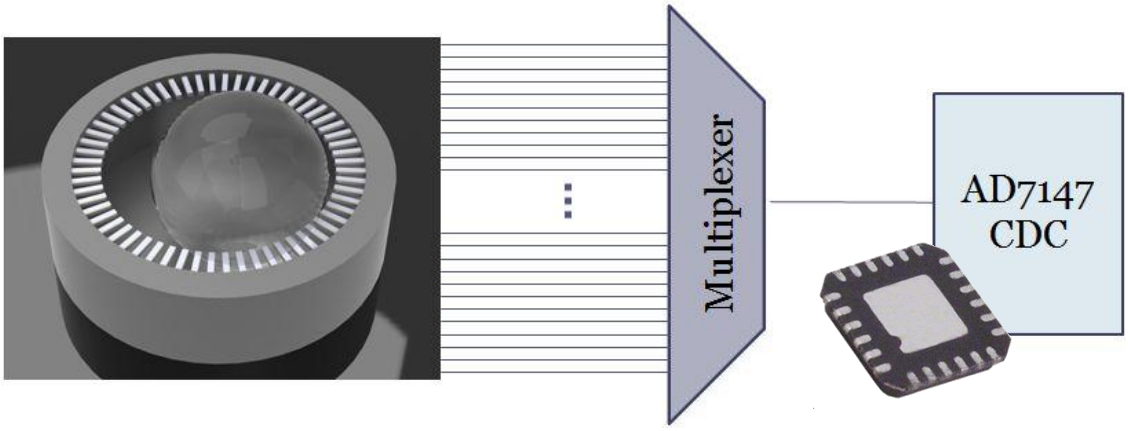

Figure 1.14: Electronics integration concept showing the 3D sensor, data moving through a multiplexer, and the capacitive sensing of the AD7147 chip

For better resolution of our proposed structure, there should be tens or hundreds of cantilevers placed around the circular cavity structure. Correspondingly, there are a number of electric capacitance signals coming out from the entire structure. Rather than connecting CDC chips to each different output channel of a cantilever, a multiplexer can be placed between the MEMS structure and CDC chip to process all cantilever signals with only one CDC chip. This can significantly decrease the size of the external signal processing structure.

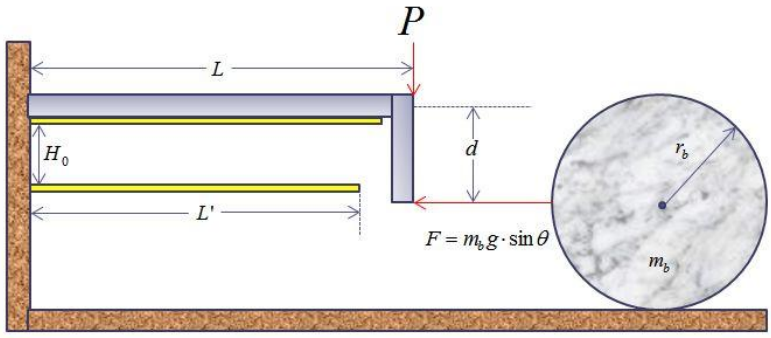

Figure 1.15: The true horizontal F-force had to be translated into a vertical P-force to use the simple form of the Euler-Bernoulli equation

The electric capacitance changes depend on the cantilever deflection, so the Euler-Bernoulli method can be introduced to describe how the horizontal beam bends. First, the force F pressing the contacting surface can be converted to a force P which presses downward on the horizontal beam by calculating equivalent moment.

$$P \cdot L = F \cdot d \tag{1}$$

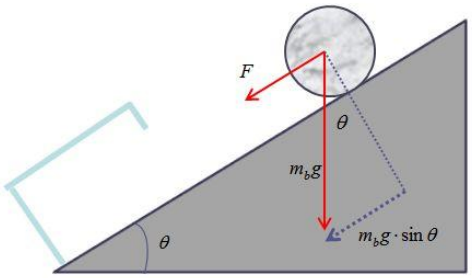

m_b : mass of ball

g : gravitational acceleration

θ : tilt angle

Figure 1.16: Tilt response of the cantilever

Here, force F is a function of tilt angle θ, so force P can also be written in terms of θ.

$$P = \frac{F \cdot d}{L} = \frac{(m_b g \cos\theta) \cdot d}{L} \tag{2}$$

By the Euler-Bernoulli equation,

$$\frac{d^2 w}{dx^2} = \frac{P(L-x)}{EI}, \text{ Boundary conditions: } w(0) = 0, \ \frac{dw}{dx}\Big|_{x=0} = 0 \tag{3}$$

where w is beam displacement at each position, E is Young's Modulus, and I is mass-moment of inertia of the cantilever. With the cantilever inertia as $I = \frac{bh^3}{12}$, the beam deflection can be shown in a final form as a function of distance along the beam and tilt angle of the sensor, as well as chosen dimensions and constants.

$$w(x,\theta) = \frac{PL}{2EI} x^2 \left(1 - \frac{x}{3L}\right) = \frac{2m_b g \cdot d}{Ebh^3 L} (3x^2 L - x^3) \cdot \sin\theta \tag{4}$$

This form is an ideal case which is based on several assumptions. First, the vertical contacting surface remains vertical and does not give considerable effect on beam's deflection because it has quite small

dimensions compared to the horizontal cantilever beam. Second, the conductor plate attached right below the cantilever beam has negligible thickness and so it gives almost no effect to beam's deflection.

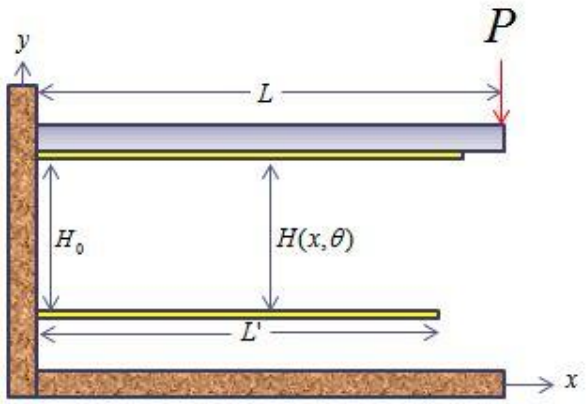

$$H(x,\theta) = H_0 - W(x,\theta)$$
$$A(x) = b \cdot x$$

$$H'(x,\theta) = -W'(x,\theta)$$
$$A'(x) = b$$

Figure 1.17: Final model with dimensions used to calculate deflection and capacitance

Now we have distances between the two conducting plates at each position along the x-axis and we can use this in the calculation of electric capacitance.

$$C = \varepsilon_0 \frac{A(x)}{H(x,\theta)} \tag{5}$$

The equation for electric capacitance is electric permittivity multiplied by surface area of conducting plate divided by the distance between two surfaces. But in our case, the distance between two plates is a function of x, so the total capacitance is the integration of infinitesimal capacitance component at each point along the x-axis from 0 to L'.

$$\frac{dC}{dx} = \varepsilon_0 \frac{b(H_0 - W) - bx(-W')}{(H_0 - W)^2} \tag{6}$$

$$C_{tot}(\theta) = \int_{x=0}^{L'} dC = \int \varepsilon_0 \frac{b(H_0 - W) + bxW'}{(H_0 - W)^2} dx \tag{7}$$

Finally, capacitance is shown as a function of tilt angle of the sensor along with the previously derived equation for the deflection of the cantilever beam. This equation cannot be solved directly, as

was instead numerically solved with computer code. With given equations, the parameters of entire system are chosen to be simulated. Table 1.1 shows each parameter value.

Table 1.1: Final parameters used for the mathematical simulations

Parameter	value	Parameter	Value
L	100um	E	160GPa
b	20um	H_o	3um
H	1um	R_b	300um
L'	95um	m_b	0.9ukg
d	15um	G	9.81kg/m^2

MATLAB simulation was used to estimate the beam deflection and total capacitance changes as a function of the variation of tilt angle from 0 to 90 degree.

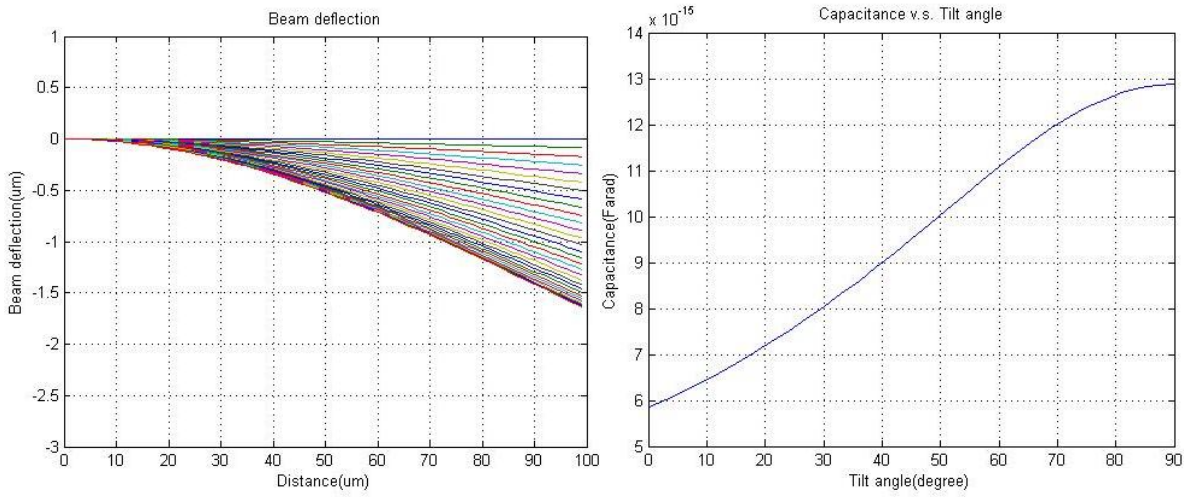

Figure 1.18: Output from MATLAB with information on the deflection of the beam across its entire length as well as capacitance versus tilt angle of the sensor

With given dimensions, the total capacitance varies from 5.841 fF to 12.88 fF. If the output is measured by AD7147 CDC chip which has resolution of 0.244 fF, the cantilever structure will have resolution of 3.717 degree.

$$\frac{90^{\circ}}{(\Delta C / 0.244\, fF)} = 3.717\,\text{deg}$$

In an effort to improve the initial electromechanical model, ANSYS Finite Element Analysis (FEA) was utilized to simulate and predict beam deflection caused by the force transferred from the ball. Figure 1.19 compares the simulated deflection as predicted by ANSYS and Euler-Bernoulli beam theory. The two predictions are similar towards the clamped end of the beam but differ by 25% (from 1.6 micron to 2 micron) at the free end. This difference can be explained through one of the assumptions that was made in order to apply the Euler-Bernoulli equations to the system. The force from the ball is applied to the lip of the beam in actuality, but the Euler-Bernoulli theory required a force applied at the tip. An equivalent force was estimated by calculating the moment at the clamped end as explained earlier. In making this assumption, moments caused by infinitesimal shear forces within the beam towards the free end are ignored, but accounted for in the ANSYS simulations where the force translation is not required. The deflection profile predicted through ANSYS replaced the predictions through Euler-Bernoulli theory in the electromechanical model improving the accuracy of the model.

The beams were designed to deflect with minimal forces therefore the beam is very thin and potentially prone to mechanical failure. In order to ensure that beam can deflect to the maximum deflection point without mechanical failure stress analysis was performed. The failure criteria chosen for the beam was ultimate tensile strength due to the beam material made of silicon nitride which is a brittle material. Figure 1.20 shows the stress profile in the beam along the lengthwise direction of the beam. The maximum stress occurs near the clamped end which is expected due to the clamped boundary condition at this end. Also near the tip of the beam there is a stress concentration caused by the interaction between the end of the beam and the lip. The maximum stress in the beam is 32 MPa and the ultimate strength is 120 MPa, a factor of safety of 3.75. It should be noted that the applied force in the simulation was static and that dynamic forces were neglected. It was assumed that the velocity and distance traveled by the ball is negligible within the sensor, therefore static simulations were determined to be sufficient. For extreme applications where rate of tilt direction is aggressive dynamic simulations will be performed to ensure failure does not occur.

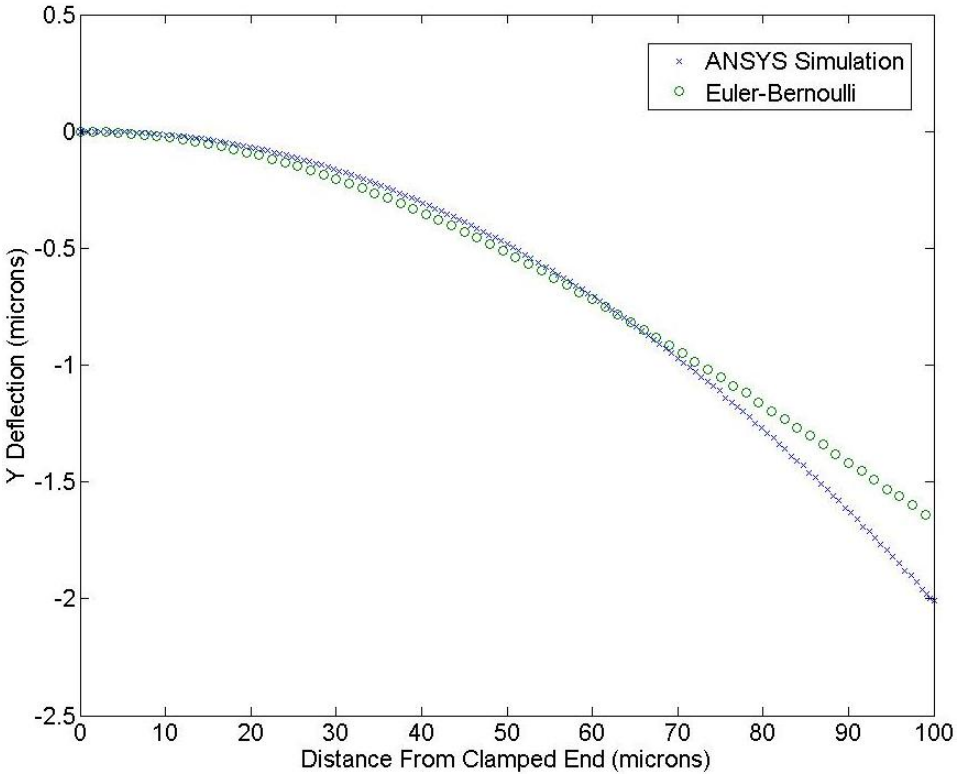

Figure 1.19: Profile deflection from the MATLAB simulations were compared to ANSYS results

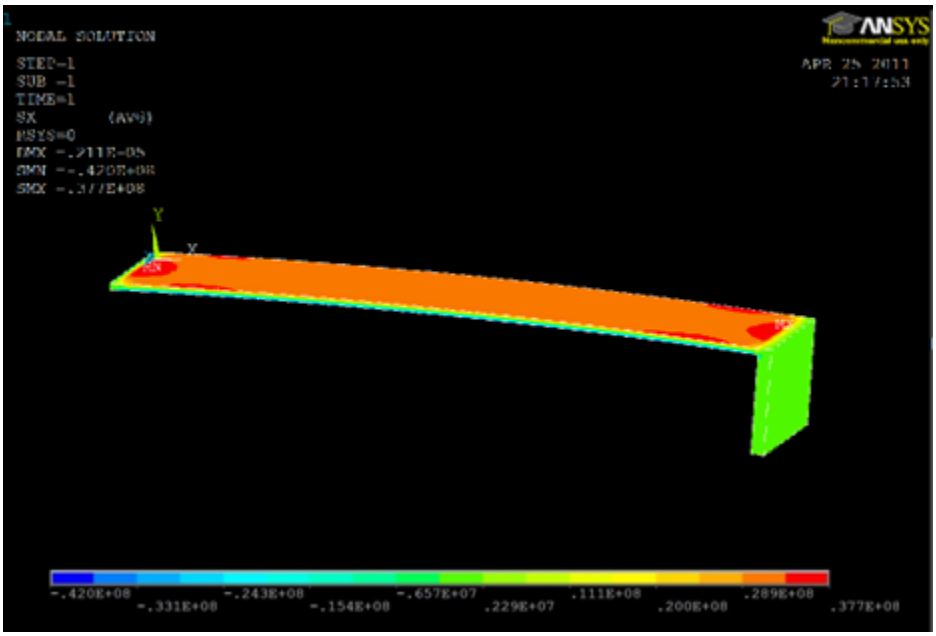

Figure 1.20: ANSYS showed stress across a 3D cantilever with noted stress concentrations at the clamped end as well as between the free end and the contact tab

1.3.1 Process Flow

A process flow was developed in order to fabricate the sensor. The fabrication process is outlined in Figure 1.21 below. The process is a combination of surface and bulk micro machining techniques. Steps 2-5 create the bottom static cantilever/capacitive surface. PECVD oxide is used as a sacrificial layer to separate the bottom cantilever from the top cantilever. After the top cantilever is fabricated in steps 7-10 the back side of the wafer is etched by using DRIE and anodically bonded to a Pyrex wafer in order to create the recessed surface for the ball to sit on. The last step etches the sacrificial oxide layer releasing the cantilever beams. The release is completed under supercritical CO_2 drying in order to prevent stiction. Any internal stress in the silicon nitride and Cr/Au layers can cause unwanted deflection after the release. To prevent any unwanted deflection from occurring PECVD was chosen as the deposition method of silicon nitride and sputtering was chosen as the deposition method of Cr/Au. The deposition settings of PECVD and sputtering can be altered in order to control the levels of stress within the films to find the optimum balance so that no unwanted deflection occurs.

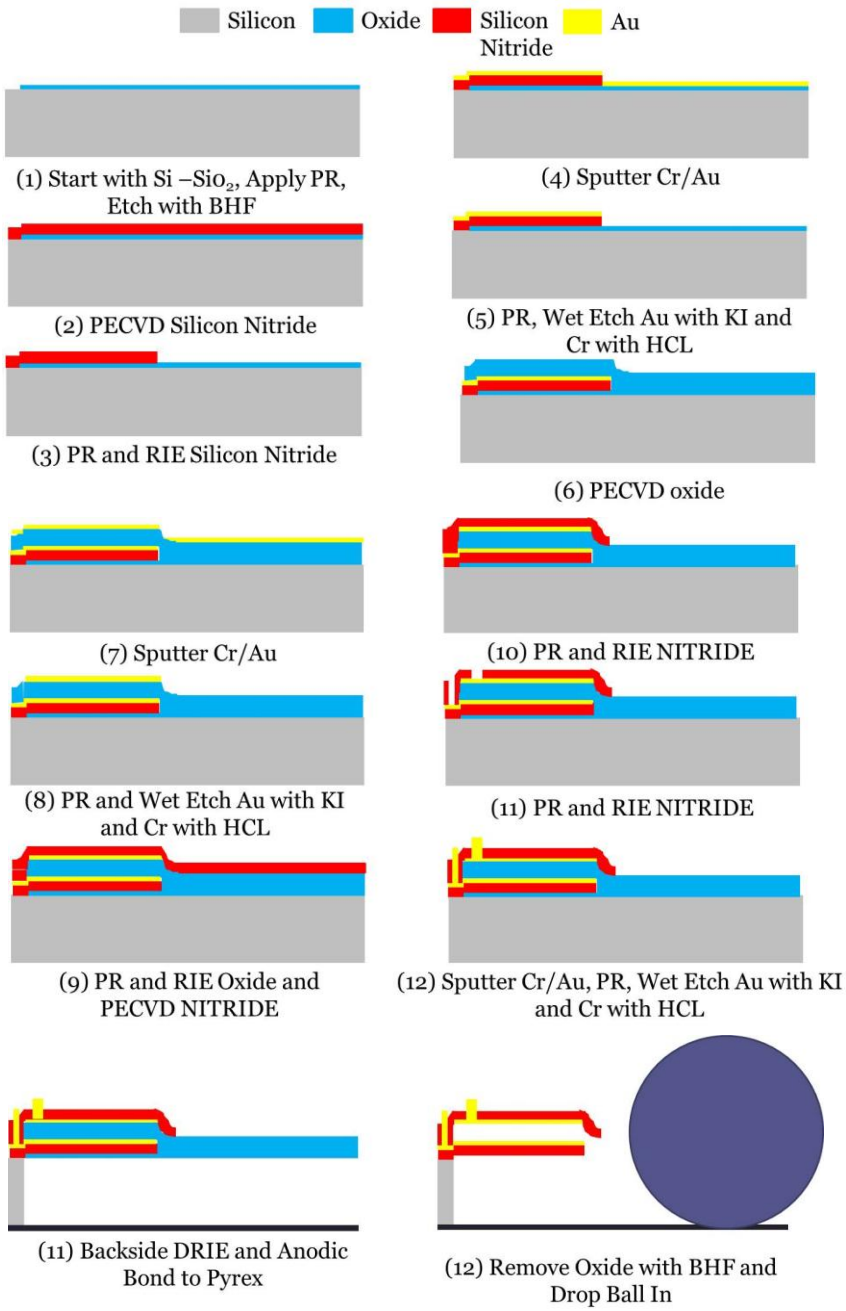

Figure 1.21: Detailed process flow of the MEMS statocyst

Chapter 2:

Multilayered conducting polymer

Biomimetic applications are increasingly in need of actuators that can accurately mimic natural muscle. Actuators of the past were comprised mostly of electromechanical motors such as steppers or servos. These actuation techniques are not life-like and consume large amounts of power, while taking up a large amount of space due to their bulkiness. Biological creatures do not have "motors" but instead rely on internal muscles that both create stress and deform as their structure. Several advances, realities and challenges have been discussed in the area of artificial muscles that mimic natural muscle (Wallace et al 2007, Bar-Cohen 2004, Mirfakhrai et al 2007); some notable technologies are air powered and pneumatic muscles (Ching-Ping and Hannaford 1996), shape memory alloy (Seelecke and Müller 2004) and polymer actuator technologies (Mirfakhrai et al 2007). Composite actuator technologies such as bio-inspired shape memory alloys composites, BISMACs (Villanueva et al 2010), are employed to achieve desired performance for biomimetic applications. Conductive polymer actuators are useful for biomimetic applications because they are lightweight and use little power. In electric motors rotational motion can only be produced at the output shaft; whereas in conducting polymer, the entire polymer actuator is involved in the motion, reducing the space requirements. Conducting polymer actuators (PPy actuator) like other smart materials directly incur bending or contraction within themselves, where electromechanical actuators need additional mechanisms to convert force into bending or contraction that occur external to the confines of the actuator.

Recently, jellyfish have become a notable biological candidate for the use of new actuators that mimic natural muscle (Villanueva et al 2009). Jellyfish are invertebrates, essentially unchanged from their ancient roots. They have a relatively simple muscle structure with radial or circumferential muscles that can easily be copied with artificial actuators. Even in their simplicity, the motion of jellyfish is considered extremely efficient. Jellyfish are being looked at for a variety of real-world applications such as military surveillance. There are roughly 1500 species that span every ocean in the world, as well as some lakes. They exist in a multitude of morphologies and colors. With this breadth in appearance and spread of the organism, artificial jellies can easily blend in to their surroundings and do not raise suspicion. In order to develop artificial jellyfish, conductive polymer actuators must be matured to the point where the force and deflection produced can match that of the natural jellyfish muscle. There are

several advantages of using conductive polymer technology in an underwater platform; for instance, the conductive polymer composites can be actuated in electrolyte, such as seawater. Previously, polypyrrole-metal composite actuators have been developed in strip and helical types (Tadesse et al 2008, Tadesse et al 2009). The goal now is to increase their performance with a variety of techniques, and measure the resulting response.

2.1 Synthesis of axial type PPy–metal composite actuator in aqueous solution

The strip geometry actuator was synthesized following the description given in (Tadesse et al 2008). A gold coated PVDF membrane obtained from KTech Corporation was cut to rectangular dimensions. Polymerization was conducted in an aqueous solution containing 0.05 M Pyrrole, 0.02 M TBAP and 0.1 M KCl in electrochemical cell with platinum plate counter electrode, Ag/AgCl reference electrode and the Au coated PVDF as a working electrode. For the axial type, helically interconnected PPy actuators were synthesized using electrochemical deposition on a gold coated polylactide core substrate with a thin Pt-wire winding as a substrate material. Figure 2.1 schematically represents the fabrication steps and structure of synthesized actuator. First Polymerization was conducted using the synthesis process reported in the earlier study (Tadesse et al 2008, Tadesse et al 2009) where the synthesis solution was composed of 0.05 M pyrrole, 0.1 M KCl and 0.02 M tetrabutylammonium perchlorate with multiple layer of platinum winding applied on the subsequent coating of polypyrrole. The current study is focused on increased amount of monomer concentration which would improve the thickness of polymer on one layer of platinum and hence affect the geometry of synthesized actuator. The monomer concentration was increased five times higher than previously used (i.e 0.25 M pyrrole, 0.5 M KCl and 0.1 M tetrabutylammonium perchlorate).

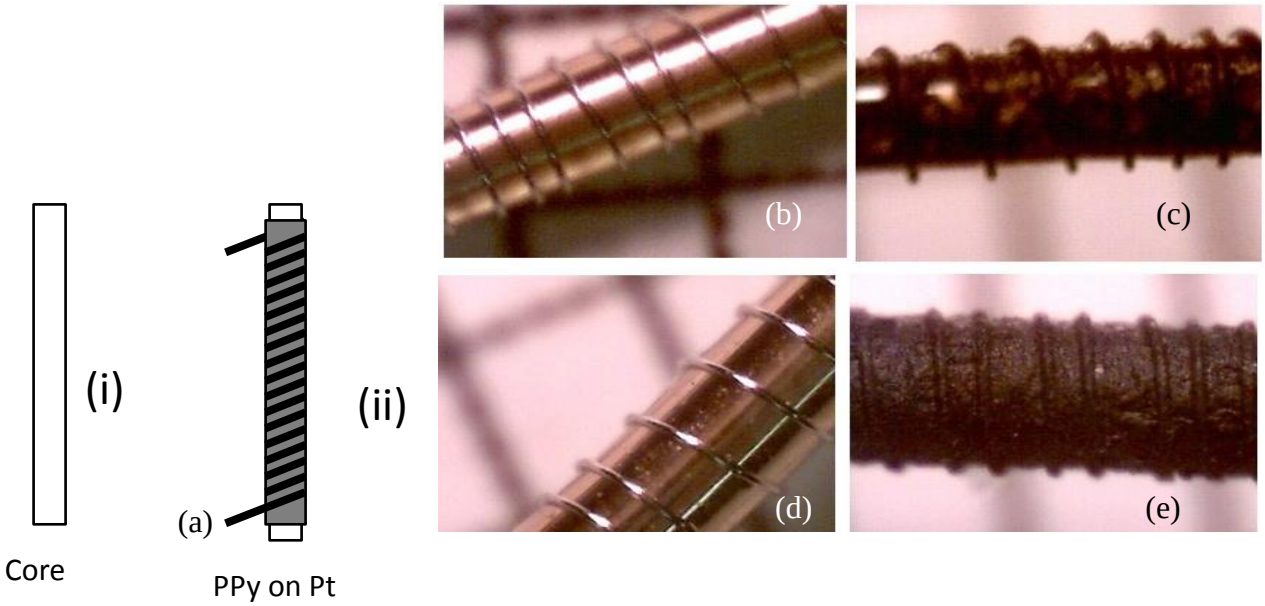

Figure 2.1: (a) Schematic diagram of fabrication process: (i) gold coated PLA rod, (ii) platinum winding on the rod and polymerization, (iii) dissolving the PLA core; PPy composite actuator: (b) sample 1 before and (c) sample 1 after polymerization (d) sample 2 before and (e) sample 2 after polymerization.

Two samples were synthesized using the dissolvable PLA core substrate as shown in Figure 2.1 (b)-(e). To attain a rigid PLA core substrate, PLA fibers were melted and extruded to a desired diameter. Next, the PLA rods were coated with gold by sputtering and platinum wires were wound around the gold coated rod. The polymerization of pyrrole in the presence of doping ions TBAP and KCl was performed with higher concentration of monomer than previous studies. Sample 1 was synthesized in aqueous solution containing 0.05 M pyrrole, 0.02 M TBAP and 0.1 M KCl to obtain a control and sample 2 was synthesized in five time higher concentration than sample 1 (0.25 M pyrrole, 0.10 M TBAP and 0.5 M KCl). One layer of 76µm diameter platinum winding was applied on a gold coated polylactide rod and polymerization was performed in a three electrode electrochemical cell for 12 hrs using cyclic voltammetry. The electrodes in the cell consisted of a platinum counter electrode (52 mm length, 5.5 mm width and 0.07 mm thickness), a standard Ag/AgCl reference electrode and the working electrode (actuator) with platinum winding on PLA rod (1 mm diameter and 55 mm length). Figure 2.1 (b) and (c) shows the images of sample 1 with the platinum winding before and after the polymerization. Figure 2.1(d) and (e) shows the images of sample 2. It can be seen that for higher monomer concentration the coating was uniform and thicker. Typical cyclic voltammograms for the synthesis conditions are shown in Figure 2.2 (a) and (b). Sample 1 had the peak anodic current of 0.6 mA whereas sample 2 had the peak anodic current of 3 mA. The lowest current for sample 1 was -1.6 mA while that for sample 2 it was -10 mA. The synthesized long actuators are shown in Figure 2.2(c) and (d) before and after the core PLA is

dissolved and after. A 76 µm platinum wire was used to wrap around the PLA rods by using a custom-built helical winder machine. The spacing (pith) between the winding was 3-4 turns per millimeter. Once the substrate was coated with polypyrrole, the core polylactide rod was dissolved in a solution containing a mixture of dichloromethane and 0.05 M HCl in a 4:1 ratio by volume. Successful fabrication of an actuator with length greater than 50 mm was achieved. As can be seen in Figure 2.2 (d), Sample 1 was coated with less amount of polypyrrole around the Pt winding, effectively reducing the interconnectivity.

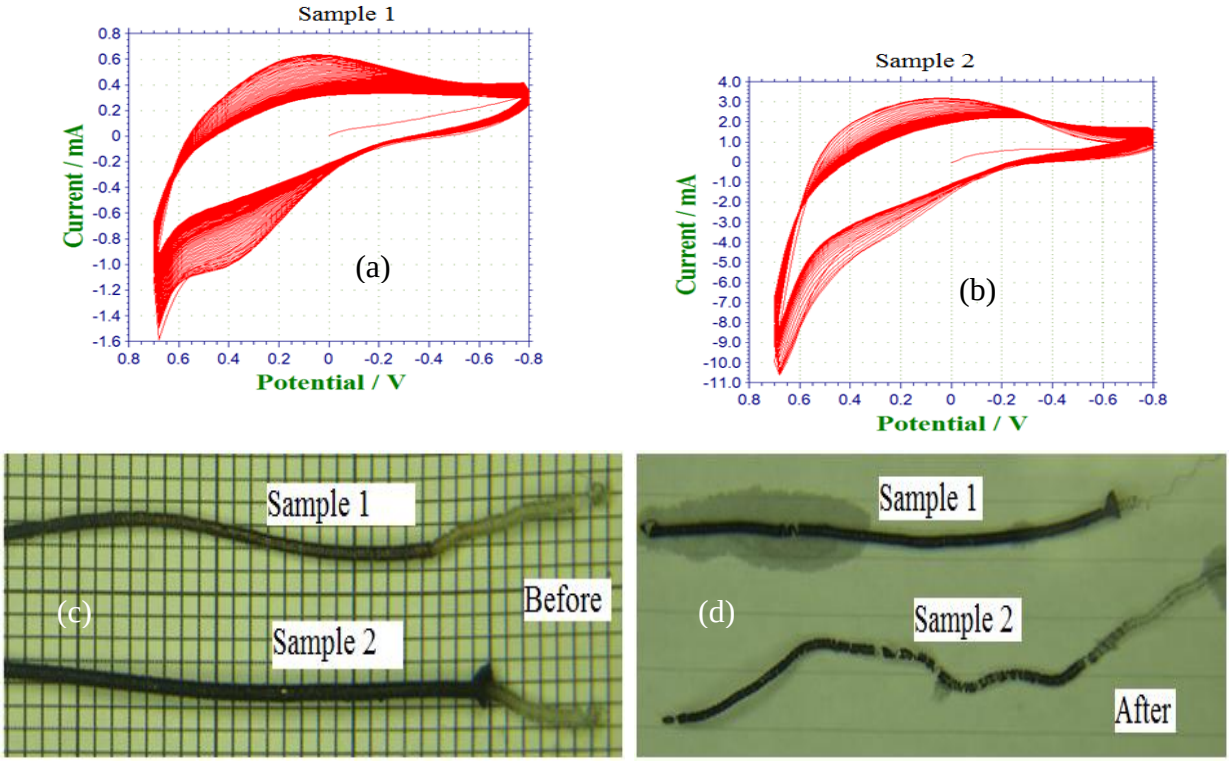

Figure 2.2: (a) Typical voltammogram for sample 1 and (b) voltammogram for sample 2 with a scan rate 0.1V/sec. (c) Pictures of sample 1 and 2, before the core PLA is dissolved, (d) after the core is dissolved.

2.1.1 Microscopy

The structure of the tubular PPy-metal composite actuator was observed with a scanning electron microscope (SEM) before and after the core PLA was dissolved. The SEM micrographs are shown in Figure 2.3 (a) and (b). It can be inferred from the SEM micrograph that the core PLA rod appears as a whitish circular island before it is dissolved (Fig 2.3 (a)). The interface between PLA rod and the PPy surface is indicated in the inset and the magnified view is shown in Figure 2.3(c). The magnified view reveals that there is a clear boundary between the two interfaces. After the core PLA is dissolved a hollow

tube structure is obtained and illustrated in Figure 2.3 (b). The internal wall surface of the tube appears distinct from the PPy outside layer which indicates that the original gold layer is not altered. An inset of the wall of the actuator is depicted in Figure 2.3 (d) and it can be easily seen that the 76 µm Pt winding wire is covered by the PPy from both the inside and outside.

The average outside and inside PPy layer thickness covering the platinum coil was 92 and 81 µm respectively. It was also observed that remnant PLA films cover some portion of the actuator. Physically such films are observed during dissolution with dichloromethane and dilute HCl. To avoid such films covering the actuator surface, changing the dissolving solution three or four times is required during fabrication. The existence of remnant film can be easily checked by taking the actuator and dipping it into a water bath. If there is a remnant film, it will create a slight isolated layer that is visible on the water surface. In such cases, dissolving in another dichloromethane solvent removes it completely. The SEM images confirm that a tubular PPy- composite actuator can be fabricated using the dispensable polylactide substrate as a core and the surface morphology was not affected by the solvent utilized during the synthesis. One of the reasons to use polylactide core substrate as a dispensable material was its dissolution with organic solvent such as dichloromethane without affecting the polypyrrole. The other reason for using polylactide is hydrolysis with acid and water.

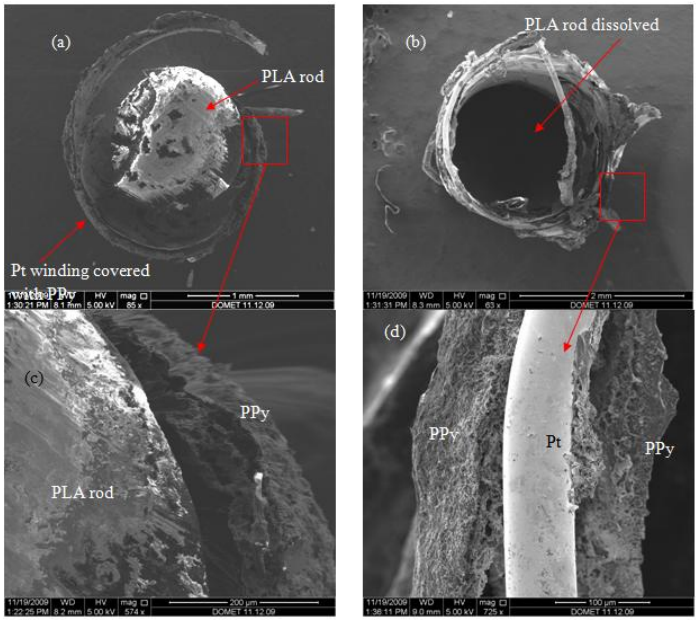

Figure 2.3: Scanning electron micrograph (SEM) of synthesize actuator with 0 .25 M Pyrrole, 0.10 M TBAP and 0.5 M KCl (a) Top view of the Au coated PLA rod before dissolution. (b) after dissolution (c) magnified view of PLA rod and PPy covered (d) magnified view of the wall of the actuator after dissolution.

2.1.2 Application for biomimetic jellyfish

The strip actuator was used to construct the biomimetic jellyfish taking advantage of its low-frequency response. Normally, a conducting polymer actuator requires electrolytic media for its operation. But as shown earlier (Tadesse et al 2008, Alici et al 2006) a PPy/PVDF/PPy trilayer actuator can operate in air. The actual total layer is five layers if the gold layer is accounted for. However, the thickness of the gold layer is in the range of angstrom and it can be ignored. Initially, experiments were conducted to characterize the flapping characteristics of PPy/PVDF/PPy composite trilayer actuator in 0.1 M KCl solution. The actuator was found to exhibit the sinusoidal response under small electrical field drives. A gold coated PVDF membrane obtained from KTech Corporation was cut to rectangular dimensions of 30 mm length x 5 mm width x 0.025 mm thickness. Synthesis of the actuator was conducted in an aqueous solution containing 0.05 M Pyrrole, 0.02 M TBAP and 0.1 M KCl. The strip actuators were immersed up to 20 mm within the solution and polymerization was carried out at a 50 mV/sec scan rate. Once the required number of actuators was fabricated, they were mounted on aluminum plates which were connected to a Styrofoam ball and bonded with glue. The plates served as an electrical connection as well as support for the actuators. All of the plates were interconnected with silver tape. The eight actuators were attached to the aluminum plates around the periphery of ball with conductive epoxy. Once the epoxy was cured, the top layer of the actuators was connected with silver strips. Figure 2.4 shows the prototype used for characterization of the eight actuators.

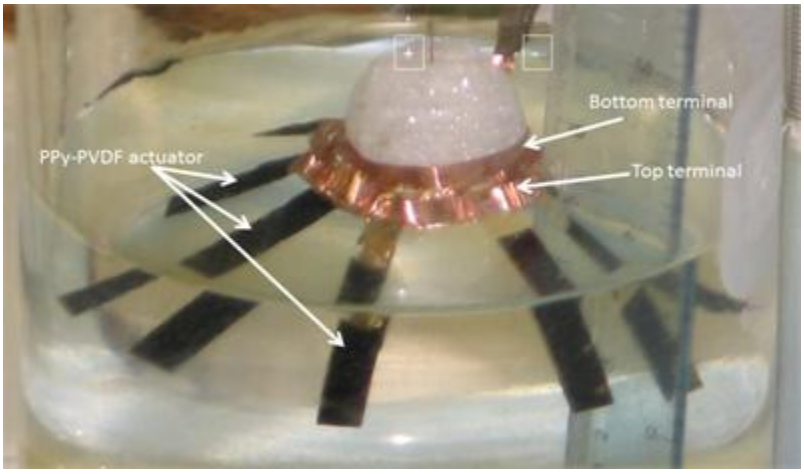

Figure 2.4: PPy-PVDF jellyfish prototype

Extensive characterization of the jellyfish was performed using a function generator (HEWLETT PACKARD 3314A) which applied cyclic potential on the actuators at varying frequencies and amplitudes. All actuators exhibited bending deformation and the tip movement of the free end was recorded by using a high magnification video camera. The displacement of the tip of the jellyfish tentacles was extracted with image processing MATLAB program. Figure 2.5 illustrates the amplitude of oscillation of the tentacles. It can be seen from this figure that for an applied potential of 7 V with 1 Hz frequency, the tentacle displacement consistently reaches 0.5 mm.

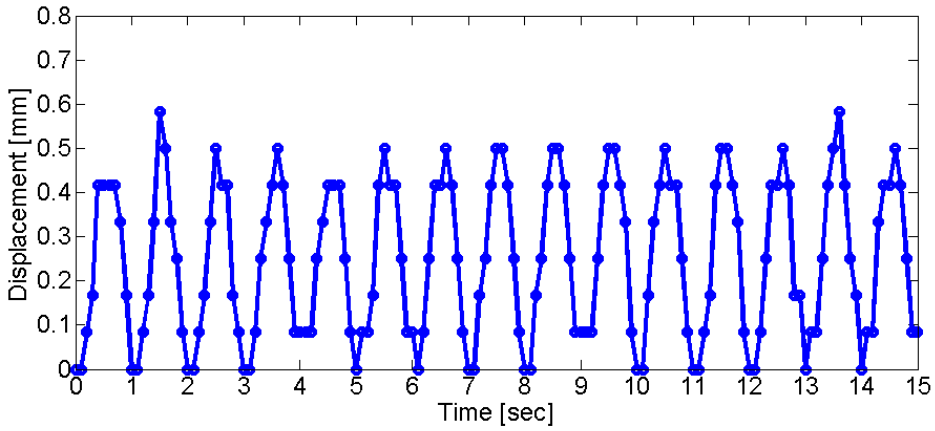

Figure 2.5: Amplitude of PPy-PVDF jellyfish wing at 7V at 1 Hz in 0.1M KCl solution

At low frequency of 0.2 Hz, the tentacle displacement was found to reach up to 2.8 mm and it was found that the forward and the backward movement were not of equal amplitude. Figure 2.6 shows the resultant displacement of the jellyfish umbrella (one strip actuator).The amplitude of displacement was less than that observed in air which is expected as the actuator was subjected to a uniform drag in the aqueous solution. The result of Figure 2.5 is encouraging as the overall thickness of actuator is merely 63 μm and yet it shows the ability to push the water and create a wake. It is also the first time conducting polymer composite actuator utilized for biomimetic jellyfish.

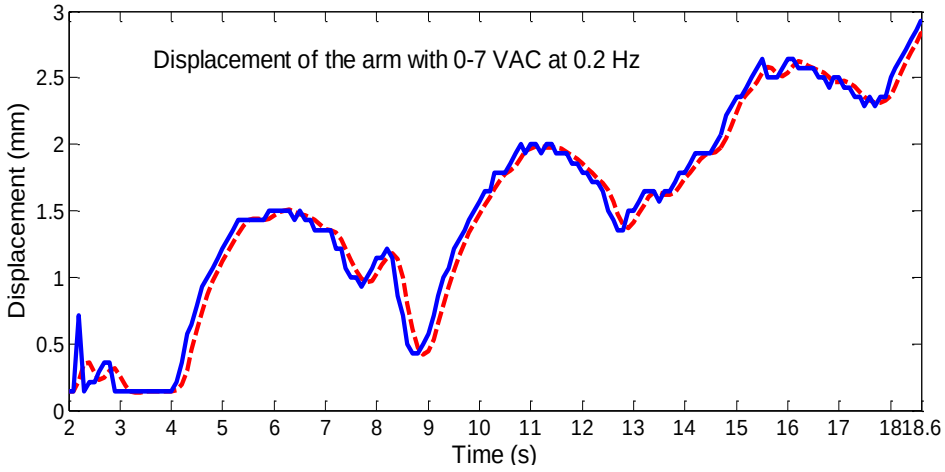

Figure 2.6: Displacement of PPy- PVDF jellyfish umbrella (one actuator) at 0.2 Hz and 7 V in 0.1 M KCl solution. The red line indicates data with noise removed due to filtering.

2.1.3 Summary and conclusion

The performance PPy composite actuator is mainly influenced by the geometry of the actuator and the chemical composition of the actuator. The geometry includes the dimension of the active layer (length, width and thickness) of the doped polymer and the support structure which is useful for the functional operation of the actuator. Strip geometry which utilizes a PVDF membrane demonstrates a bending movement due to the redox reaction on the top and bottom surface of the film. Axial type of PPy composite actuator also requires a passive substrate layer which supports the active doped PPy film. Usually a gold, platinum or tungsten wires are wound around a core substrate and PPy film deposition takes place on the surface. The cylindrical geometry will produce contraction and relaxation along the axis of the cylinder; however a slight difference in thickness of deposited PPy film will lead to a bending type motion. Several free characterization axial type of PPy-composite actuator exhibits a rotational motion in addition to translation. The experimental study in this paper indicate that axial type of actuator exhibit a combination of motion if the actuator is free in one end within the electrolytic media. The rotation could be utilized for various micro systems application. Two type of geometry of PPy composite actuators, strip and axial, were electrochemically synthesized using potentiodynamic film growth in an aqueous media and experimentally characterized in this study. The axial actuator consisted of a single layer of platinum winding on gold-coated core substrate with a high concentration of monomer (0.25 M Pyrrole, 0.10 M TBAP and 0.5 M KCl) yielded a uniform film of PPy than the less monomer composition (0.05 M Pyrrole, 0.02 M TBAP and 0.1 M KCl). Electrochemical characterization for force and displacement properties was conducted. A higher monomer sample tested in 0.1 M TBAP solution,

exhibit tip displacement of 6% of initial actuator length at an applied potential of 6V DC after 80 sec stimulation time. The blocking stress of 18 kPa was estimated by extrapolating the deflection magnitude on stress-strain diagram. The axial type geometry has a potential application to develop artificial facial muscle and other biomimetic application. The strip geometry with dimension of 20mm long, 5mm wide and 63μm thickness exhibit a 2.8 mm transversal deflection at 7V and 0.2 Hz. Application of strip geometry for biomimetic jellyfish application has been demonstrated by testing the actuator arrays within a 0.1 M KCl salt solution. Though, the thickness of the jellyfish umbrella is around micrometers, it was able to create a wake within the salt solution. Further study on the geometry structure such as multilayer technique is required to improve the performance.

2.2 Synthesizing PVDF membrane for multilayered actuators

Much attention has been given to ionic electroactive devices constructed with conducting polymers due to their low voltage requirements, high deflection, and similarities to natural muscle. Unfortunately, conducting polymer actuators have challenges related to repeatability and robustness. In addition, the two most important aspects of conducting polymer actuators that have not been addressed fully are their slow time response and low output force. In applications such as humanoid and biomimetic undersea vehicles the key requirements are total magnitude of force and displacement with fast time response (~1 Hz). Thus, even though conducting polymer actuators are projected to be promising candidate in these two applications their implementation has been limited.

Previously, displacement has been correlated to surface area of conducting polymer (Tadesse et al 2008), while the rate of change has been correlated to PPy thickness (Madden et al 2004). Deflections of 40% and rates of 13% per second have been demonstrated (Hara et al 2005, Zama et al 2005). An analytical bending model has been developed for single iteration actuators that showed the deflection is highly dependent on the modulus of the polymer substrate (Du et al 2010). Models of the force output of polymer actuators have also been created showing mathematically and experimentally that polymer actuators can be used for small robotic grippers (Alicia and Huynh 2006). Some work has also been done on feedback control of this actuator technology to reduce forward relaxation/creep or drift (Yao et al 2008).

Actuators with a higher force output are desired to be used in a variety of applications. Such application can take the form of a biomimetic robotic jellyfish (Tadesse et al 2010), expressive robotic

face (Tadesse et al 2008), or braille displays for the visually impaired (Ding et al 2003). All of these applications are limited by the small force output of conducting polymer actuators, while at the same time benefiting from the current magnitude of displacement and the time constants that have already been achieved.

In addition to the coil type conducting polymer actuator, we can produce flat, strip type actuators. Force output can be increased by increasing PPy layer thickness, however the time constant of actuation can be maintained by building a multilayer structure with multiple PPy iterations. This allows us to maintain each layer thickness optimum for actuation but still achieve overall thickness as desired for higher force.

In order to manufacture multilayered actuators, PVDF must be synthesized in membrane form on top of previously created layers. Applying previously manufactured PVDF membrane to a multilayered structure is difficult due to the need for an adhesive to connect the layers. Since the entire structure is only tens of microns in thickness, the addition of a adhesive even microns thick would upset the system. Also there must be good contact between the layers to promote ion transfer in the layers which is the direct mechanism responsible for actuation.

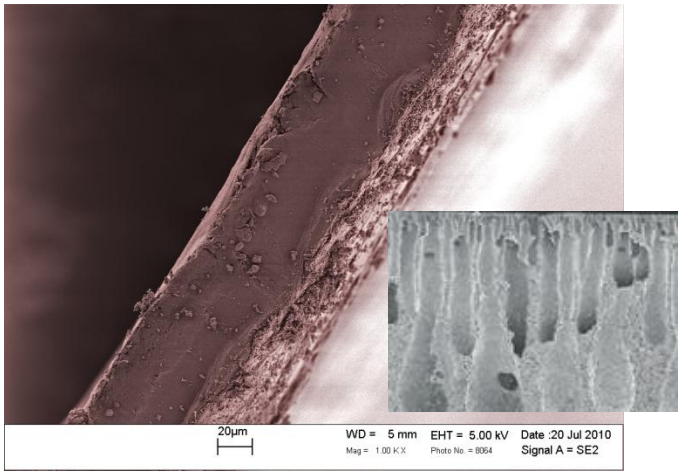

Figure 2.7: Membrane produced with hot press method, target pore structure (inset)

Multiple methods for direct PVDF membrane fabrication were investigated, including hot press and electrospinning methods. Hot press produced a visibly uneven membrane. Viewing scanning electron microscopy images, it can be seen that a membrane of approximately 100 microns was produced, which is too thick for actuator application. Additionally, pores running laterally through the membrane were not produced. The sample under SEM as well as the target pore size of 10-30 microns is shown in

Figure 2.7. Pores in the membrane allow for ion mobility in the polymer, which is necessary for actuation.

Electrospinning was investigated as a method of membrane fabrication which could be directly applied to previously constructed actuator layers to build the multilayered structure. Electrospinning produces many nano- to micro-sized fibers. These fibers build up on a substrate, producing a fiber mat. The morphology of fibers determines relative pore size and density in the membrane. PVDF solution was produced using PVDF 301F powder garunteed and 3 micron diameter from Kynar corporation with the addition of dimethylacetamide (DMAc) solvent in weight percents of 10-30%.

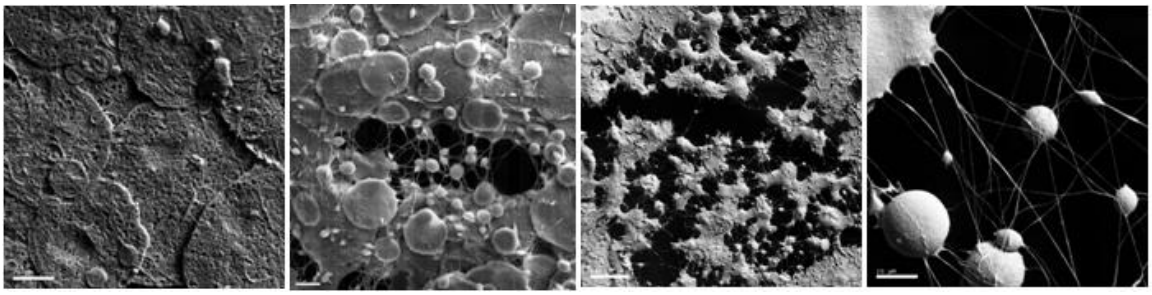

Figure 2.8: A variety of polymer morphologies were produced by varying electrospinning parameters

Figure 2.8 shows a variety of morphologies produced by varying electric potential between the syringe and collector in the electrospinning setup, polymer solution viscosity controlled by weight percent of DMAc solvent, distance between the syringe and collector, and solution feed rate as determined by syringe pump settings. "Lily pad" type depositions were produced at first when collector distance was too close or the solution contained too much solvent. As we move to the right in the inset figures, fewer lily pads are produced, and clear fibers are created by optimizing electrospinning parameters. Figure 2.9 shows the final result of creating a fiber mat with a lack of lily pad type features. Table 2.1 shows a summary of how fiber diameter changes with increased value of a parameter. For example, by increasing potential in the setup from 10 to 20 kV, we can produce a fiber with a decreased diameter.

This mat will next be coated with polypyrrole (PPy), a conducting polymer, to produce actuation in the structure. PPy is chemically applied in a solution of 10 mL 0.008 M pyrrole monomer, 20 mL 0.008 M p-toluenesulfonic acid, and 10 mL 0.008 M ammonium persulfate. PPy can also be electrochemically applied by cyclic voltammetry method, which produces a thicker coating, but with less predictable results.

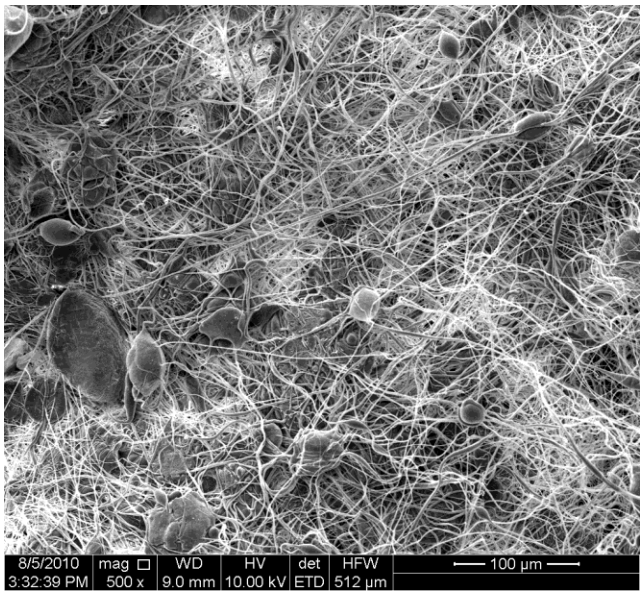

Figure 2.9: Fiber mat showing good characteristics such as lack of lily pad structures, small pore diameter, and high pore density

Table 2.1: Summary of parameter effect of fiber diameter

Parameter	Range	Fiber diameter
Potential	10-30 kV	↓
Solution viscosity	10-30 wt%	↑
Syringe-collector distance	8-23 cm	↓
Solution feed rate	0-5 ml/h	↑

Figure 2.10 shows a fiber mat before and after coating with PPy. From the magnified view of the PPy-coated mat, the rough morphology of the polypyrrole can be seen evenly coated onto the PVDF fiber. More work must be completed to fully characterize the effects of parameters on fiber diameter and the functionality of PPy coating. Multiple samples are being analyzed in order to produce graphs of parameter value vs. fiber diameter, pore size, and pore density in the fiber mat.

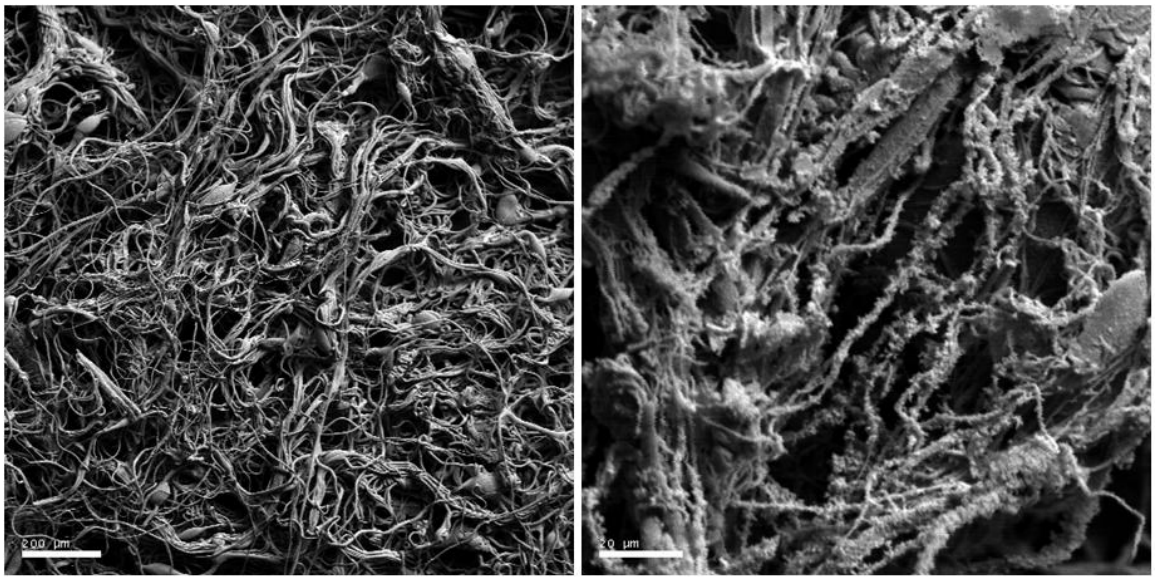

Figure 2.10: Dense fiber mat before and after coating with polypyrrole

2.3 PPy-Au-PVDF-Au-PPy multilayer actuators

Multilayer structures have been shown in 5-layer configurations (Gaihre et al 2011), however prior research did not demonstrate electrode connections required to achieve monolithic performance. In one study, layers of PPy film and ionic liquid soaked separators were layered to form a polymer actuator with scalable work output (Ikashima et al 2009). However, this structure was not fully connected and consisted of passive layers.

We aim to create a monolithic actuator, operable in air, with fast actuation times and increased force generation. There are essentially three methods by which a multilayer actuator can be created with more than one PVDF substrate layer (Figure 2.11). The simplest step in this direction would be to create multiple stripe actuators, polymerizing PPy on top and bottom, and then multilayer them with an adhesive. This concept is referred to as the addition method. The second method would be to build the substrate, in this case PVDF into the desired final configuration, before PPy is deposited. The various layers would have to be held apart by small spacers on the order of 1-10 μm. This method was thought to be too difficult due to small tolerances and the low rigidity of the PVDF films. The final method is that of direct application. This method uses a layer-by-layer approach to subsequently build each new level of the actuator upon the prior one. This method was investigated in this manuscript. Within the direct application method, alternative processing techniques were explored such as electrospinning of PVDF

fibers onto the prior substrate; however, electrospinning was found to have too large pore size, large pore density, and did not provide necessary structural rigidity. The doctor blade method was straight forward and was found to produce a fine pore size with high pore density.

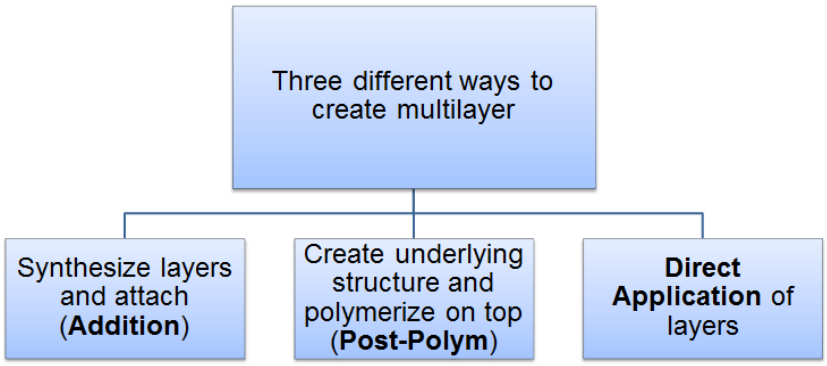

Figure 2.11: Three methods for creating multilayer actuators

2.3.1 Methods

PVDF film was initially created on glass lab slides with the doctor blade method. Magic Tape of 50µm was placed around the edges to produce the correct thickness of the PVDF film. Approximately 75% of the glass slide was covered with the PVDF melt. The solution was 25 wt% PVDF powder (Kynar Corp.) in 50/50 DMAc and acetone solvents. Samples were dried in air for 24 hr at either 25ºC or 80ºC on a hot plate. After the samples were dried, they were gold (99% purity) coated with a Technics Hummer V sputter coater for 6 minutes per side at a sputter current of 15 mA under vacuum.

Actuator strips were cut from the substrate in a size of 6 x 20 mm or 3.5 x 21.5 mm. Polypyrrole was electrochemically plated on 15 mm of the PVDF-Au film by the cyclic voltammetry method in a three electrode setup. The actuator was selected as the working electrode, platinum foil in the same dimensions as the counter electrode, and an Ag/AgCl as the reference electrode. A pyrrole monomer-containing aqueous solution of 0.25 M Pyrrole, 0.10 M TBAP and 0.5 M KCl was used. Deposition parameters were -1.3-1.5V at a scan rate of 100 mV per second. Fifty total sweep segments were produced over a period of 24 minutes. The cyclic voltagrams for PVDF films dried at 25ºC and 80ºC respectively are shown below.

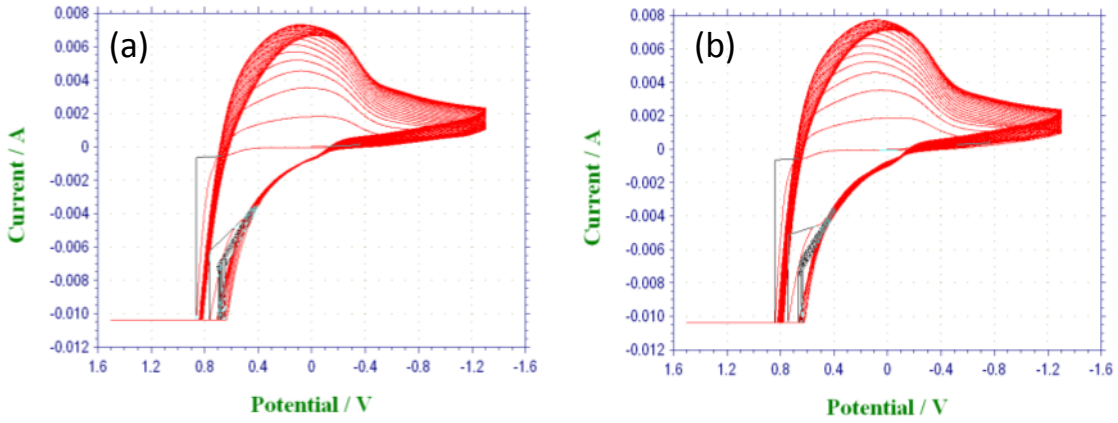

Figure 2.12: Cyclic voltammetry curves for 50 layers of PPy coating on a) 25ºC and b) 80ºC dried PVDF-Au films.

After electrochemical polymerization, the actuators were stored in either 3 M or 0.5 M KCl solution overnight until testing could be performed. Samples were actuated in air at 0-6 VDC by placing the 5 mm gold section of the actuator between two copper electrodes. Still images were taken with a digital camera in macro mode, no flash, at 5 megapixels and videos were recorded in macro mode at 15 fps. Tip displacements were obtained using a custom-designed MATLAB code with the Image Processing Toolbox functions. Scanning electron microscopy (SEM) characterization was performed with a LEO (Zeiss) 1550 high-performance Schottky field-emission SEM (FESEM) capable of resolution in 2-5 nm size range. For cross-sectional SEM imaging, polymer samples were broken after being cooled into a glassy state with liquid nitrogen.

2.3.2 Results

SEM characterizations were performed to measure sample thickness as well as understand the failure mechanism of the actuator. Due to this fact, SEM images were taken after the actuators had been actuated to failure. It was assumed that PVDF layered thickness does not change during this process since it is not the active material in actuation.

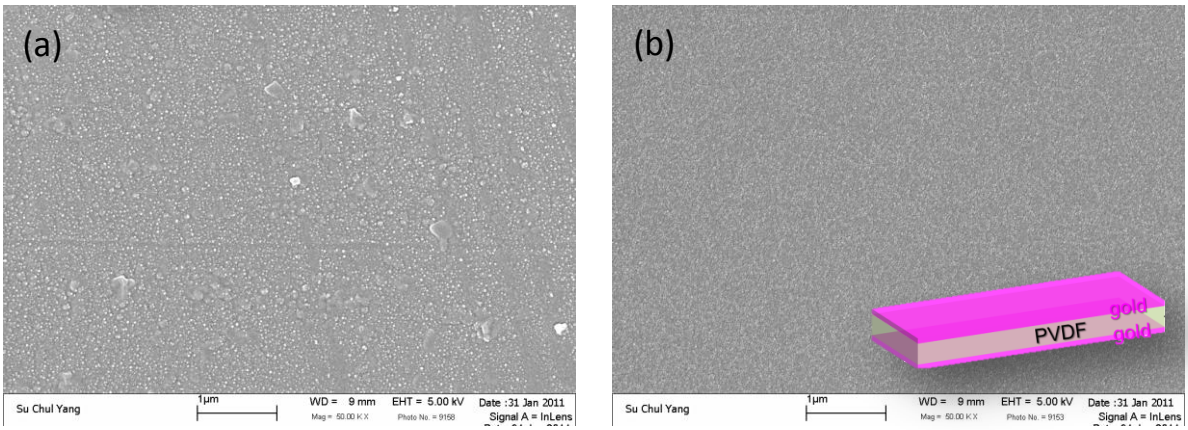

Figure 2.13: Surface morphology of (a) commercial and (b) laboratory-manufactured Au-coated PVDF film.

Commercial and laboratory-manufactured gold coated PVDF film SEM micrographs are shown in Figure 2.13 before PPy deposition. The commercial samples show a more uneven surface than the laboratory-produced films. A fine grain structure can also be detected in the images. The laboratory-produced film SEM image is similar for both 25ºC and 80ºC dried samples.

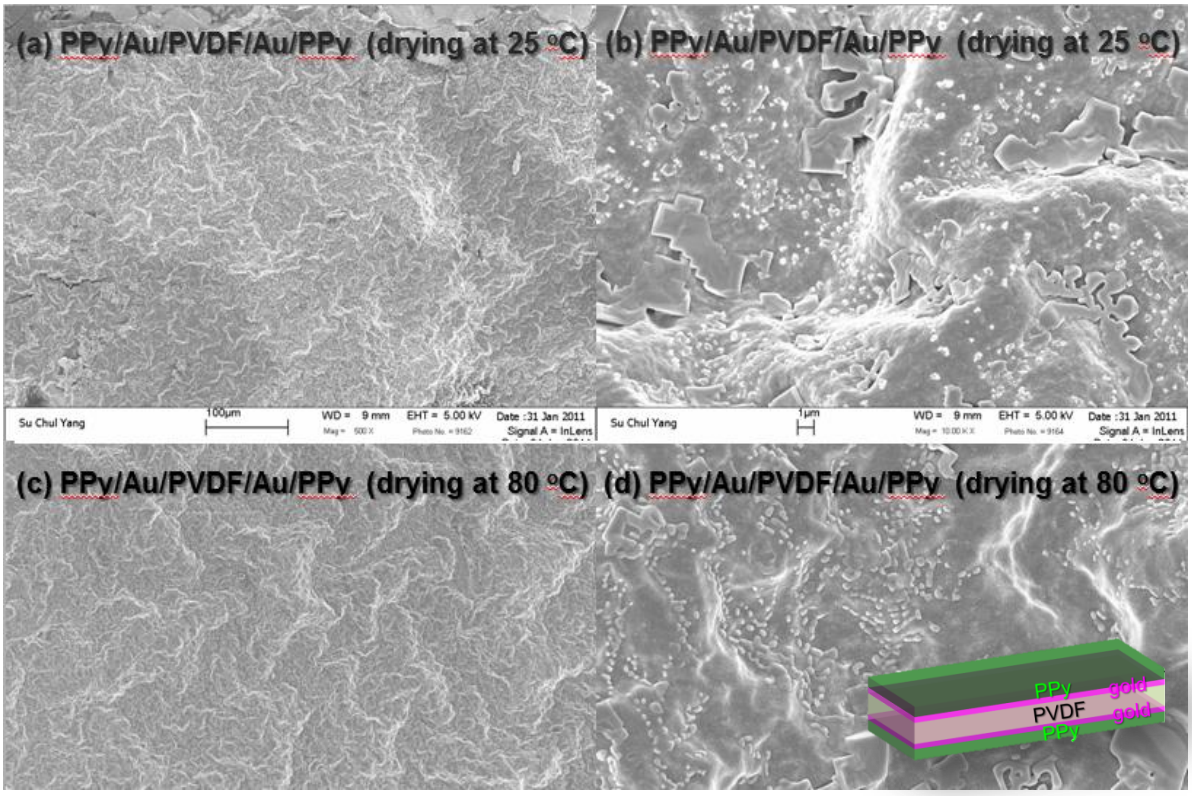

Figure 2.14: Surface morphology of PPy/Au/PVDF/Au/PPy actuators (a-b) drying at 25ºC and (c-d) drying at 80ºC

SEM images are shown in Figure 2.14 for the sample dried at 25ºC and 80ºC. The PPy morphology can be seen to remain fairly constant between the two samples. An interesting dense homogeneous structure can be noted rather than the common smoother globular PPy structure that can be seen in Figure 2.15.

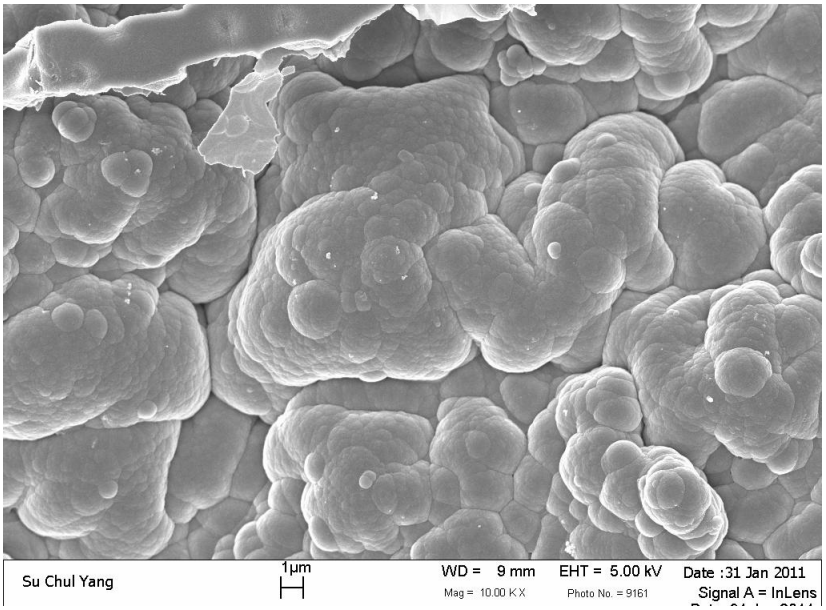

Figure 2.15: Typical surface morphology of PPy showing smooth and bulbous "cauliflower-like" structure

Cross-sectional images were taken to determine actuator thickness and provide a visual basis for actuator comparison. Initially, a commercial PVDF film was analyzed and found to have thickness of approximately 34µm. Figure 2.16 shows PVDF films synthesized with the doctor blade method and dried at 80ºC. Samples dried at 25ºC were similar and were also found to have thicknesses of 15-20 µm. It can be seen that after actuation the PPy no longer adheres to the PVDF substrate. In the SEM micrograph the PPy layer can be seen peeling off from the flat surface. Figure 2.17 also presents an image where the sputter coated gold layer can be seen separating from the PVDF substrate. The entire actuator structure was calculated to be approximately 60 µm in thickness including all of the layers. In the micrograph, the bottom layer is carrier tape.

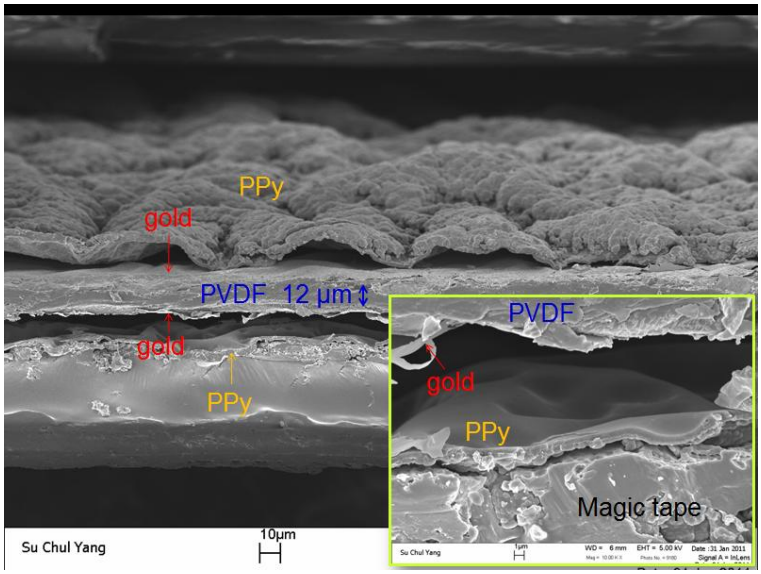

Figure 2.16: Cross-section of PPy-Au-PVDF-Au-PPy actuator dried at 80°C after voltage was applied.

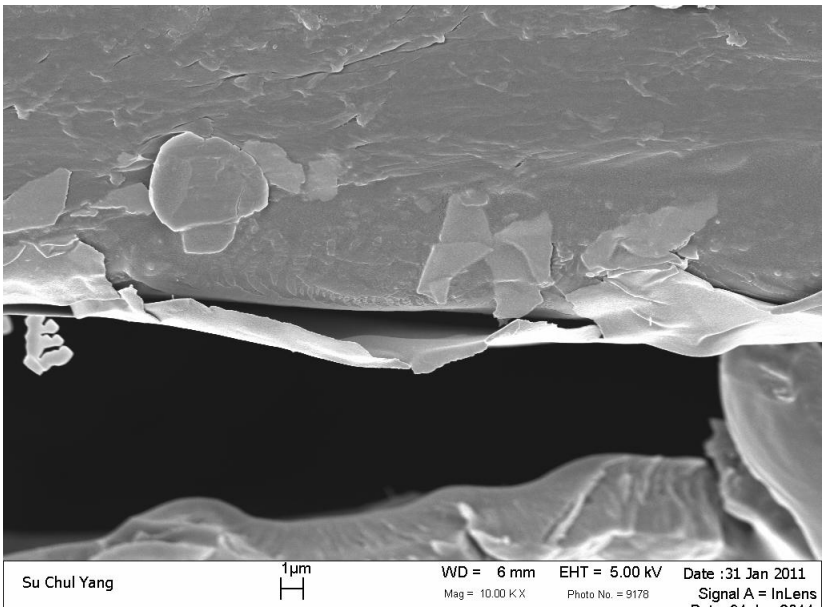

Figure 2.17: Close up SEM micrograph with delaminating gold and PPy layers.

Cross-sections of the PVDF membranes were taken to explore the pore size and density within the film. Commercially sourced film from Ktech Corp. was specified to have 0.1 – 1 µm pore size with a pore density of 10 - 60%. Figure 2.18 shows SEM images that revealed the true porosity of the commercial films as well as that of the laboratory-produced samples. Commercial film showed pore sizes of 0.1 to 0.3 µm while laboratory-produced samples showed pore sizes of 10 nm to 0.2 µm (inset close-up). The pore density was not analytically calculated but by visual inspection the pore density was higher

for samples produced in the laboratory than the commercial ones. Some of the variation in the microstructures shown in Figure 2.18 is due to the fact that the samples were cleaved in slightly different planes during liquid nitrogen treatment. The sample in Figure 2.18(b) was cleaved directly normal to the pore structure while that in Figure 2.18(a) was cleaved at an angle to the pore structure.

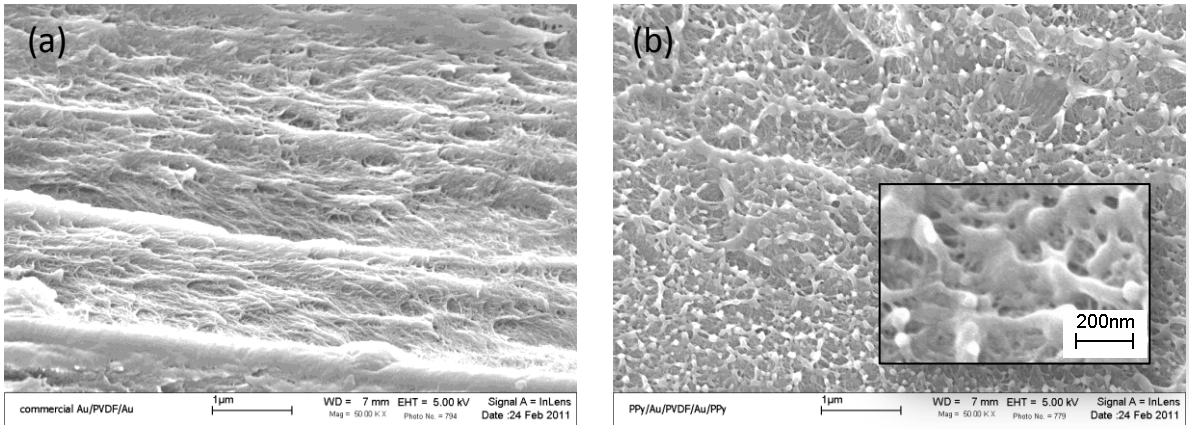

Figure 2.18: Cross-section of (a) commercial Au-coated PVDF film and (b) Au-coated PVDF film produced using doctor blade method showing porous structure.

Figure 2.19 is a superposition of two still images that were taken of the actuator driven under constant field and used to determine the deflection properties. Linear deflection was computed as the percentage of the total actuator length that the tip moved. The deformation over time was recorded in 15 fps video and run through a MATLAB program to extract the change in position (Figure 2.20). Composite video screenshots are shown with the initial and final states superimposed on top of each other.

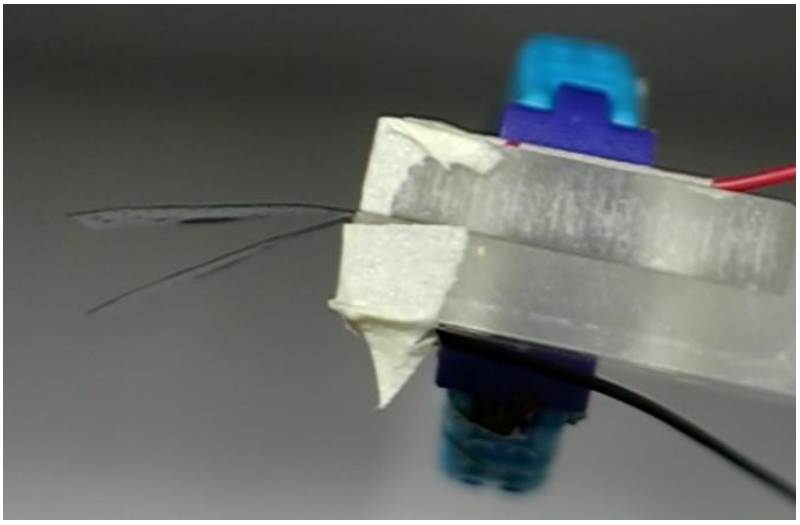

Figure 2.19: Overlay of the initial and final states of a 6 x 20 mm PPy-Au-PVDF-Au-PPy actuator stored in 3M KCl solution actuated at 6 VDC potential.

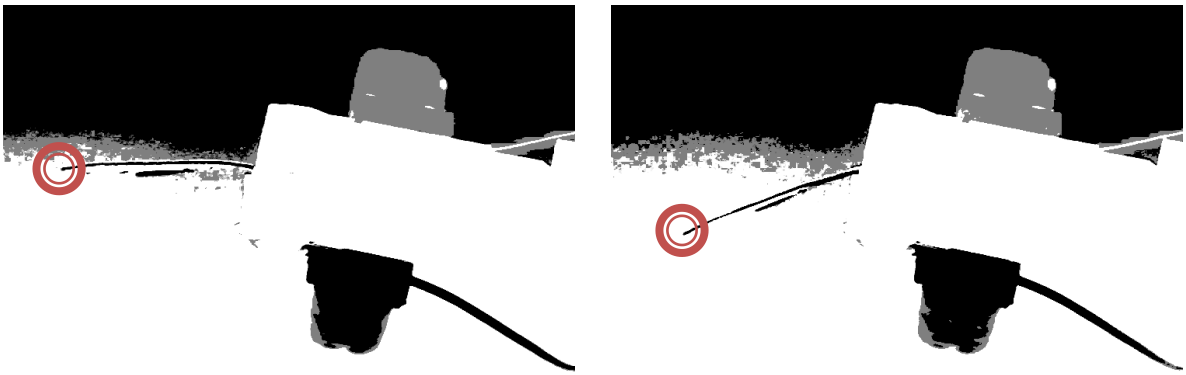

Figure 2.20: MATLAB image processing techniques were used to extract actuator tip displacement.

The maximum deflection achieved was 33% of original actuator length. Voltage was applied to the actuator for 30 seconds and the ions within the PVDF membrane and the conducting polymer layer were allowed to diffuse. Figure 2.21 shows the resulting motion of the actuator over time. One interesting aspect to note is that the actuator shows initial motion opposite to the desired direction. This is due to the differing diffusion time constants between cation and anion. Since the anion is much larger than the cation, it produces the eventual large deflection in the desired direction. However, since the cation is smaller it has a much faster diffusion rate. This implies that we see the initial movement in the opposite

direction because the cations are causing a larger volumetric change at the outset of actuation. That initial deflection accounts for a movement of 4.5% of the actuator length.

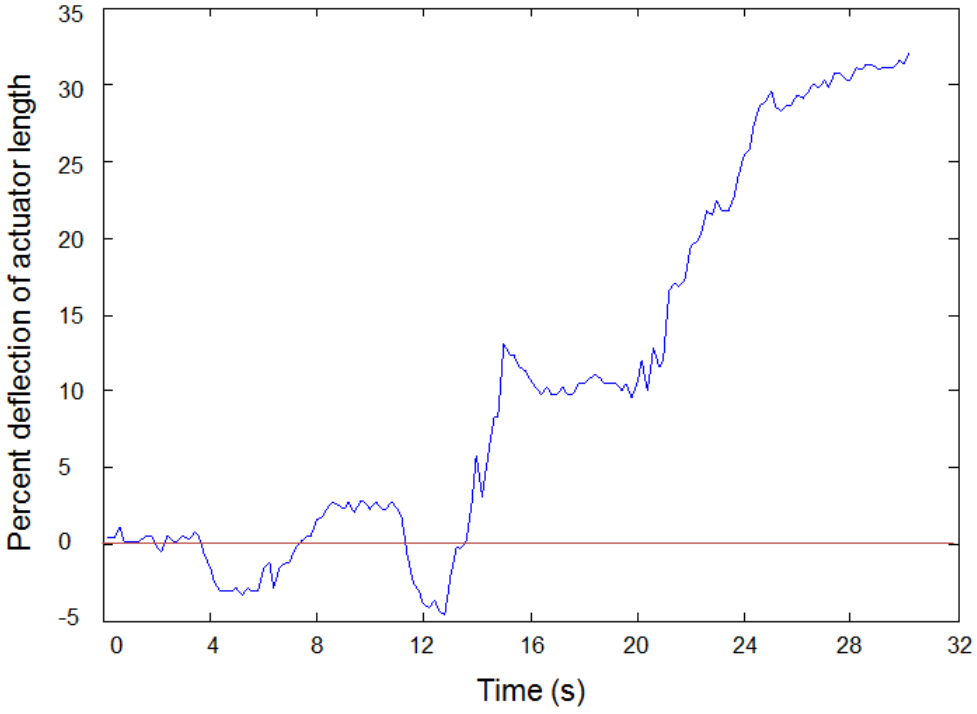

Figure 2.21: Deflection of actuator tip over time expressed as a percentage of total actuator length.

2.3.3 Optimization and high speed actuation

In order to reduce the damage, both a lower voltage and lower concentration solution was used to store the actuators. For further characterizations we used a slightly smaller actuator (3.5 x 21.5 mm) stored in 0.5 M KCl. The input potential was set at 4V. Video processing revealed that the actuator produced an impressive 90% tip deflection. In addition, the deflection rate was extremely high at 50% deflection per second. This rate was taken over the entire actuation cycle; maximum instantaneous deflection rates would be slightly higher than this magnitude.

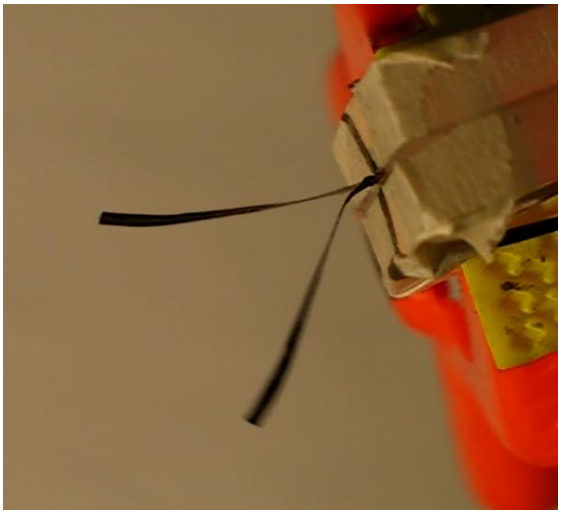

Figure 2.22: Overlay of the initial and final states of a 3.5 x 21.5 mm PPy-Au-PVDF-Au-PPy actuator stored in 0.5M KCl solution actuated at 4 VDC potential.

Initial attempts at creating a structure with multiple iterations of the 5-layer structure were met with some difficulty. The direct application method was used where subsequent layers of the actuator were built on top of each other. Glass slides were used as the substrate material. Actuators were developed following the methods outlined in previous sections. After the polymerization of PPy, another layer of PVDF was applied to the top. During drying the PVDF layer undergoes shrinkage in-plane which causes a delamination effect between the PVDF and the PPy layers. This is aided by the poor adhesion between the two layers. Attempts to apply an initial stress to the actuator film before application of PVDF melt were also not successful.

2.3.4 Conclusions and future work

Five layer PPy-Au-PVDF-Au-PPy actuators were produced to lay the ground work for multi-iteration actuators using the direct application method. Laboratory-created Au-coated PVDF membranes using the doctor blade method were found to have an even surface structure with a visible fine grain structure. The cross-section SEM revealed that the pore structure was similar to that of a commercial sample; however, it possessed slightly smaller pores with a higher pore density.

Stripe actuators under a potential of 6 VDC showed burning due to high potential and high concentration of storage electrolyte solution. An actuator was then produced that showed 90% deflection as a function of initial actuator length, with an extremely fast deflection rate of 50% per second over the entire actuation cycle and minimized burning. This reduction in burning was due to reduction in potential

to 4 VDC, as well as a reduction in storage electrolyte concentration to 0.5 M KCl from 3 M KCl. The large deflection and increased deflection rate was attributed to thin PVDF layer thickness, fine pore structure, and even coating of fine PPy layer.

The direct application method was found to work well for a single iteration actuator, while the adhesion between a polymerized PPy and newly applied PVDF melt layer was found to be very low. This created a delamination effect in the actuators with a larger number of layers. Multi-iteration actuators should be produced utilizing the addition method with the help of a fine, flexible aerosol spray adhesive.

Chapter 3:

Mechanical properties of mesoglea

In the next chapter, I describe the fabrication of a biomimetic jellyfish robot mimicking *Aurelia aurita* by using shape memory alloy composite actuators. Many of the soft robots being developed utilize standard engineering materials such as room temperature vulcanization (RTV) silicone to develop the body of the vehicles. RTV is an easy choice due to the availability of wide range of silicone types allowing for one to custom-select the correct formulation. In the next chapter, silicone was chosen for constructing the body of the biomimetic robotic jellyfish because thermosetting polymers could react adversely with the heat sensitive shape memory alloys used for actuation. Silicone is also hydrophobic and fairly cheap; however, RTV silicones are not neutrally buoyant and too stiff to appropriately mimic the dynamic elastic properties of biological materials. In this chapter, we focus on creating a nanocomposite hydrogel that could mimic the mechanical characteristics of jellyfish mesoglea. In the future we intend on using this novel biomimetic material instead of RTV silicone for robot body creation. Multiple types of mesoglea exist within a given species: bell and joint, subumbrellar and exumbrellar. The objective of this chapter was to design the nanocomposite hydrogel that surpasses the mechanical properties of the natural specimen. Emphasis was placed on understanding the mechanical properties of soft mesoglea and its effect on the propulsion. While doing this study, we found the scarcity of information in literature on mechanical properties of both swimming and flying animals. As a comparative study, we decided to investigate the mechanical property of any other natural species that can be readily made available in adequate quantity. In collaboration with Prof. Mueller's laboratory, we were able to locate bat wing's and thus we put our effort in characterizing its mechanical properties. This required development of an automated measurement system that can be used for a variety of biological materials and provide extremely good resolution due to the National Instruments FPGA used to collect high speed data. Thus, this chapter provides an important experimental data quantifying the mechanical properties of natural animals with varying characteristics.

3.1 Natural Mesoglea

In jellyfish, the mesoglea makes up a majority of the volume of the body (Arai 1997). In structural sense it acts as the "skeleton" of the animal. Interestingly though, mesoglea also serves as the main locomotor such as the wing skin of a bat or the mantle of a squid. In achieving this additional functionality, it is evident that the mechanical properties of mesoglea should play an special role in

jellyfish. Thus, we focused our attention on understanding the role of mesoglea which plays the dual role serving as both the structural and locomotor element.

Mesoglea is a jelly-like substance composed of long 20-50 nm diameter collagen fibers and a network of proteins and polysaccharides which span the space between them (Wang et al. 2011). It is found in the taxa Cnidaria and Ctenophora but in this study we are primarily concerned with the jellyfish represented in the classes hydrozoa, scyphozoa, cubozoa, and staurozoa. The collagen fibers that are radially aligned in relationship to the central jellyfish axis contribute towards the jellyfish's overall strength by broadly dispersing the stresses that are localized on the body. Figure 3.1 shows the SEM image of a freeze-dried collagen structure extracted from an *Aurelia aurita* jellyfish. The image shows the ordered block structure of mesoglea (Hermansson et. al., 2010; Yang et. al., 2008)

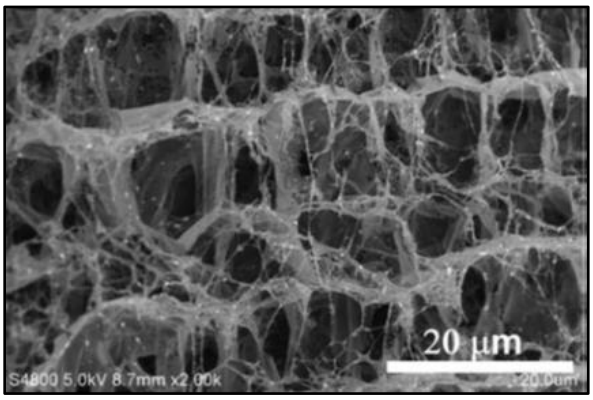

Figure 3.1: SEM micrographs of freeze-dried collagen fibers from jellyfish mesoglea. (Wang et al 2010)

The mechanical properties of natural jellyfish mesoglea have scarcely been investigated. The first attempts were a visco-elastic study by Alexander (1964) who concluded that jellyfish (Scyphozoa, *Cyanea and Chrysaora*) mesoglea was softer than that of previously studied sea anemones (Anthozoa). It had a "broad distribution of retardation times" and a slow creep recovery [describe what is retardation times]. Gladfelter (1972) investigated the bell mesoglea of *Polyorchis montereyensis* as a firm gel and the joint mesoglea as a much softer deformable gel that does not have liquid flowing properties [List the important results from Gladfelter's study]. Demont and Gosline (1998) found that intact jellyfish bell of the species *Polyorchis penicillatus* has modulus between 400 and 1000 Pa. Megill (2005) found the stiffness of *Polyorchis penicillatus* bell mesoglea to be 350 Pa in compression while the softer joint mesoglea had stiffness of 50 Pa. Wang et al. (2011) investigated the mechanical properties of the jellyfish *Rhopilema esculenta Kishinouye* but did not report a single stiffness value. In their study, it was found that mesoglea from natural jellyfish could be used in conjunction with artificial hydrogels in a hybrid structure. It can also be seen from these prior studies that reported values of modulus of mesoglea

vary over a wide range. This could be associated with the measurement technique and also the method of sample preparation. It is well-known that rapid changes in property of mesoglea occur as a function of time after it has been cut-off from the real animal. Further, there is no experimental data in literature on the modulus of *Aurelia* mesoglea. So the first objective of this work was to correctly determine the bulk properties of natural jellyfish mesoglea. Based upon these measurements, the second objective was to successfully synthesize synthetic hydrogels that can replicate the mechanical performance of natural mesoglea.

The rowing mechanism used by jellyfish involves sequential contractions of the bell mesoglea. In this case, compressive modulus provides a reasonable metric for characterizing the performance because natural mesoglea is usually under a compressive load during this free-swimming (Dabiri et. al. 2006). Jellyfish mesoglea can be transparent, highly hydrophilic, neutrally buoyant, biocompatible, and possess a low modulus while retaining durability (Arai 1997). These properties are partly due to the fact that mesoglea has such a high water content, near 96% (Lowndes 1942).

3.2 Artificial mesoglea

Much work has been done on synthetic hydrogels for a variety of purposes as diverse as tissue engineering (Shin 2008), superabsorbent polymers (Hermansson 2010), and gold ion reclamation into nanoparticles (Kumar 2005). Advances in durable hydrogels have opened the possibility of tailoring them for use in a biomimetic robotic jellyfish. This class of material is highly tunable by way of nanofillers and can be synthesized in many ways including freeze-thaw, radiation, and chemical cross-linking agents. Based upon the literature survey, we found that hydrogels can serve as good starting point towards synthesis of artificial mesoglea. Hydrogels are an aqueous gel network composed typically of a hydrophilic polymer, cross-linked either by chemical bonds or cohesion forces. When placed in water, hydrogels are able to swell rapidly and retain large volumes of water without dissolving. Despite high water contents, hydrogels are elastic solids that exhibit memory, a state to which the system can return after being deformed (Park et. al. 1993). Conventional hydrogels are usually mechanically weak due to their lack of ordered structure at the molecular level (Miyazaki et. al. 2002). However, recently there has been increasing interest in hydrogels with high mechanical strength and novel microstructures have been developed to achieve this aspect (Kopecek et. al. 1986). Wang et al. (2011) have developed hybrid hydrogels based upon the mesoglea structure of the jellyfish *Rhopilema esculenta Kishinouye* but with the intent of achieving higher mechanical strength than other synthetic hydrogels.

Using nanofiller composites was found to be a viable option in increasing the strength due to its sustainability. Ferritin was chosen as the candidate for nanofiller composite because of its structural

uniformity on the nanoscale. With a protein shell of about 2 to 2.5 nm surrounding a ferritin-iron core of about 7 to 8 nm, the particles can form network with polymer chains due to the carboxylic acid and the amino groups of ferritin shells (see Figure 1). Nanofillers can decelerate crack propagation, and delay complete failure of the composite hydrogel. Smaller filler particles increase surface area, which maximizes the interaction between filler and polymer matrix. Ferritin exists naturally in a biocompatible form in various animals, plants, and bacteria for maintaining iron (Shin et. al., 2009; Ohara et. al., 2009). Polymer nanocomposites based upon the ferritin also have the possibility to respond to external stimuli and be mechanically adaptive. These properties could theoretically allow the body of the jellyfish to change stiffness, diffusion properties, or electrical conductivity (Hsu 2011).

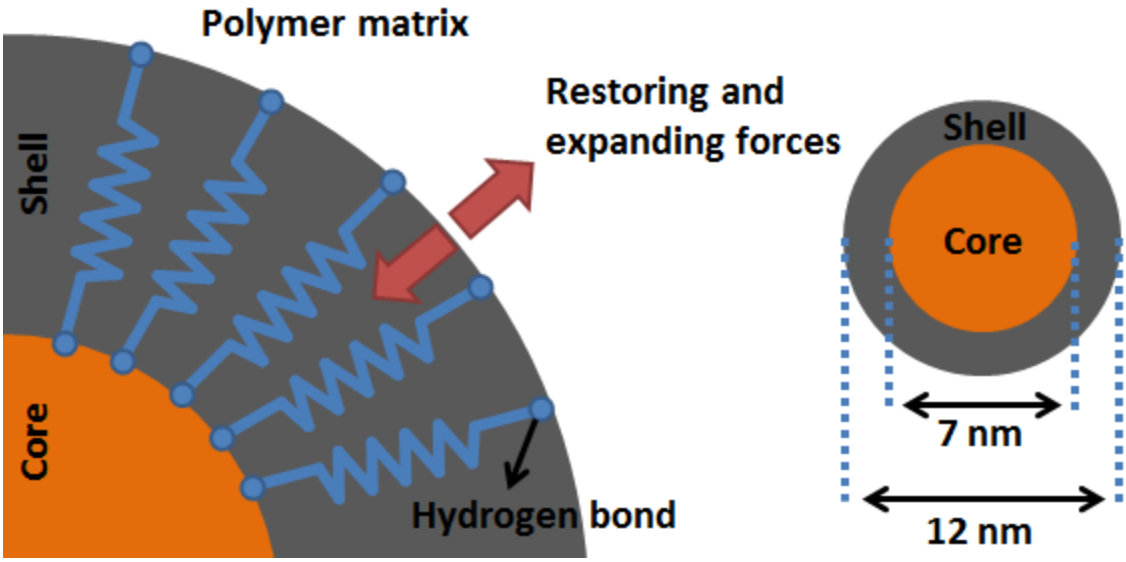

Figure 3.2: Elastic spring model of ferritin (protein) shell with ferritin (iron) core redrawn from (Shin et al 2009) and cross-section of a ferritin nanoparticle redrawn from (Ohara et al 2009)

3.3 Synthesis and characterization

Preparation of Poly(vinyl) alcohol (PVA) hydrogel (Y. Ikada et al 1989). A homogenous solution was prepared consisting of 15 wt% PVA with molecular weight of ~146,000. PVA was purchased from Sigma Aldrich (St. Louis, MO) and combined with a mixture of 18.2 MΩ-cm water and organic solvent dimethyl sulfoxide (DMSO). Mixing ratio of water to DMSO ranged from 50:50 to 90:10 by weight. DMSO with 99.9% purity (purchased from Sigma Aldrich) was thawed to room temperature liquid prior to use. Once PVA, water, and DMSO were combined, the solution was covered and stirred vigorously at 140 ^{o}C for two hours. After sufficient mixing, the solution was a clear gel. The gel was swiftly poured

into a mold, degased in a vacuum chamber, and then placed in a – 5 ^{o}C freezer for 10 hours to promote crystallization. The crystalized hydrogel was then placed in a flowing bath for 4 days, consisting of a constant supply of water to exchange DMSO in the gel with water (Hyon et. al. 1989).

Crystallinity has been found to increase with PVA concentration and freezing time, while the breakdown of crystalline structure was seen during the thawing process. (Miyazaki et. al., 2002; Peppas et. al., 1991) Additionally, PVA polymer with higher molecular weight was chosen because it has been found to increase crystallite size and overall phase. (Mandelkern et. al., 1967) Upon further examination, it was found that the structure consisted of three phases: a water phase with low PVA concentration, an amorphous phase, and a crystalline phase that restricts some of the motion of the amorphous PVA chains. Researchers have introduced organic solvents during the freezing and thawing process to promote greater crystallinity [Ref]. This occurs because during the freezing stage the molecular movements are restricted. The intermolecular nucleation of PVA begins at this stage with the initiation of hydrogen bonding. With the addition of the organic solvent, crystallization can proceed further because of the lowered freezing temperature and significant volume expansion. This yields a much stronger and more durable hydrogel than conventional PVA synthesis (Yokoyama et. al., 1986).

Preparation of PVA-Ferritin Nanocomposite hydrogel. This material was produced by using the method described above for producing PVA hydrogel. However, prior to mixing water with PVA and DMSO, 0.25 grams of undiluted stock (54 mg/mL) ferritin nanoparticles (type 1 from horse spleen) (purchased from Sigma Aldrich) was injected into 100 mL of 18.2 MΩ-cm water. The ferritin nanoparticle and water solution was sonicated for 5 minutes to ensure homogeneous dispersion. This mixture was then used in place of pure water in the standard PVA hydrogel preparation. PVA is a matrix for ferritin nanoparticles which are nanofillers. Other nanoparticles such as inorganic clays and carbon nanotube molecules have also been explored for improving the mechanical properties of hydrogels.

Preparation of EcoFlex Silicone. EcoFlex is a platinum-catalyzed silicone purchased from Smooth-On, Inc. (Easton PA). EcoFlex is a two part, 1A:1B mixture that cures at room temperature. Cure time can be decreased by increasing temperature. Because silicone was used for design of artificial mesoglea on the UUV discussed in the previous chapter, it was synthesised as the control material to compare the results against the PVA hydrogel.

Water content of natural Aurelia aurita jellyfish. Five samples of approximately 22 mm diameter *Aurelia* jellyfish were lightly rinsed to remove excess salt water. The samples were then allowed to dry in air for 120 seconds to remove the surface water. The pre-dried weight was recorded and then the samples

were exposed to light air flow under a fume hood for three days at which point the post-dry weight was recorded. After drying, salt crystals were observed on the samples, showing that the mesoglea was indeed carrying a large amount of sodium from the surrounding seawater.

Compression Strength of artificial mesoglea candidates. Compression testing was conducted on a Texture Analyzer manufactured by Stable Microsystems Ltd. The instrument was fitted with a 5 kg load cell with 0.01 N resolution. No ASTM standard for compression strength measurement of hydrogel materials or silicones currently exists. Therefore, the following method was developed by combining the guidelines from two existing ASTM standards that address compressive properties of rubbers and rigid plastics. ASTM D575 – Standard Test Methods for Rubber Properties in Compression and ASTM D695 – 10 Standard Test Method for Compressive Properties of Rigid Plastics were chosen as model methods because of the polymeric nature of the PVA and the rubbery similarities that silicone exhibits.

PVA and PVA-Ferritin hydrogels were compressed at a rate of 12.5 mm/min (0.5 ± 0.1 in/min) to a deformation of 50% the specimen thickness. 50% was chosen because naturally occurring *Aurelia aurita* has a maximum compressive deformation which does not exceed 50%. Specimens were cylindrical in shape with dimensions of 28.6 ± 0.1 mm in diameter and 12.5 ± 0.5 mm thickness. All tests were conducted in an environment of 23 ± 2 °C and 50 ± 6 % relative humidity. Compressive forces were applied twice to condition the specimen and readings were taken during the third applied compressive force. Conditioning was performed to ensure that any internal stresses created during the hydrogel manufacturing process were accounted in the measurement. Compression platens were sufficiently larger than all specimens to ensure no material exceeded the perimeter of the platens during compression. Additionally, 400 grit waterproof sandpaper was placed on the top and bottom surfaces of the compression platens to minimize specimen slippage during compression. All silicones were compressed at a rate of 1.2 mm/min to a deformation of 98%. Video recordings and image processing in MATLAB were used to measure the true compressional surface area for calculating stress.

Compression Strength of natural mesoglea. Natural jellyfish mesoglea was taken from *Aurelia aurita* specimens of around 30 mm in diameter. A sample of 28.6 ± 0.1 mm in diameter were cut from the bell. The thickness was measured in air by digital calipers for calculating strain. All tests were conducted in an environment of 23 ± 2 °C and 50 ± 6 % relative humidity. The same equipment and load cell were used to test both artificial and natural mesoglea. Similar to the artificial hydrogel methods, compressive forces were applied twice to condition the specimen and readings were taken during the third applied compressive force. Compression platens were sufficiently larger than all specimens to ensure no material exceeded the perimeter of the platens during compression. 400 grit waterproof sandpaper was placed on

the top and bottom surfaces of the compression platens to minimize specimen slippage during compression. Specimens were compressed at a rate of 1.2 mm/min to a deformation of 98%. Video recordings and image processing in MATLAB were used to measure the true compressional surface area for calculating stress.

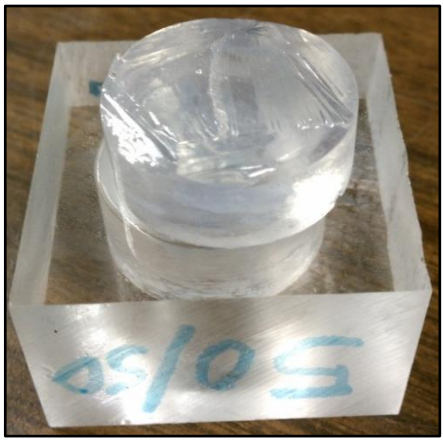

Figure 3.3: 50:50 (water:DMSO ratio) PVA hydrogel compression specimen.

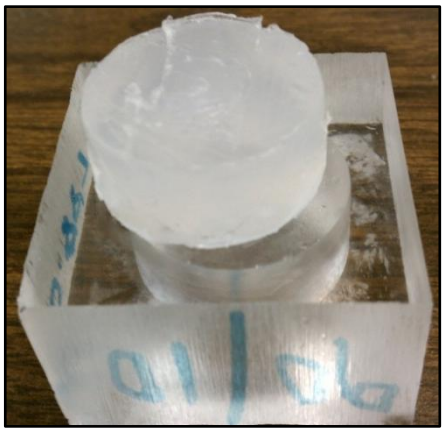

Figure 3.4: 90:10 (water:DMSO ratio) PVA hydrogel compression specimen.

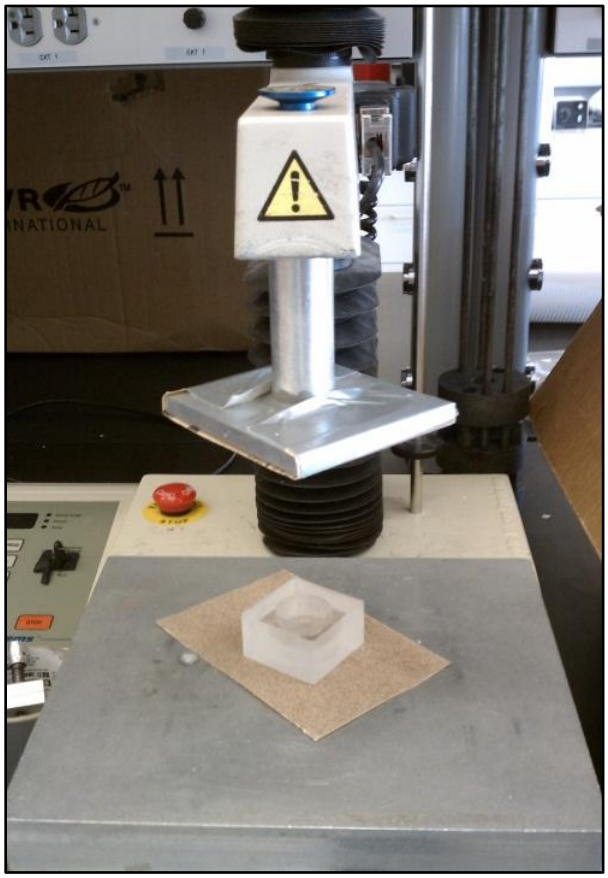

Figure 3.5: Stable Microsystems Texture Analyzer fitted with custom compression platen and anti-slip surface material (400 grit waterproof sandpaper).

Samples of hydrogels with and without ferritin were characterized for their dielectric properties. Small samples of approximately 5.5mm x 5.5mm x 2mm were cut from the larger blocks of hydrogel material. The material was assumed to be homogenous. The small samples were then allowed to dry in air for approximately 120 seconds to allow excess surface moisture to evaporate. The hydrogel squares were then placed between two parallel copper plates, also of dimensions 5.5mm x 5.5mm. This created a

capacitor-type structure with hydrogel dielectric in the middle. The samples were then mounted in a holder with two movable pins that could be tightened onto either side of the structure. Care was taken to keep the copper plates in parallel with each other. A frequency sweep of capacitance was taken with an impedance analyzer from 500 Hz to 1 MHz. This returned capacitance values, Cp, over that prescribed range. These values were normalized with the C0 value for each sample, calculated by the equation:

$$C_0 = \varepsilon_0 \frac{A}{t} \tag{1}$$

where ε_0 is the permittivity of free space 8.854 x 10^{-12} F/m, A is the planform area of the sample, and t is the thickness. The dielectric constant or relative permittivity, ε_r', was then calculated by:

$$\varepsilon_r' = \frac{C_p}{C_0} \tag{2}$$

3.4 Experimental Results

3.4.1 Optical Clarity

Prior to mechanical and dielectric testing, hydrogels with various water to DMSO ratios were synthesized and visually inspected to determine if light transmittance varied in accordance with published data as well as to determine how physically durable the material is while being handled. Figure 3.6 shows the percent light transmittance over a range of water to DMSO ratios. The figure contains PVA hydrogel samples (without FNP reinforcement) with four different water to DMSO ratios and their optical transmittance change. The optical clarity is increased drastically with increased DMSO content. The addition of more and more water seems to cloud the hydrogel samples.

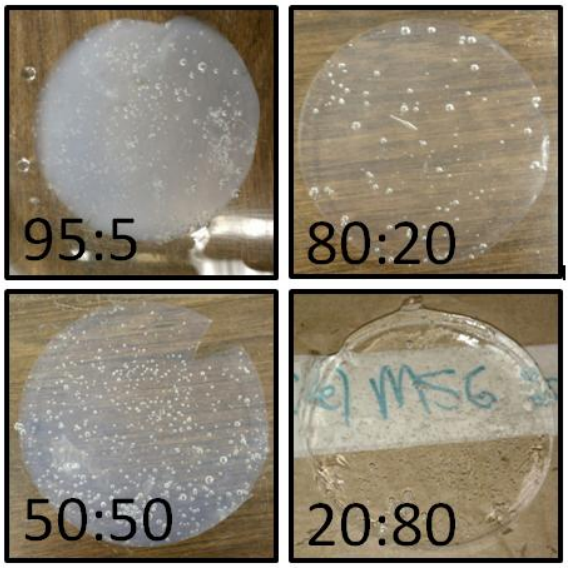

Figure 3.6: PVA hydrogel samples with various water : DMSO ratios (95:5, 80:20, 50:50, 20:80)

3.4.2 Compression Strength Testing

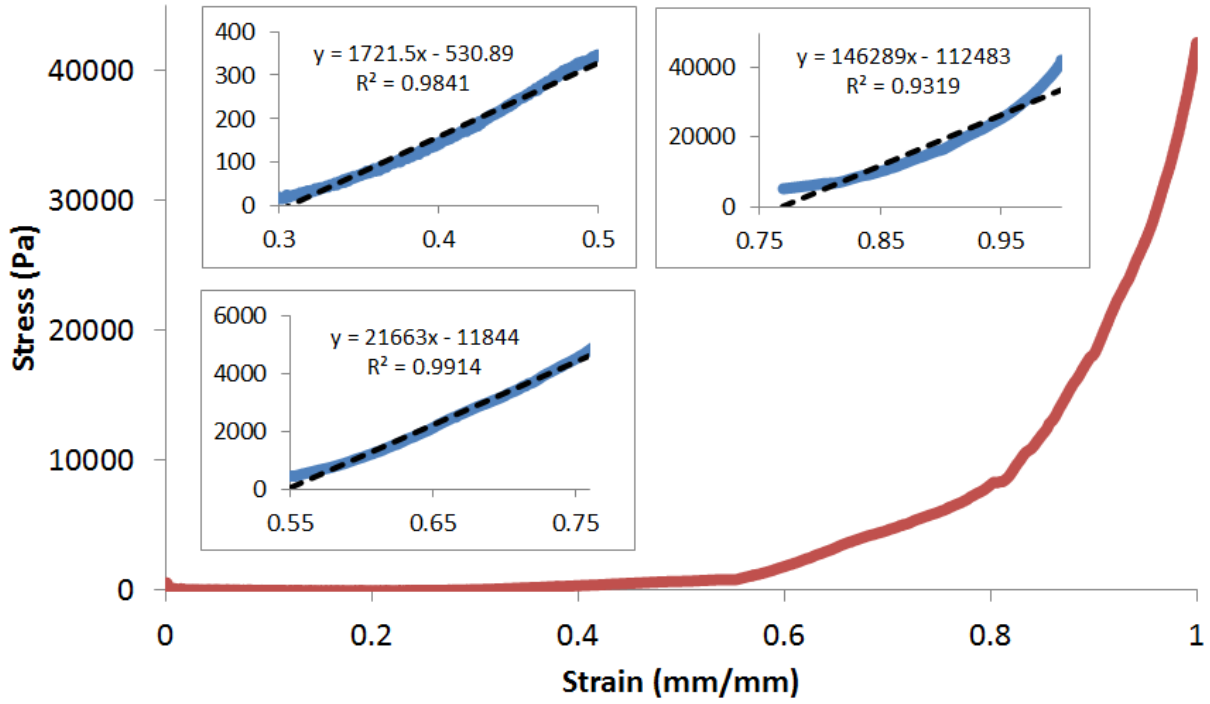

Figure 3.7: Stress-strain curve and varying moduli of natural *Aurelia aurita* jellyfish mesoglea. A center of the bell portion with flat upper surface was used for this test.

The Young's Modulus of natural *A. aurita* jellyfish mesoglea was found to be highly variable. Between 30% and 50% strain, the modulus was 1.7 kPa which compares well with most of the prior data. Above 50% strain, however, the mesoglea stiffens quickly. Between 50% and 75% strain the modulus was found to be ~22 kPa which is in the same domain as synthetic mesogleas that we developed. Above 75% strain, the mesoglea becomes very stiff and shows a modulus of about 150 kPa. Water was found to secrete out of the tissue at around 75% to 80% strain which may explain why there is a large increase in modulus after this value. According to the results from Villanueva et al. (2010(BISMAC paper)), the natural animal is expected to have a mesoglea compression of around 42% during a swimming cycle. This measurement is relative to the bell diameter in the relaxed position. Water content in the natural AA jellyfish mesoglea was measured. It was found to be 96.3% with a standard deviation of 0.57% compared to the 85% water content of PVA-ferritin hydrogels. Compression strength of PVA hydrogel and PVA ferritin nanocomposite hydrogel for various water to DMSO ratios is shown in Figure 3.8 and 3.9. The different water to DMSO mix ratios such as 90% water and 10% DMSO is denoted as the percentage of water only ("90"). All strains are shown to 50% due to the maximum compression seen in jellyfish natural mesoglea.

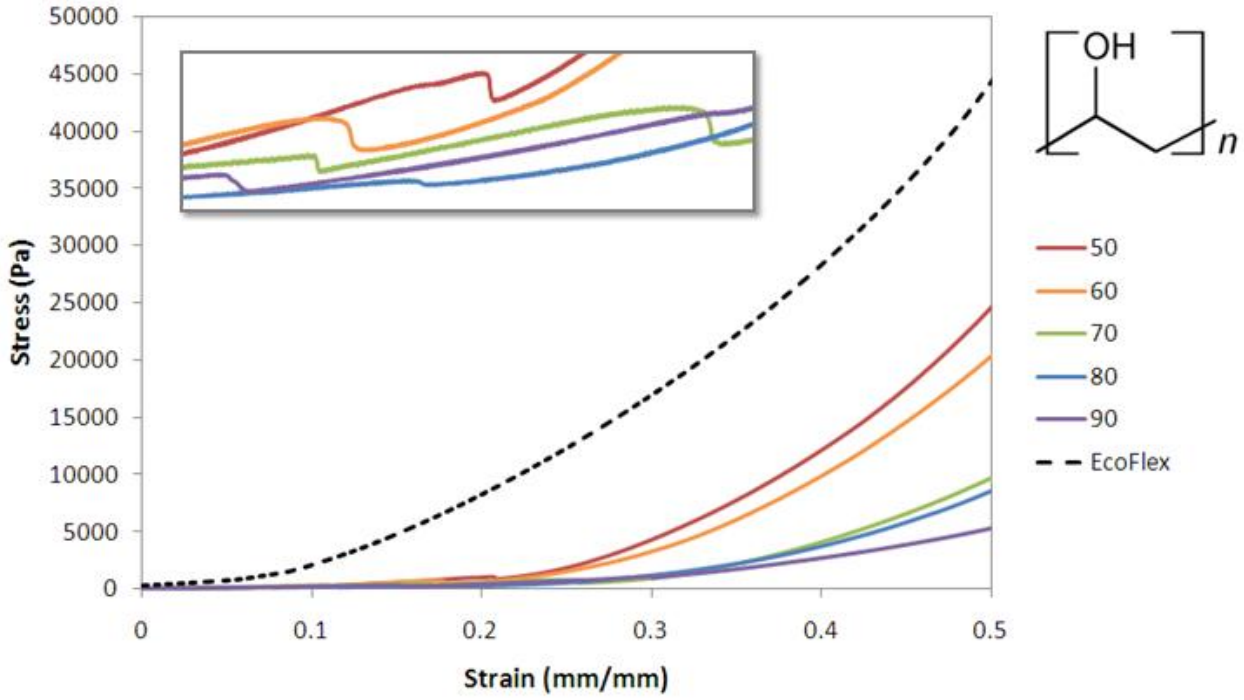

Figure 3.8: Compression of PVA hydrogels of varying water content

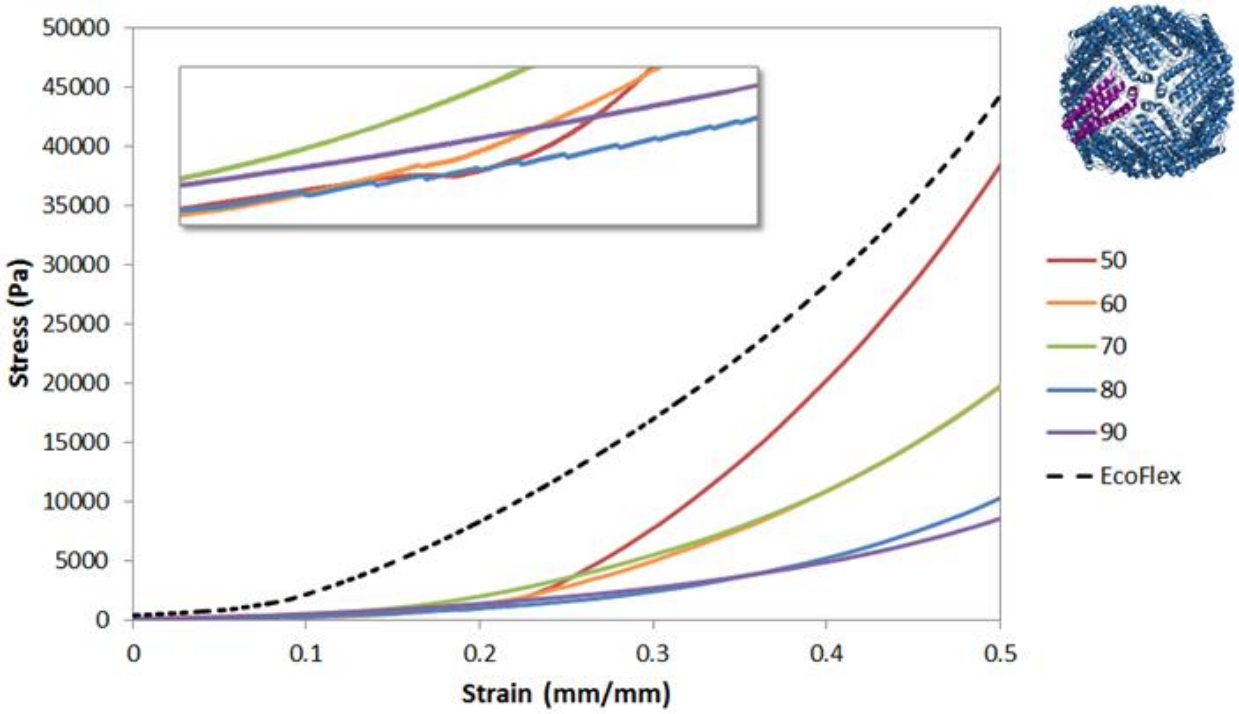

Figure 3.9: Compression of PVA hydrogels of varying water content with ferritin nanoparticles

PVA hydrogels exhibited non-linear behavior similar to that of the natural jellyfish mesoglea. There was a wide range of stiffnesses depending on water to DMSO ratio. A higher water to DMSO ratio lowered the stiffness of the material. The addition of FNPs increased stiffness of the hydrogel if water to DMSO ratio was held constant. The addition of FNPs also eliminated micro-failures in the hydrogel. These can be seen in the blowup in Figure 3.8, but are greatly reduced in Figure 3.9.

3.4.3 Dielectric Constant

Figures 3.10 and 3.11 are the dielectric constants of PVA hydrogel with and without FNP, respectively, reinforcement over ~ 500 kHz range. The dielectric constant for 90:10 PVA without FNPs was the highest, while for PVA with FNPs, 50:50 was the highest.

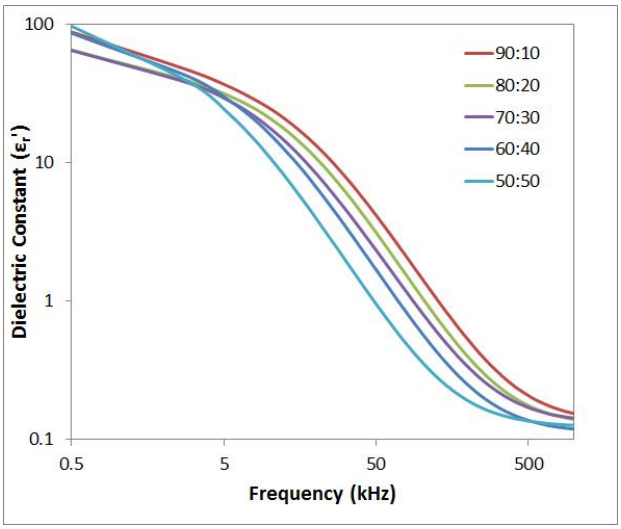

Figure 3.10: Dielectric constants of PVA hydrogels.

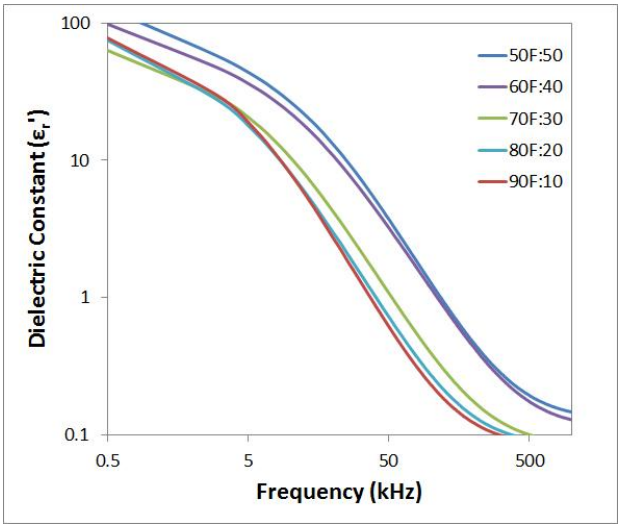

Figure 3.11: Dielectric constant of PVA-ferritin nanocomposite hydrogels.

All hydrogels produced followed a clear trend of increasing optical clarity with increased DMSO content. Stiffness increases inversely with the water to DMSO ratio in PVA hydrogels with and without FNP reinforcement. In general, ferritin increased the modulus of the hydrogel, while also increasing resistance to breakage. It can be seen in the magnified region of figure 3.8 that small ruptures were encountered during testing of the hydrogels without FNP. The stress builds slightly and then rapidly decreases. In the hydrogels with FNP, this effect is greatly reduced which can be seen in the Figure 3.9 blow-ups.

The hydrogels with the highest water content begin to enter a region where they emulate the measured mechanical properties of natural AA jellyfish mesoglea. According to the experimental data shown, PVA hydrogels with around 90% water to DMSO ratio provide a good alternative mesoglea. At 50% strain, the stress in the hydrogel is about 20% that of the Ecoflex RTV silicone. This will reduce the amount of power needed in actuators to propel an aqueous robot constructed of artificial jellyfish mesoglea.

In all the experiments conducted in this study, Ferritin was held constant (0.25 g in 100 mL). In future studies, testing will be required to determine an optimal concentration of nanofiller. Too much nanofiller or too little will likely degrade the material properties and thus an optimization study will be required. Currently, all hydrogels produced are denser than water. Future developments should determine the inherent buoyancy of PVA hydrogels and assess the materials ability to perform as desired in salt water environments.

PVA hydrogels have a stiffness between that of living jellyfish mesoglea and silicone. Outside of water environment jellyfish are very fragile so this may be a desirable compromise. Megill's (2002) results yielded joint mesoglea possessing a stiffness of 130 Pa while the bell mesoglea was 352 Pa. The species he used for testing was *Polyorchis penicillatus*. Compared to an *Aurelia aurita*, the *Polyorchis penicillatus* is much smaller and uses jetting method of swimming. *Aurelia aurita* uses rowing and can grow up to 10 times the size of *Polyorchis penicillatus.* Also, Megill's samples were fixed before testing which most likely would have altered the material properties. Our results indicate that jellyfish mesoglea is stiffer by an order of magnitude than Megill previously reported. Additionally, PVA hydrogels, both with and without FNP, with high water to DMSO ratios can adequately match the stiffness properties of natural *Aurelia aurita*. 90/10 water to DMSO PVA hydrogel matched well with the natural material due to a similar modulus in the range of natural compression. FNPs caused the dielectric constant for the regular PVA hydrogels without FNPs to be flipped in order for PVA hydrogels with FNPs. This is most likely due to the carboxylic acid and amino groups dispersed throughout the polymer network. Water content was not varied in this study, instead the water to DMSO ratio was varied which resulted in different mechanical properties. In future, this ratio as well as water to PVA content could be varied to fine tune the properties of artificial mesoglea.

3.5 Summary

A PVA based hydrogel is a promising base material for artificial mesoglea. Mechanical similarities exist between the PVA hydrogel reinforced with FNPs (a nanofiller which acts like elastic nanosprings) and biological mesoglea (a fiber reinforced tissue) that warrants its use as a synthetic mesoglea on the jellyfish platform. However, issues may arise when the material is exposed to electrical circuitry due to its high water content. The high water content may prove to be a problem if it causes shorting in the electrical conductors. Because of variable mechanical properties, it is possible for PVA hydrogels to be altered to match specific locations on the UUV platform. More specifically, softer sections of joint mesoglea can be replicated by varying DMSO and nanofiller content to allow for folding during rowing contraction, which is seen in rowing jellyfish. Modulus pairing between artificial and natural mesoglea for specific regions on the platform is a potential topic of future research. Additionally, saltwater stability and absorption must be addressed to ensure that the outer layer does not degrade during use.

Chapter 4:

Architecture, design, and characterization of robotic jellyfish

4.1 Artificial Muscle Characterization

Various SMA-based composite actuators have been reported in literature with varying magnitudes of blocking force and displacement. Turner et al (2001) have demonstrated a glass-epoxy laminate composite with embedded SMA ribbon which exhibited characteristics useful for adaptive stiffening of aerospace structures. Shahinpoor and Wang (1995) have proposed designs for large-motion from SMA actuators. One of their designs uses an SMA fiber bundle arranged in parallel configuration inside a helical compression spring with flat ends. A cylindrical composite with a flexible beam and thin-wall elastic tube has been shown to exhibit large bending deformations (Wang and Shahinpoor 1997). However, these prior designs are unable to meet the requirements of force, displacement, and energy density required for mimicking the propulsive system of medusa. Biomimetic and bio-inspired robots require actuators that are low profile, consume a small magnitude of electrical power, and have performance resembling that of natural muscle.

Recently, bio-inspired shape memory alloy composite (BISMAC) actuators have demonstrated the ability to translate the relatively high-force (70 gf) and low-strain (4%) of SMA wire into low-force and giant bending deformations (Villanueva et al 2010). BISMAC actuators were developed for use in unmanned undersea vehicles (UUVs) inspired by jellyfish species *Aurelia aurita* which requires axial displacements up to 42%. The requirement for actuators in these applications is large tip displacement with small net force as they are submerged in water and benefit from buoyancy (Denton and Shaw 1961). BISMAC actuators have the tremendous potential to be configured in multiple composite variations to realize complex deformation profiles. Further, the surface of BISMAC is hydrophobic which makes them directly operable in water. This opens up the possibility of developing various robotic systems such as biomimetic jellyfish (Villanueva et al 2010), hexapod stick insect (Espenschied et al 1993), mechatronic fish propelled by its tail (Liu et al 2005), and a ray with oscillating fins (Clark and Smits 2006). SMA-based actuators have been previously deployed in two underwater robots: a lobster (Ayers et al 2000a) and lamprey (Ayers et al 2000b). Both of these applications will be impacted by the advancement made in

design and fabrication of BISMAC actuators. BISMAC is a polymer – metal composite consisting of 50% Ni-50% Ti SMA wire and thin medium carbon steel embedded in a low durometer (Shore 10A) platinum cure silicone. Figure 4.1 shows a high magnification micrograph of the BISMAC actuator characterized in this study. In this specific sample, four SMA wires 150 mm in length and 0.01 mm in diameter were held at a constant distance of 2.2 mm from a strip of 150 x 6 x 0.1 mm spring steel.

BISMAC actuators have been shown to provide a large non-linear deformation which can be easily tailored by varying the composite structure parameters and material properties. In this way, hysteretic contraction and expansion cycles can be tuned to replicate the propulsive cycle of medusa which makes BISMAC an ideal candidate for undersea bio-inspired robots. However, the fundamental understanding of physics governing this deformation has not been achieved. It is obvious that when a BISMAC beam is undergoing bending deformation, the region under the neutral axis is experiencing compression while the region above it is put into tension. But the question arises, "What is causing this deformation?" It is also obvious that silicone compression is due to SMA contraction, but is this result of friction between SMA and silicone or is this due to compression occurring from a tip load induced by the terminal end where SMA is connected to the spring steel? In this chapter, we answer these questions and compare the performance of BISMAC actuator with other potential artificial muscle candidates suitable for UUVs.

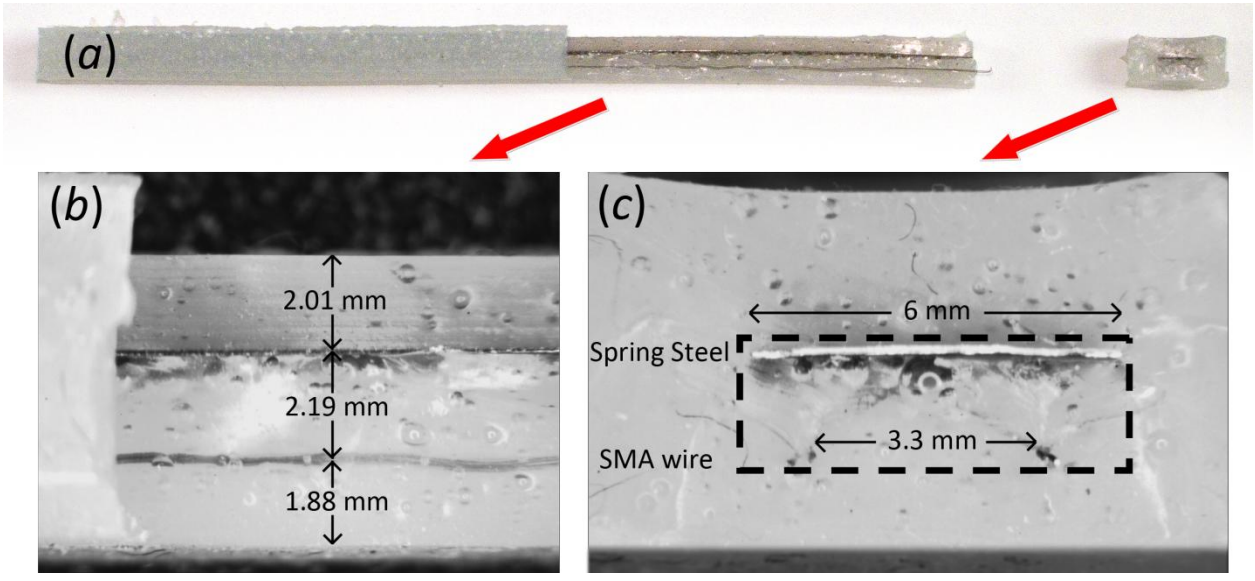

Figure 4.1: (a) Picture of monolithic BISMAC layered structure. Microscopy of internal structure of BISMAC actuator 175 x 12.7 x 6.0 mm showing (b) side-view and (c) cross-section with active dashed region.

In a sequence of experiments, all the possible components contributing to SMA tip attachment were removed one at a time to determine their individual impact on resulting curvature. The deformation profiles and schematics of the different tip configurations are shown in Figure 4.2. A constant current of 0.6 A was used to actuate the SMA wires for 40 s in all configurations. The two pairs of SMA wires in BISMAC were electrically connected in series. For characterization of the displacement, BISMAC actuators were mounted in a vertical position with free tip facing downward (fixed – free cantilever beam structure). The actuators were tested in air instead of water eliminating the requirement of a sealed tip and thus allowing easy access to SMA wires and attachment points. First, the constant cross-section BISMAC was actuated in its usual configuration with all the components present. Second, the tip silicone was removed and the actuator was characterized in its new configuration. Third, the spring steel connection was removed which consists of spring steel strip bent at the tip and SMA wires passing through it via a small hole. Lastly, a gap corresponding to 4% of SMA active length was added between the silicone tip and crimped attachment point. This allowed the SMA wire to contract and slip through the maximum 4% strain without creating a tip load. BISMAC deformation was digitized by tracking reflective points on the actuator in custom-built MATLAB code. Removing the silicone seal reduced the deformation by 7.64%. Removing the spring steel connection had a drastic effect on deformation with a loss in performance by 41.3%. Similarly, creating a loose segment between the crimp and silicone further reduced the deformation with a total loss of 89.6%. During this experiment, it was observed that the length of SMA wire had fully retracted inside the silicone upon actuation. The results in Figure 4.2 clearly show that tip attachment plays a dominant role in achieving full BISMAC deformation. The configuration with loose SMA wires resulted in slip in the silicone upon contraction. Tip loading contributed to most of the deformation while a small percentage of deformation still occurs due to friction between SMA and silicone. Deformation due to friction was below 10.4% but this does not reflect the friction force produced in the beam in a fully curved configuration.

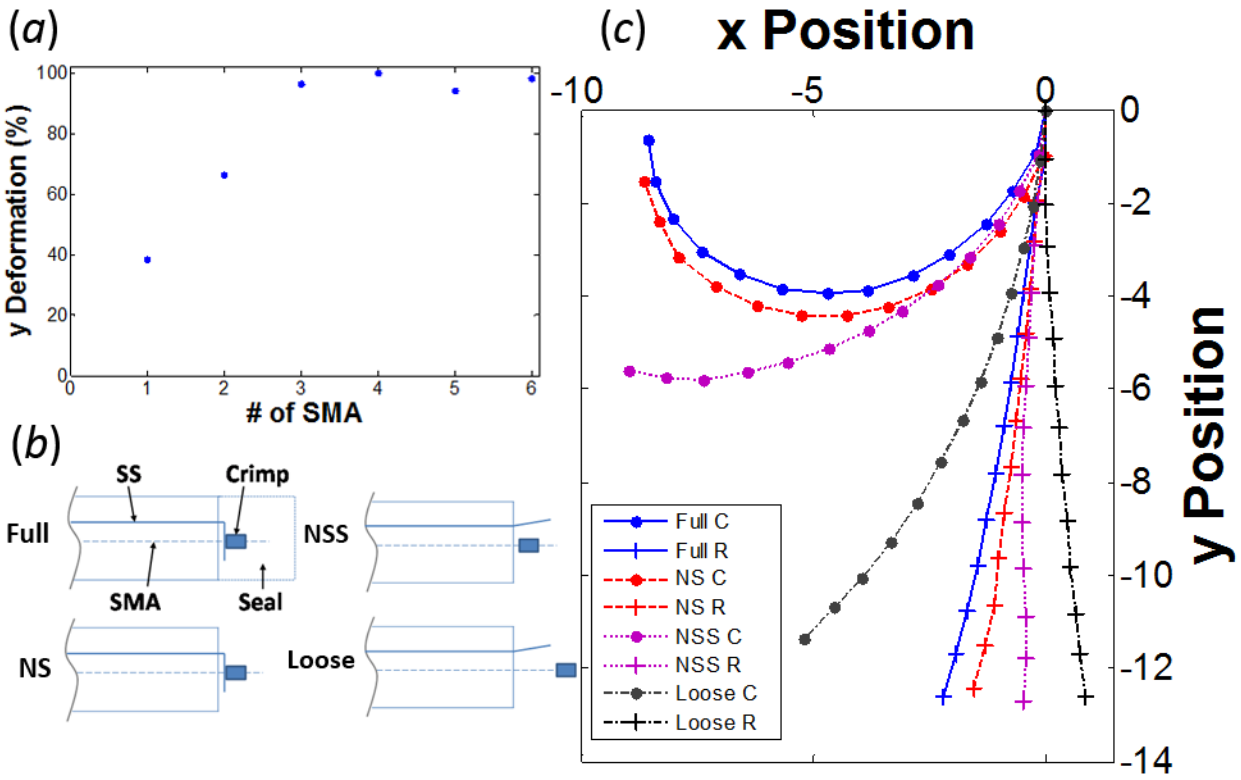

Figure 4.2: (a) Percent deformation in the y-axis as a function of number of SMA wires present in the actuator, (b) Schematic of full tip (Full), silicone seal removed (NS), spring steel attachment removed (NSS), loose between silicone end and crimp (Loose) tip configurations. (c) Contracted, C, and relaxed, R, BISMAC deformation profiles for all tip configurations.

BISMAC curvature is limited by strain and force capabilities of SMA wires. Previous experiments have shown that four SMA actuators of 100 µm diameter are capable of producing high deformation (Villanueva et al 2010). These SMA wires were capable of contracting 4% and achieving a force of 70 gf. Current BISMAC theoretical models do not properly capture the full behavior of the SMA. As a result, it is not known if BISMAC curvature is limited by maximum SMA stress or strain. Verification was conducted on a new BISMAC actuator which had initially 6 SMA wires. Each configuration was fabricated by using the same BISMAC and by removing one SMA wire at a time. In each case, the crimps at both ends were removed and new ones were attached after removing the SMA. It is noted that this could potentially create a change in pre-tension in the wires from one configuration to the next and contribute a small error to the final deformation profile. BISMAC actuators typically have two channels each containing two SMA wires. For this experiment, symmetry in the placement and number of SMA in each channel was desired for homogeneous deformation and load application on the composite. All SMA wires were connected in parallel with one electric terminal at each end of the BISMAC. For odd numbers of SMA wires (1, 3, 5), symmetry was not possible between the two channels. In the case of 5 SMA wires for example, two SMAs were in one channel having contact with

each other while the other channel housed 3 SMAs. Current distribution was even in each SMA wire for all configurations since they were connected in parallel. This allowed for an even contraction in all the SMA wires but with a slightly off-centered resulting load. The effect of the off-centered load had minimal effect on BISMAC curvature and was therefore neglected in the analysis. The SMA wires were heated with constant current of 1.3 A until no further contraction was observed. Actuation time varied from 6 to 69 s for 1 SMA to 6 SMAs, respectively, which is due to the difference in net power.

Figure 4.2 (a) shows the deformation results for BISMAC with different numbers of SMAs. The results show that for three SMA wires and more, the deformation of BISMAC is relatively constant. The percent deformation in the y-axis varies between 94.3 and 100%. This deformation is the total displacement in the y-component normalized to the maximum. The maximum deformation was achieved with four SMA wires and the initial deformation was taken as the tip position before the actuation. With two SMA wires, the deformation was significantly less equal to 61.6 % and with only one wire the deformation becomes even smaller equal to 33.6%. Deformation hardly changes for 3, 4, 5 and 6 SMA wires and any variation is mainly due to slight changes in initial pretension of the SMAs. Based on these experiments, the changes in force can be ruled out as the dominant factor for deformation in configurations with higher number of SMA wires. The limiting factor was found to be maximum 4% SMA wire contraction in these cases. For the configurations with one and two SMA wires, the limiting factor was force as they are unable to attain maximum contraction. Since three SMA wires are strong enough to achieve a full contraction in the BISMAC actuators, we know that the standard four SMA wires will provide force in excess of 70 gf. This is a very interesting result providing insight into the working mechanism of BISMAC actuators.

Figure 4.3 shows the test setup used for measurement of force and displacement characteristics of BISMAC actuators in underwater conditions. The actuators were naturally water-resistant as they are encapsulated in hydrophobic silicone material (Tadesse et al 2009). A thin nylon monofilament was attached on both sides of BISMAC actuator tip. These filaments rise from the top of the water tank where they are fed over two pulleys. The role of two filaments was to reduce any torsional effects that a misplaced single connection point would produce in the actuator. After passing over the pulleys, the two filaments join together and are attached to a mass which creates a force that opposes the downward bending actuation. Power was applied at a constant potential of 12V with current in the range of 0.65 – 0.75A using a Hewlett Packard 6632B DC power supply. The initial and final positions of the actuator were recorded using a high speed camera (Fastec Imaging IN250). The actuator was positioned in the tank using the method described by Villanueva et al (2010). Incremental weights in steps of 0.5 gm were

used to load the actuator for blocking force calculation. The tip displacements were then calculated from the pixels in a digital image created by highly reflective points attached to the BISMAC actuator.

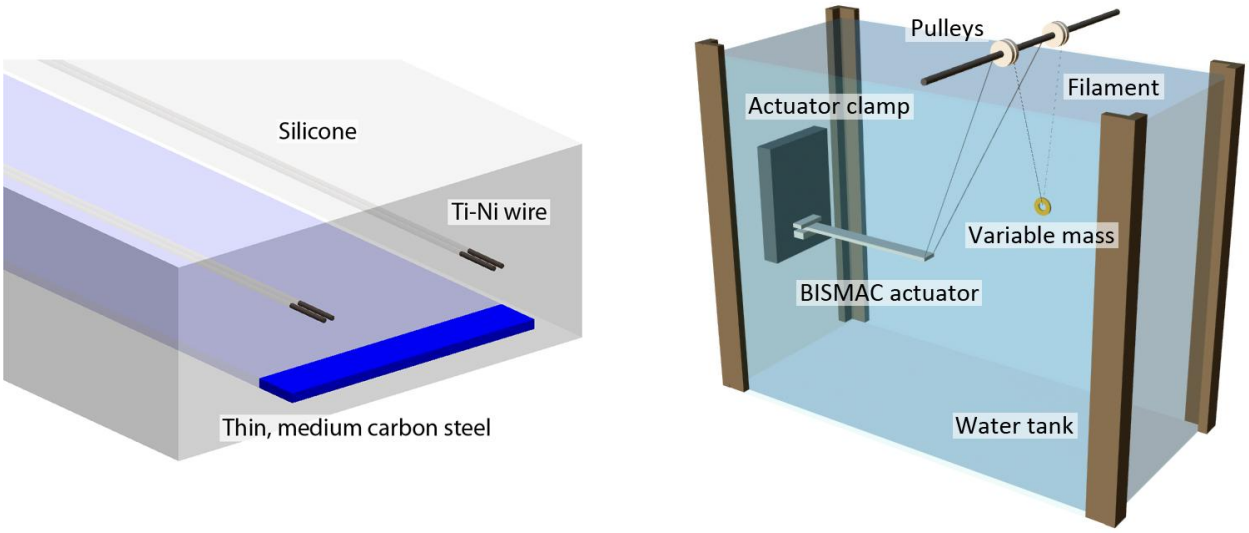

Figure 4.3: Schematic of experimental test setup to measure force and displacement characteristics.

The deformation behavior of the BISMAC actuator is shown in Figure 4.4(a) – (c). It is interesting to note that there is some upward bending in the initial position of the actuator due to elasticity of the beam in conjunction with the applied upward force from the weight over the pulleys. The time of actuation was found to increase from 0.5 s at 0.5 gm to 4 s at 6 gm. A full contraction was taken to be at the point where the actuator displacement no longer increased. A third-order polynomial regression was fitted to the force and displacement data to derive a simple mathematical relationship between the two quantities as shown in Figure 4.4(a). Since the variable masses resided under water during testing, the buoyancy force was subtracted from the calculated dry-air weight of the masses to obtain the total resistive force applied to the actuator tip. The deflection was measured linearly from the initial relaxed tip position after loading to the final tip position after SMA contraction as shown in Figure 4.4(b) and (c). Weight applied to the actuator created an initial upward deformation in the structure; therefore, the recorded displacement corresponds to a structure with initial deformation. The maximum deflection measured was 146 mm under no load, which normalizes to 111% of the active actuator length. The maximum blocking force was calculated to be 0.061 N.

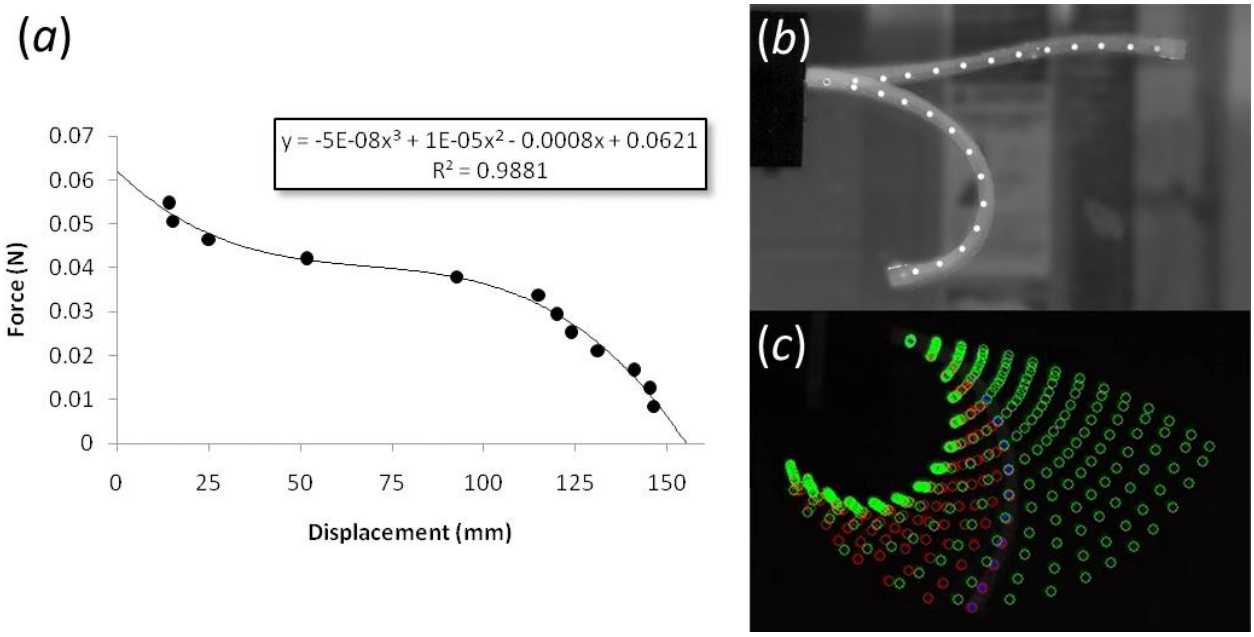

Figure 4.4: (a) Tip force and displacement properties of BISMAC actuator. Force was calculated from the magnitude of hanging mass reduced by the associated buoyancy force of the object. (b) Superimposed initial (straight) and final (deflected) states of BISMAC actuator opposing a mass of 3.5 gm, showing complex deformation profile with large overall bending deflection. (c) Motion tracking of contraction in MATLAB.

Figure 4.5 explains the understanding achieved through this series of experiments on the working mechanism of BISMAC actuators. Figure 4.5(a) shows how moment in the BISMAC is generated and Figure 4.5(b) shows the geometry of deformed BISMAC. We can define the moment in the BISMAC as:

$$M = f \times d \tag{1}$$

where f is the force generated by the SMA wire and d is the distance between SMA wire and the metal strip. If SMA wires were allowed to contract freely without constraint, they generate no force and contract by ϵ_{trans} upon heating beyond austenite transformation temperature (A_f). The physical constraint imposed by the spring steel strip reduces the achievable contraction strain. The true strain can be written as: $\epsilon_{act} = \epsilon_{trans} - \epsilon_f$ which would generate force $f = \epsilon_f E_{Austenite} A_{SMA}$, considering all strains in their absolute sense and disregarding the sign. Here ϵ_f is the strain induced by resistance to free thermal contraction of SMA, $E_{Austenite}$ is elastic modulus of austenite phase, and A_{SMA} is cross-sectional area of SMA wires.

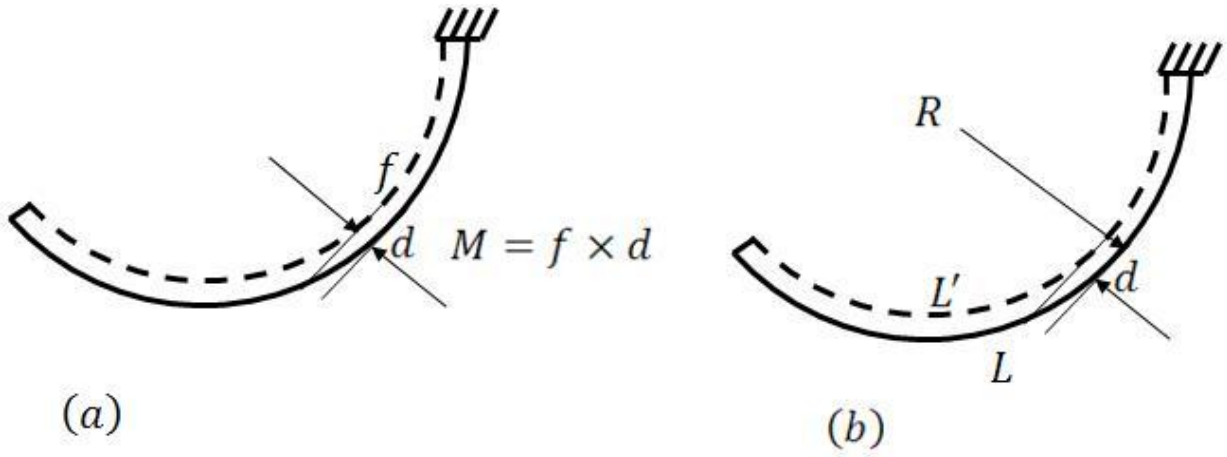

Figure 4.5: (a) Schematic of the force and moment in BISMAC, and (b) geometry of the beam curvature.

Considering that initially the length of SMA was equal to metal strip length L, the new length after contraction can be given by the relation $L' = (1 - \epsilon_{act})L$. Using the geometry shown in Figure 4.5, the radius of curvature, R, can be derived as:

$$\frac{L'}{L} = (1 - \varepsilon_{act}) = \frac{R - d}{R} \tag{2}$$

$$1 - \varepsilon_{trans} + \varepsilon_f = 1 - \frac{d}{R} \tag{3}$$

$$R = \frac{d}{\varepsilon_{trans} - \varepsilon_f} \tag{4}$$

Using (1) and (4) and by invoking Euler beam theory, we can derive strain as:

$$\frac{M}{I} = \frac{E}{R} \Rightarrow \frac{f \times d}{I} = \frac{E(\varepsilon_{trans} - \varepsilon_f)}{d} \tag{5}$$

$$\frac{\varepsilon_f E_{Austenite} A_{SMA} \times d}{I} = \frac{E(\varepsilon_{trans} - \varepsilon_f)}{d} \tag{6}$$

$$\varepsilon_f = \frac{EI(\varepsilon_{trans} - \varepsilon_f)}{E_{Austenite} A_{SMA} d^2} \Rightarrow \varepsilon_f = \frac{EI\varepsilon_{trans}}{E_{Austenite} A_{SMA} d^2 \left(1 + \frac{EI}{E_{Austenite} A_{SMA} d^2}\right)} \tag{7}$$

Other parameters being fixed, we can determine ϵ_f uniquely to be:

$$\varepsilon_f = \frac{EI\varepsilon_{trans}}{E_{Austenite}A_{SMA}d^2 + EI} \tag{8}$$

where ϵ_f provides the radius of curvature, R , that a given BISMAC configuration will achieve using (4). It should be noted that ϵ_f varies with the inverse of d^2. Thus, it is highly sensitive to d and we can purposefully achieve high curvature by reducing d. The role of silicone rubber was to maintain this distance d without adding bending stiffness so that high ϵ_f is achieved. This relationship holds true until f reaches the maximum force that SMA wire can produce; beyond this point SMA would begin to transform from austenite phase to stress-induced martensite structure and lose thermal transformation strain that was originally achieved. Though BISMAC configuration resembles bimetallic strip, it achieves much higher deformation because SMA wires have much higher force capability as they contract (Morgan and Friend 2003).

Next, a comparative analysis was conducted on the performance of BISMAC actuators with other smart material actuation technologies considered as candidates for biomimetic UUVs. For this purpose, the blocking stress and free strain of the actuators was used to create a common mathematical relationship representing the overall stress as shown in (9). Ignoring the hysteresis loop for forward and backward actuation, the relationship between blocking stress and free strain can be expressed by a linear equation with negative slope. The stress-strain relationship with assumption of linearity can be written as:

$$\boldsymbol{\sigma} = -\frac{\sigma_b}{\varepsilon_f}\boldsymbol{\varepsilon} + \sigma_b \tag{9}$$

where $\boldsymbol{\sigma}$ is the stress generated by the actuator, σ_b is the blocking stress that actuator can produce without producing any displacement, ε_f is the free strain of the actuator when no external load or constraint is applied on it, and $\boldsymbol{\varepsilon}$ is the strain at any stress generation capability of the actuator. Table 1 shows the comparison of the BISMAC actuator with other technologies. The blocking stress and strain diagram for different types of actuation technologies and BISMAC is presented in Figure 4.6 (log plot). It can be seen that BISMAC actuator provides higher strain than that can be achieved from dielectric elastomer (with typical practical strain of 63%). The energy density of BISMAC actuator was calculated to be 4,929 J/m^3 by using the active cross-section of the actuator. Active cross-section was taken to be the area exactly surrounding the spring steel and SMA wires as shown in micrographs of Figure 4.1, while any silicone outside of this area was taken to be unnecessary for functioning BISMAC and is thus extraneous.

Table 4.1: Blocking stress-strain relationship for smart actuator technologies.

Actuator Type	Blocking stress-strain equation	Comment
Shape memory alloy	$\boldsymbol{\sigma} = -4.7x10^3\ \boldsymbol{\varepsilon} + 1.9x10^2$ (a) $\boldsymbol{\sigma} = -4.5x10^3\ \boldsymbol{\varepsilon} + 1.8x10^4$ (b)	Current consumption was 180 mA at applied field of 27 V/m. Eq. (a) is for 100 µm diameter wire and Eq. (b) is for 127 µm diameter wire (Dynalloy, Inc 2010).
Dielectric elastomer	$\boldsymbol{\sigma} = -4.8\ \boldsymbol{\varepsilon} + 3x10^0$	Dielectric elastomer provide high practical strains up to 63% but the required electric field is too high of order of 110-350MV/m. A 150µm thick diaphragm requires about 190-300V (Madden et al 2004, Kornbluh et al 1998, Kornbluh et al 2000, Tadesse et al 2009).
Conducting polymer	$\boldsymbol{\sigma} = -1.7x10^3\boldsymbol{\varepsilon} + 3.4x10^1$ (a) $\boldsymbol{\sigma} = -4.2x10^1\boldsymbol{\varepsilon} + 5x10^0$ (b)	Polypyrrole actuator is promising as it requires small power <100mW. Typical strain is between 2-12% and stress is in the range of 5 - 35 MPa. Eq.(a) is for 34MPa and 2% strain, and Eq. (b) is for 5MPa and 12% strain (Madden et al 2004, Tadesse et al 2009, Tadesse et al 2008).
Pneumatic	$\boldsymbol{\sigma} = -1.9x10^0\boldsymbol{\varepsilon} + 6.5x10^{-1}$ (a) $\boldsymbol{\sigma} = -14.5x10^0\boldsymbol{\varepsilon} + 4.4x10^0$ (b)	Extended actuator length 1780 mm with contracted diameter 70 mm exhibiting force of 2500N and strain of 35% (Davis and Caldwell 2006). Braided pneumatic muscle having length of 614mm, outside diameter of 14.3mm, diameter of one strand was 25mm, number of strand was 240, length of one strand was 650mm, and spiral number was 4.7 (Davis and Caldwell 2006, Tsagarakis and Caldwell 2000). Eq. (a) is for 500 kPa and Eq. (b) is for 300 kPa. Power requirement of pneumatic actuator was usually high because it is driven by a bulky compressor which also requires electrically activated solenoid valve.
BISMAC actuator	$\boldsymbol{\sigma} = -1.9x10^0\boldsymbol{\varepsilon} + 6.5x10^{-1}$	Bio-Inspired shape memory composite (BISMAC) actuator provides bending deflection > 100% of active actuator length.
Natural Muscle	$\boldsymbol{\sigma} = -8.7x10^{-3}\ \boldsymbol{\varepsilon} + 3.5x10^{-1}$	Assuming natural muscle as a linear actuator (Madden et al 2004, Kornbluh et al 1998).

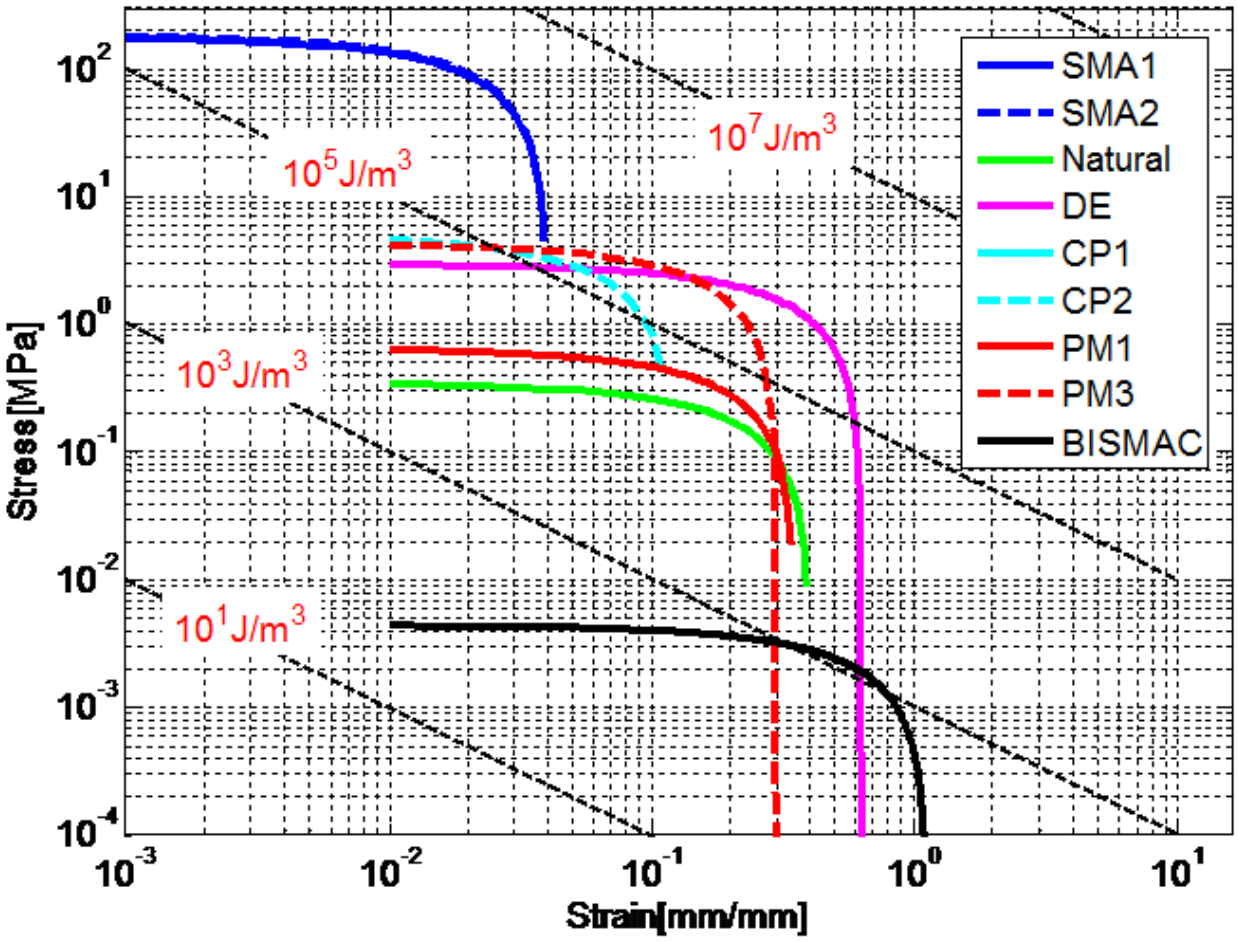

Figure 4.6: Blocking stress – strain relationship of actuator technologies conducting polymer (CP), shape memory alloy (SMA), dielectric elastomer (DE), pneumatic muscle (PM), and Bio-inspired shape memory composite actuator (BISMAC).

4.2 Joint investigation and modeling

Joints in jellyfish are approximately triangularly shaped regions where the gastrodermal lamella meets the sub- and exumbrellar epithelia (DeMont and Gosline 1988). They run from the top of the bell all the way to the bell margin. Through analytical modeling, Gladfelter determined that the joints within the bell provide strain relief and reduce the total force needed to deform the bell during contraction phase of the swimming cycle compared to an un-jointed model (Gladfelter 1972). As the bell deforms, the material inside is redistributed rather than compressed as shown in Figure 4.7, causing a shape change and thickening of the bell walls. Joints also provide a specific area where the bell can deform ensuring an even contraction radially. A modeling of joint structure geometry in conjunction with physical

implementation to experimentally test the effectiveness of joints will help in identifying the techniques that can reduce the demand on actuators.

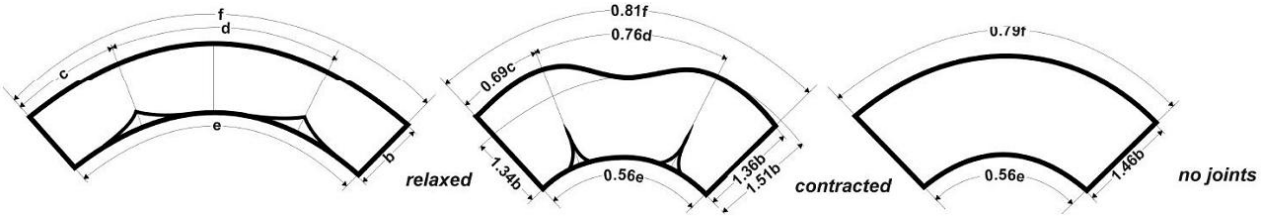

Figure 4.7: Sketch of joint structures with accompanying changes in length over a complete contraction cycle. Redrawn from Megill from Gladfelter (1972).

Physical joint structures were fabricated in 2D. The cross-sectional view of medusa bell provides the visual of intended joint geometry. A single joint rather than a full circular set was investigated for each geometry and 3D behavior was extrapolated from this model. The joint test piece was a rectangular prism of width 10 cm, height 5 cm, and average depth 1.3 cm. A solid control piece was constructed as well as eight varying geometries. A mathematical model was developed to match the geometric properties of jellyfish joint using a function of type 1/x. An empirical equation was found to describe the right hand side of the joint, given as:

$$y = \frac{1}{\alpha x + \beta} + \delta \tag{10}$$

where y describes the vertical aspects of the joint, x describes the horizontal aspects, and parameters α, β, and δ provide the translation and scaling properties. To constrain the joint geometry further, x and y intercepts were used to solve for parameters α, β, and δ as:

$$x = 0 \qquad y = y_{intercept} = j$$

$$y = 0 \qquad x = x_{intercept} = k \tag{11}$$

This yielded two additional equations that can be solved for the two parameters α and β as:

$$\beta = \frac{1}{j - \delta} \qquad \alpha = -\frac{j}{\delta k (j - \delta)} \tag{12}$$

Since α and β are both functions of δ, we will be left with single parameter which can be used to vary the joint shape while keeping the function constrained at x and y intercepts for values of k and j respectively. When α and β are inserted into Eq. (10) we obtain:

$$y = \frac{1}{\frac{-jx}{\delta k(j-\delta)} + \frac{1}{j-\delta}} + \delta \tag{13}$$

which can be reduced to

$$y = \frac{\delta j(k-x)}{\delta k - jx} \tag{14}$$

It can be seen from Eq. (14) that y is a function of horizontal position (x), the y-intercept (j), the x-intercept (k), and the parameter δ. These parameters can now be simulated to produce joints with different heights based on j, widths based on k, and curvatures based on δ. For instance, a variety of curvatures (δ) were plotted in Mathematica with height 3 cm and half-width 3 cm as shown in Figure 4.8 (the function has been mirrored about the y-axis to produce the full joint geometry from the half-geometry).

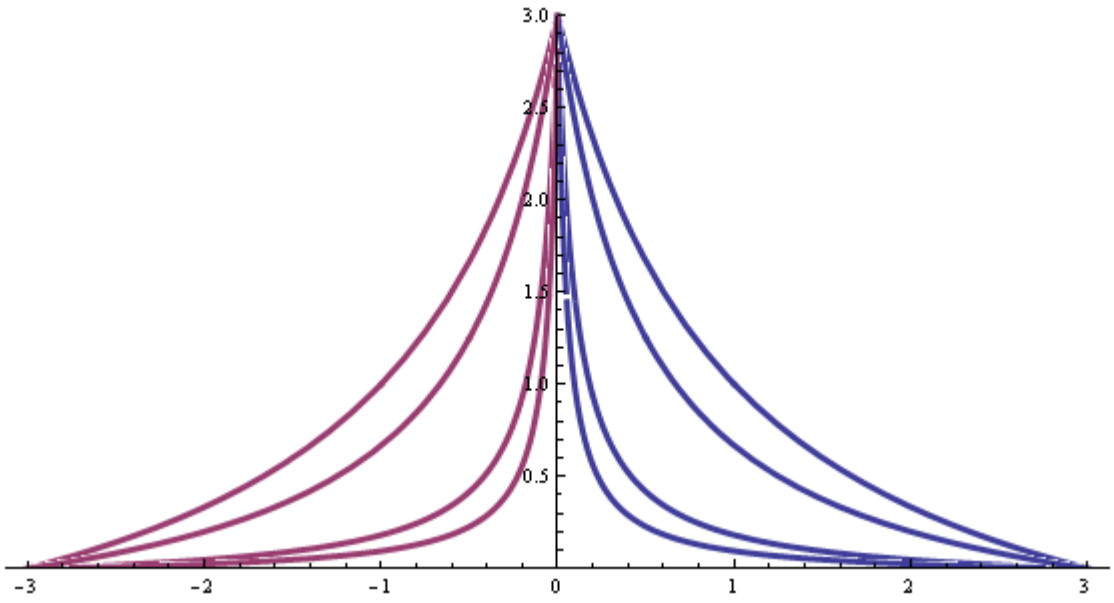

Figure 4.8: Joint geometries for curvatures of 0.01, 0.05, 0.5, and 1.0. Small curvatures produce "narrow" joints, while large curvatures produce "wide" joints.

These joint geometries were included in the form of molds used to produce test pieces. MDF board of thickness 2 cm was cut to the correct geometry which served as the base of a mold. Masking tape was wrapped around this piece to provide a wall structure to cast the test piece material. Ecoflex silicone was then poured into the molds and allowed to cure for 4 hrs before being used as shown in Figure 4.9. The joint test piece was a rectangular prism of width 10 cm, height 5 cm, and thickness 13.19 mm (SD 0.54).

Figure 4.9: Test specimens after pouring super-soft silicone

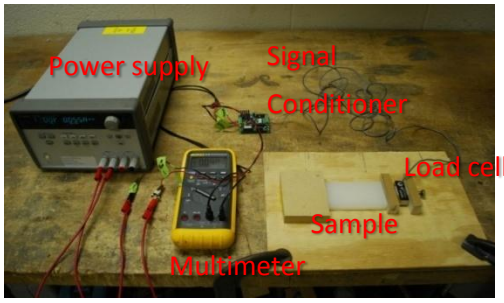

Figure 4.10: Schematic of the test setup for measuring the required force during contraction

The test setup used for force measurement is shown in Figure 4.10. A flat board was coated with a thin plastic layer to reduce friction between the test specimen and the substrate. The left side of specimen was held fixed while the right boundary which contained a load cell was allowed to slide horizontally. Joint samples were contracted and the force required was measured at 1-5 cm displacements in increments of 1 cm. A Transducer Techniques MLP-75 load cell was used in conjunction with a TMO-1 load cell signal conditioner and Agilent E3648A 0-20 VDC power supply. The power supply provided a constant 12 VDC to the signal conditioning board. Output voltage was measured with a FLUKE 87 III True RMS multimeter set to record DC voltage. Typical readings were between -50 mV and 150 mV.

During testing, artificial joints showed similarity to natural jellyfish joints as the bell wall thickened due to relocation of mesoglea material as shown in Figure 4.11. The joint structure directed contraction to occur mainly in the bell wall area. Required force was recorded for positions of 1-5 cm at 1 cm intervals, however, special attention was paid to contraction force required at 42%. This radial strain has been reported as typical for the species *Aurelia aurita* (Villanueva et al 2010). The different test pieces measured are shown in Figure 4.12. Joint geometries 2, 3, and 7 showed the lowest required contraction force at approximately 6-7 N. When varying height, the force required for contraction followed a decreasing pattern as height increased. Increasing the width of the joint also decreased the contraction force required. Lowering the value of curvature (flatter sides) decreased necessary contraction force, however, above curvature values of 1, the force leveled off and there was little advantage to further increasing the curvature. For example, it can be noted that from C=1 to C=4, there is only a 5% decrease in required force. From these data, we can summarize that an optimal joint for this configuration is 3 cm high, 3 cm wide (half-width value), and is described by a curvature value of C= 4.

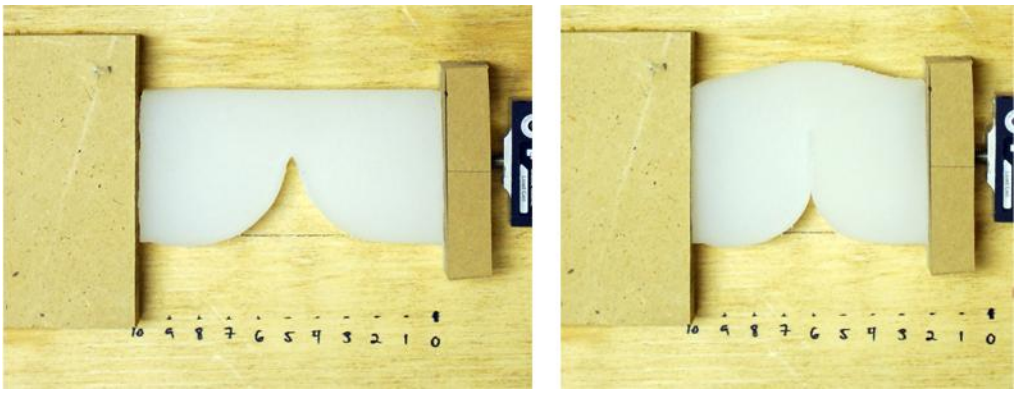

Figure 4.11: Joint test piece in the relaxed state and under compression.

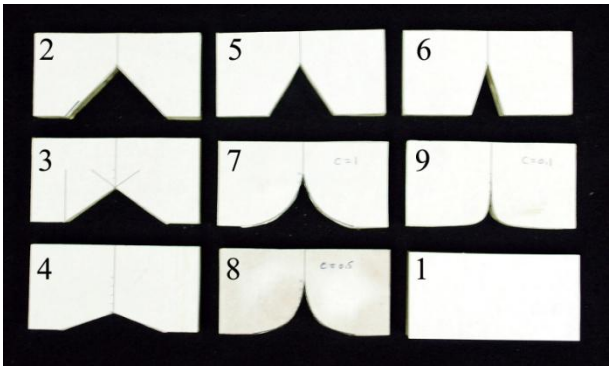

Figure 4.12: Control test piece (1) and eight different joint geometries first modeled in Mathematica and then experimentally verified.

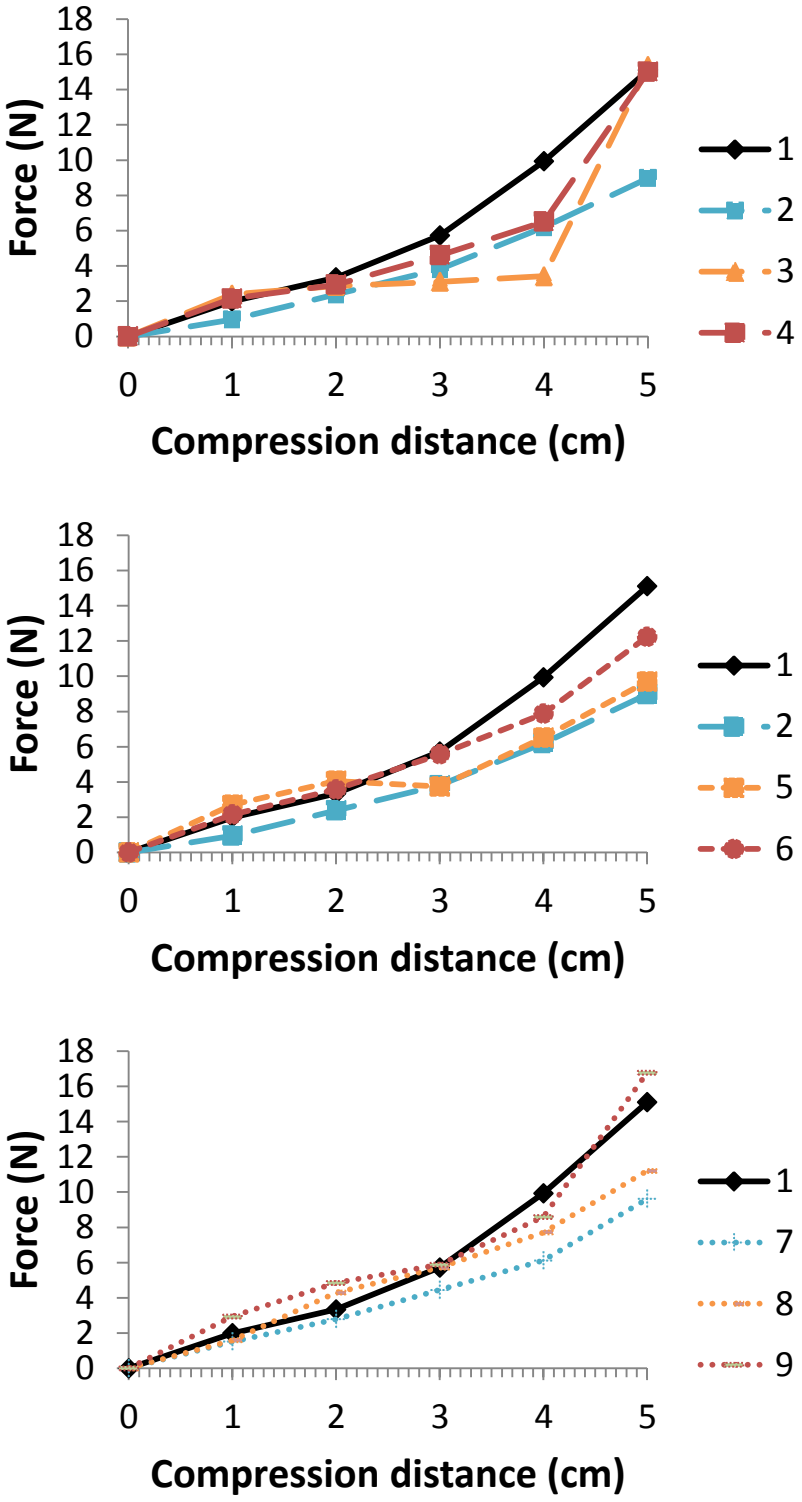

Figure 4.13: Force required for compression of a certain distance (1-5 cm in increments of 1 cm). Comparisons of joint height (a), width (b), and curvature (c). Test specimen 1 is the control piece with no joint structure. The numbers in this figure correspond to the samples shown in Figure 4.12.

4.3 Robotic jellyfish manufacturing

4.3.1 Fabrication of robotic jellyfish

The manufacturing process that leads to the creation of a prototype is a multistep venture. The BISMAC concept was leveraged and eight of these actuators were radially arranged around a laser-cut plastic central mount. First a model must be built from known *Aurelia aurita* data. From this 3D CAD model, a mold can be constructed in which the soft-bodied prototype can be built. Next, the internal structure of BISMAC actuators is constructed separate from the rest of the body. This internal structure is incorporated into the hard mold, and the soft mesoglea material is poured around it to form the correct body geometry. Lastly, the prototype is finalized by ensuring total water sealing around the vehicle.

4.3.2 3D CAD model

The 3D CAD model is constructed in SolidWorks software to allow for easy export to a rapid prototyping machine. The solid geometry can be fully defined by four rules, all derived directly from the biological model. First, longitudinal cross-section data is digitized from images of real *Aurelia aurita* (Figure 4.14a). This geometry was swept around the Z-axis to create a sold body that contained the exact geometric shape of the *A. aurita* bell (Figure 4.14c). This used the assumption that the uncontracted bell of the jellyfish forms a perfect circle at its margin. Next, joint geometry was drawn, using available literature as a guide [Gladfelter, 72]. The curve that represented the joint geometry is inscribed into the center of the bell and the placement can be seen in (Figure 4.14b). Finally, all of the joints must meet at a single point on the interior of the bell.

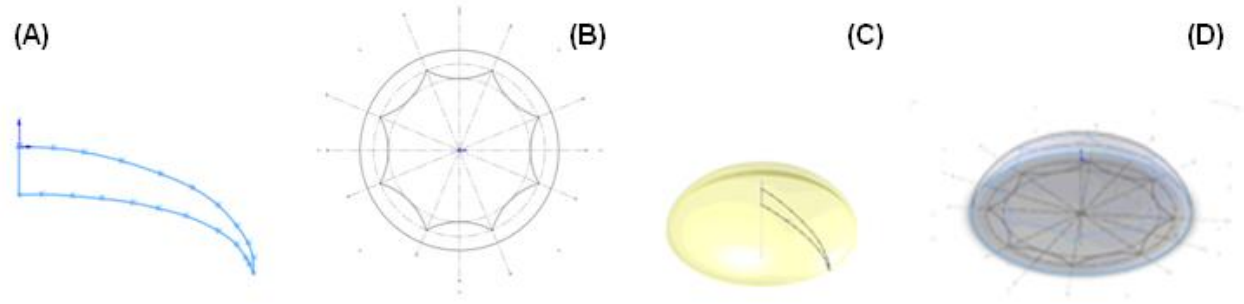

Figure 4.14: Four constraints that produce the 3D model of the *A. aurita* jellyfish.

These rules produce a solid with biomimetic geometry, as can be seen in different views in Figure 4.15. The outside surface is thus a function of the cross-section data, and the inside is a function of the cross-section as well as the joint geometry. Since the CAD model comes directly from biological data, this means the jellyfish robot will have almost exactly the same resting morphology as a natural *Aurelia aurita*.

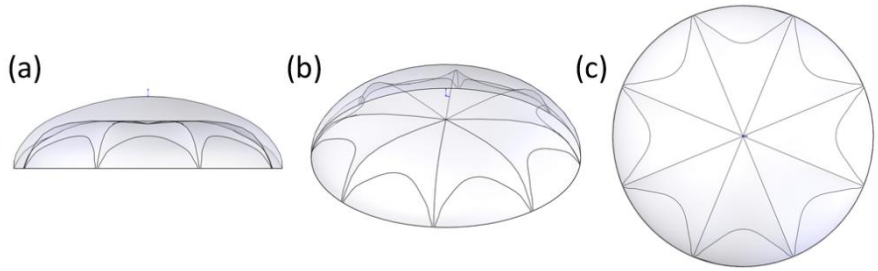

Figure 4.15: (a) Front, (b) trimetric, and (c) top view of the final jellyfish CAD model.

4.3.3 Mold production

The solid 3D CAD model is a representation of the final jellyfish and prototype form. In order to produce this shape physically, a two-part mold had to be made from the geometry. A solid block was modeled in SolidWorks and the jellyfish geometry was subtracted from the solid. The block was then divided into two segments near the bell margin of the jellyfish to produce both an exterior and an interior mold portion. Finally, extraneous material was removed to speed up mold manufacturing time. Small sections of material were removed in the model to produce internal terminations for SMA wire and spring steel in the internal structure. A cylindrical riser was added to the center of the interior mold part to support the internal structure at the correct height. Holes and pegs were added externally to ensure the mold was properly aligned after the mesoglea material was poured. The final two-part mold can be seen in Figure 4.16.

Figure 4.16: Two-part mold showing the halves separated as well as fit together.

The mold was rapid prototyped on a 3D printer (Dimension, Stratasys Corp.) which produces parts in ABS plastic. The completed mold parts were lightly sanded to reduce surface roughness and sprayed with a clear acrylic aerosol to further smooth and seal the slightly porous ABS matrix.

4.3.4 Internal BISMAC structure

The internal structure provides the actuation potential for the prototype; all active materials are contained within this assembly. The internal structure is based on the BISMAC actuator. Eight of these actuators are radially arranged with equal spacing and are held together by a hard, circular, polymer structure in the center of the bell (Figure 4.17).

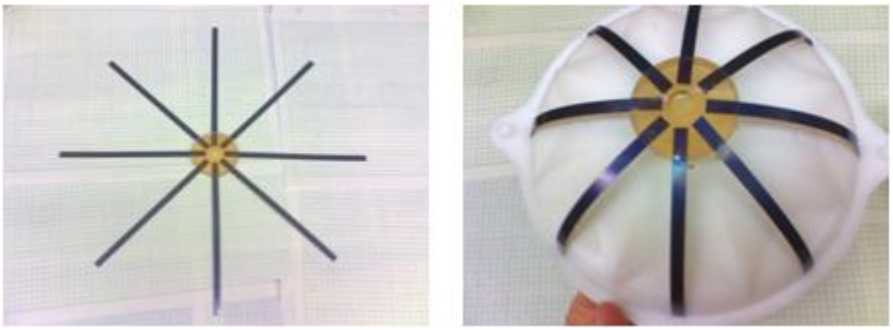

Figure 4.17: Internal structure is composed of eight radially arranged BISMACs.

To construct the internal structure, first three pieces were produced from acrylic polymer of varying thicknesses. The first is a circular piece with a diameter of 44 mm and thickness of 2 mm (piece A). The second is a ring with outer diameter of 50 mm, inner diameter of 44 mm, thickness of 6 mm and 16 radially spaced grooves in pairs of two for the SMAs to pass through (piece B). The third is a rind with outer diameter of 50 mm, inner diameter of 44 mm, and thickness of 2 mm (piece C). These pieces were laser-cut from AutoCAD 2D models on substrates of correct thickness. Schematics can be seen in the Appendix.

The SMA contractile wires were cut into lengths of 110 mm. Four lengths were used for each of the eight BISMAC segments, producing a total of 32 individual lengths. The arrangement of the four SMA lengths in each BISMAC segment was such that two lengths were connected to a positive wire and two were connected to a negative wire, with a terminus at the distal end of the BISMAC. To prepare each of these wire-to-SMA connections, 3 mm eye-crimps were used. A 4 cm section of 32 AWG insulated wire was soldered to the "eye" of the eye-crimp. This was done as the first step because the SMA contractile wire could be damaged by the high heat of the solder. After the solder was cooled, the ends of

the SMA contractile wire were inserted into the eye-crimp and the clasp was closed under pressure from a crimping tool. The exposed electrically conductive parts of the eye-crimp were then painted with black rubber or heat shrink tubing for insulation (Figure 4.18). Sixteen of these assemblies were produced, positive and negative leads, for the eight radially arranged BISMACs.

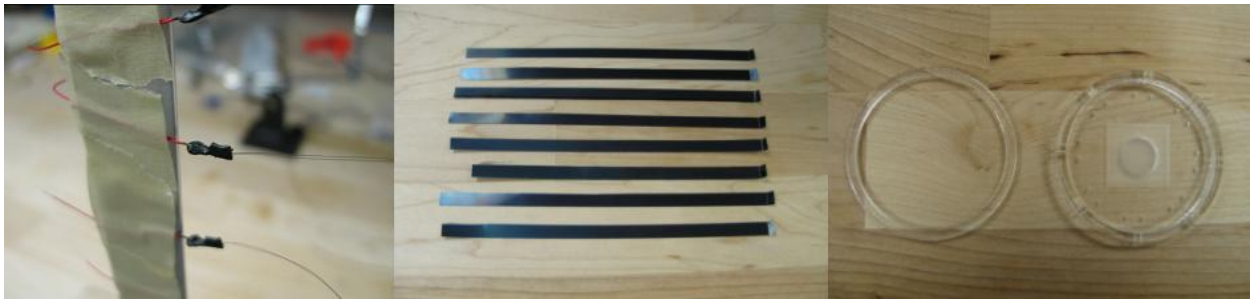

Figure 4.18: Parts for construction of internal structure. From left to right, SMA contractile wires, spring steel strips, and plastic rings.

Each of the 16 wire assemblies was then positioned within the plastic rings. Plastic piece A was placed within piece B and held stable with a thin strip of adhesive on the underside. The end of the 30 AWG wire was bent at 90 degrees to angle the wire up and perpendicularly out towards the top of the jellyfish. The SMAs were set within the grooves in plastic piece B and the wire assemblies were held in place with a small section of metal wire threaded through the holes in piece A. These wires were sacrificial and provided no electrical purpose, merely keeping the assembly stable during construction. Spring steel strips of 150 mm length, 6 mm width, and 0.1 mm thickness were radially positioned so that they lay directly on top of the pairs of SMA wires, with a 1 cm length contained within the circle, and 14 cm portion outside of the centerpiece. Plastic piece C was then laid on top and pressure was applied to the whole assembly with plastic lab clips (Figure 4.19). Acrylic resin was then poured into the center of the plastic assembly to set and hold all of the components in their respective positions. The resin also provided an electrically insulative material to mitigate the chance of an internal electrical short.

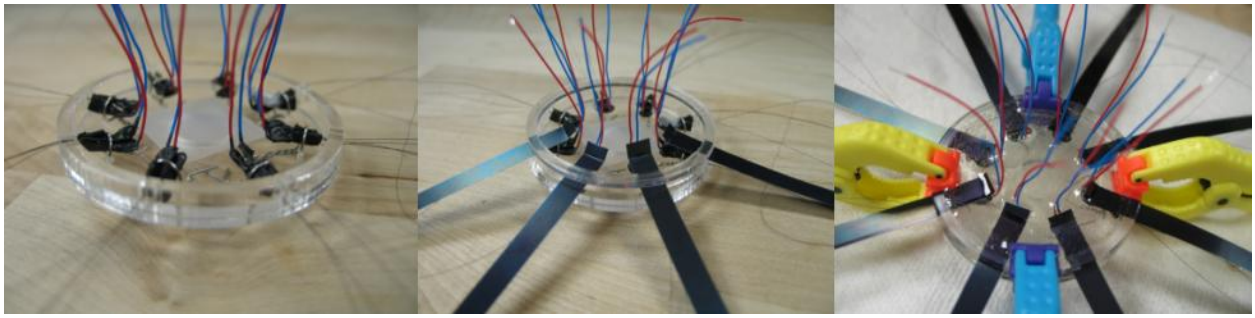

Figure 4.19: Steps to assemble the internal structure. From left to right, positioning of SMA wires, addition of spring steel strips, and clamping of entire structure with plastic lab clips allowing for the pouring of resin.

After the resin was set, the plastic clips were removed, and each spring steel strip was threaded with three plastic spacers at 2 cm intervals from the centerpiece. The spacers are constructed from hard acrylic plastic and ensure that the SMA wires remain a constant distance from the spring steel strips instead of possibly drifting within the soft mesoglea material. These spacers ensure that the SMA stays a certain distance from the spring steel at the attachment points, however, the SMA is likely further from the spring steel between the spacers during contraction. A schematic of the plastic spacers can be seen in the Appendix. The SMA contractile wires are thread through the two small holes in each of the spacers with two of the four wires going on each side (Figure 4.20).

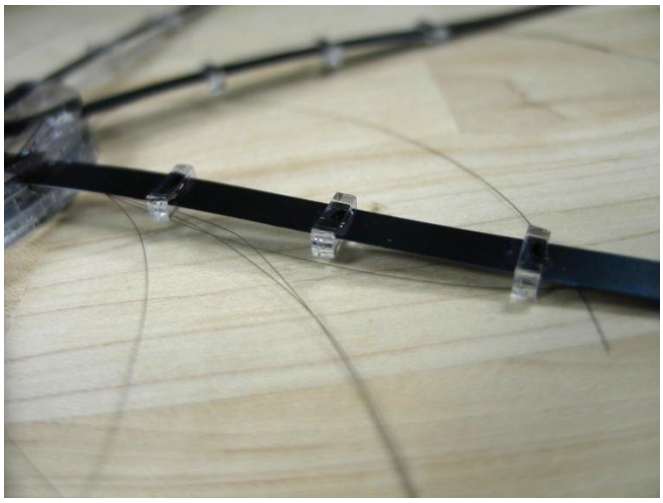

Figure 4.20: SMA contractile wires being thread through small holes in plastic spacers along the spring steel strips.

4.3.5 Integration of internal structure into mold

After the internal structure has been fabricated, the BISMAC subassembly is positioned in the mold. It is kept centered relative to the mold with a removable center post which is attached to the top of the interior half of the two part mold. The free ends of the SMA wire are fed through small holes on the interior mold that are constructed to match the holes in the plastic spacers. The ends of the spring steel strips are similarly fed through slots modeled into the mold specifically to accept them.

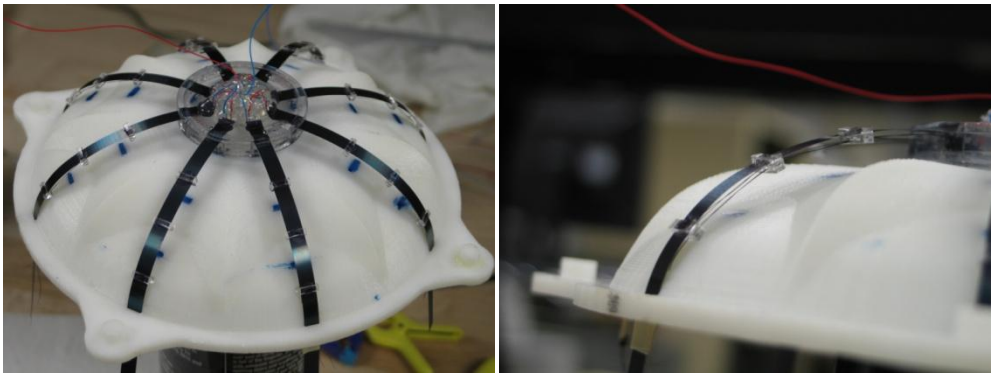

Figure 4.21: Top view of the internal structure when it is meshed with the mold as well as side view showing the SMA wire residing underneath the spring steel strips and passing through the edge of the internal mold.

The ends of the spring steel and SMA wire are held in place with small metal clamps to ensure that the internal structure remains in the correct position during the molding process. Integration of the internal structure into the mold can be seen in Figure 4.21.

4.3.6 Pouring of the mold

Two-part, platinum cure, RTV silicone (SmoothOn Corp.) is mixed with a 50:50 volume ratio in an external container. The liquid mixture is then poured into the external half of the mold. The power wires rising from the top of the internal structure are thread through the hole in the top of the external mold half as the two mold pieces are fit into each other. This will cause any excess liquid silicone to be pushed out of the mold and make certain that there are no air gaps that would cause incomplete molding.

Silicone pot life is 45 minutes, at which point the mold can be removed. A full cure is obtained in 4 hours.

4.3.7 Finalizing the prototype

After the mold is set the metal clamps on the spring steel and SMA wires are loosened. The mold halves are carefully separated and the prototype is pulled up from the surfaces. The extra ends of spring steel are cut flat with the bell margin and the final plastic SMA guide is directly added to the end of the spring steel. The free SMA wire ends are threaded through the holes in the guides and then held tight on the other side with metal crimps. This provides tension to the SMA to allow full contraction of the bell as well as completing the electrical circuit between the two parallel pairs of SMA wire bundle.

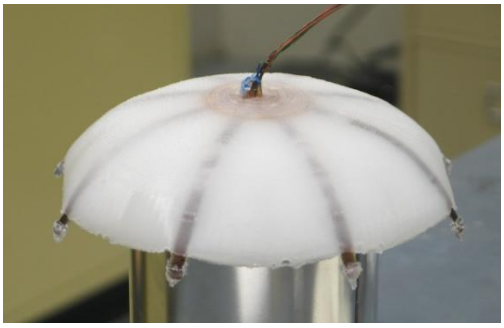

Figure 4.22: Prototype just after being released from the mold. The power wire entrance and ends of the BISMAC actuators have not yet been coated in additional silicone.

The prototype (Figure 4.22) can now be actuated; however, for use underwater all surfaces must be waterproofed with additional silicone. Silicone is added specifically to the area where the wires enter the top of the prototype and around the distal end of each BISMAC. If water were to seep in at these locations, it would cause the spring steel to rust, and negatively affect the SMA contractile wire.

4.4 Analysis of robotic jellyfish

Once the robotic prototype was complete and sealed, the various properties were characterized to compare to natural jellyfish. We had some data on the speed of *Aurelia* in the water, obtained from video recordings. The robotic jellyfish was tracked with a high speed camera (Fastec Imaging IN250). In addition, a reflective dot was placed on the top of the vehicle in a location that did not move. This reflective dot was picked up by the high speed camera in the video recording. MATLAB was used to

extract the position of that reflective dot. These results were then filtered in MATLAB with a low pass filter to remove noise from the image detection algorithm. Velocity and acceleration were calculated from the position data by taking the derivative. The speed was found to be about 2 mm/s over seven cycles and the maximum instantaneous forward velocity was about 22 mm/s. The maximum acceleration eclipsed 200 mm/s/s.

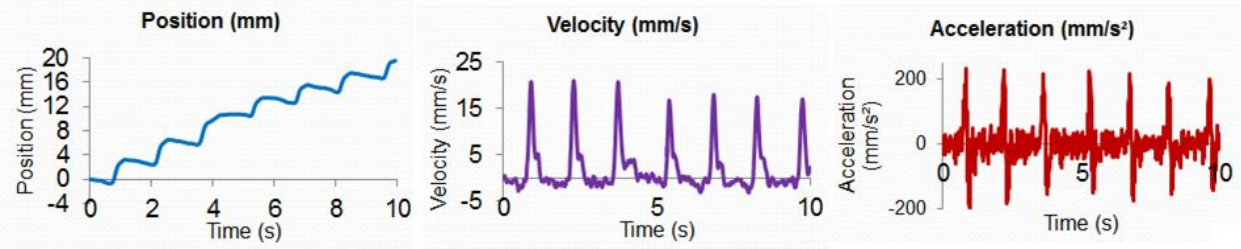

Figure 4.23: Position, velocity, and acceleration of the entire jellyfish body

A technique called digital particle image velocimetry (DPIV) was conducted to visualize the wake structure in the water. This technique can be used for both living jellyfish as well as the robotic model. This will make comparisons of the wake structure all the more easy. Figure 4.24 shows the setup to obtain DPIV results. A water tank is first seeded with millions of micron-scale glass beads. Second, a high power laser is pointed towards the tank. The laser beam runs through specialized optics to create a 2D laser sheet. This sheet illuminates a single plane in the water and lights up the small glass beads. A high speed camera is positioned at 90 degrees to the laser sheet. When the animal or robot actuates within the water, the water and glass beads move, the results of which are captured by the camera images. Software then converts this data into usable velocity vectors.

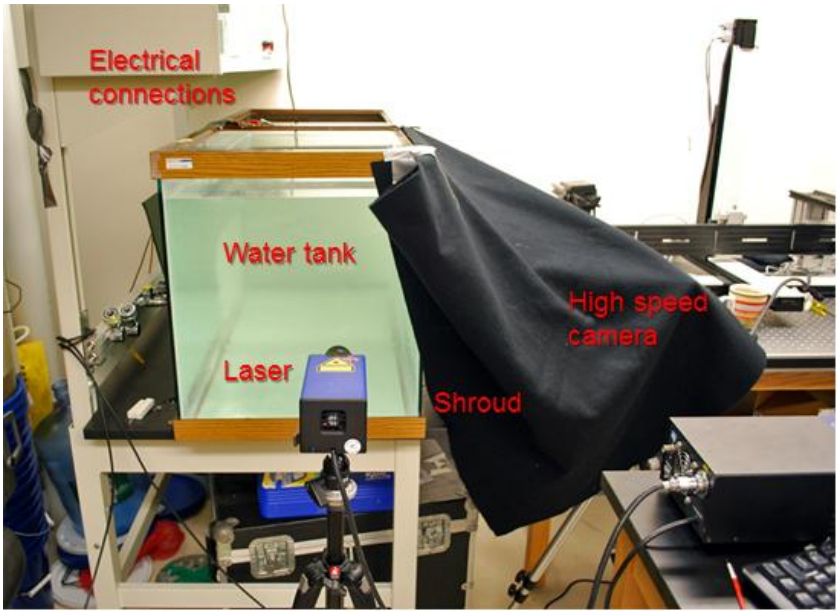

Figure 4.24: DPIV setup in Woods Hole, MA

The DPIV results are shown for the first robotic prototype. The vorticity is very weak compared to the motion of the water in the tank. This is due to the fact that there is no passive flap on the outside of the bell. Further improvements were made to the prototype to increase vortex creation, but they are outside the scope of this chapter.

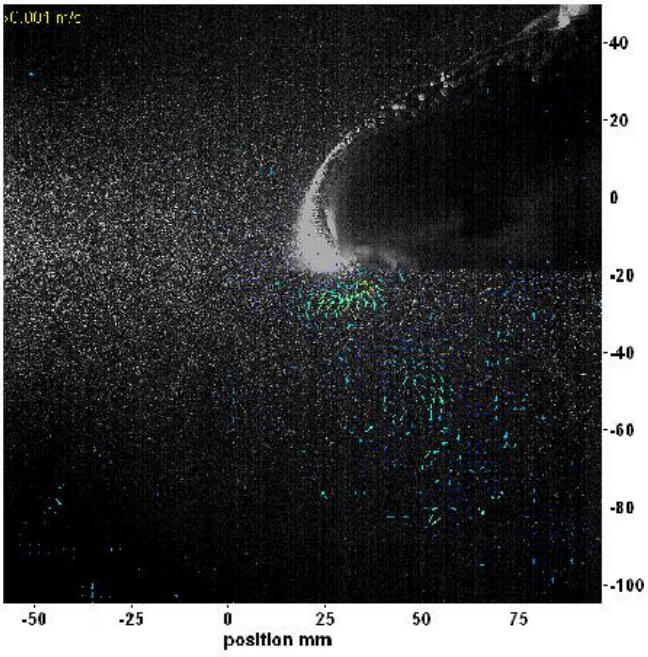

Figure 4.25: DPIV results of the wake structure of the initial prototype

A rapid heating controller was used to actuate the robotic jellyfish's segments. The controller sent a high impulse of current for the initial contraction. Once the actuators were fully contracted, a low current maintained this deformation. SMA resistance was monitored and used to determine the contraction state of the wire. The vehicle previously showed that it was able to generate enough thrust in static water conditions to propel itself and achieve a proficiency of 0.19 s^{-1} while the *A. aurita* achieves around 0.25 s^{-1}. However, this movement was only in the upward direction. A circuit was then designed to break up the large input signal (Figure 4.26(b)) for all eight BISMAC into individual signals so that different parts of the bell could be controlled independently.

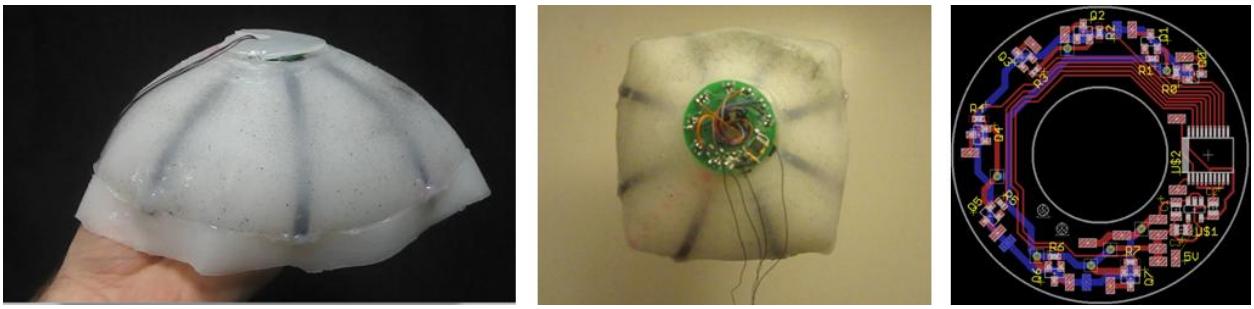

Figure 4.26: (a) Prototype just after being released from the mold. The power wire entrance has not yet been coated in additional silicone. (b) Integration of the board with the robotic jellyfish vehicle (c) Circuit diagram of the power splitting board with U$1: 5V power supply, U$2: I^2C I/O expander, Q0-Q7: MOSFET chips.

Figure 4.26 (c) shows the circuit diagram for the turning signal board as well as the integration of the electronics with the robotic jellyfish prototype. The board was designed in a circular shape to match the natural shape of the jellyfish vehicle. The motion of the actuators was not restricted because the upper portion where the electronics was held has been shown to not move during contraction. A hole in the center of the circuit board allows wires to pass through for software control and power. When a signal is sent to the board, an I^2C I/O expander chip decodes the commands and parses the signal into eight different individual on/off switches. The switches are electrically controlled by 8 MOSFETs with associated resistors and capacitors. There is also an on-board 5V supply, so that a variety of voltages can be fed into the board. This allows the electronics to use the power feed wires intended for vehicle actuation without adding added bulk to the wire bundle.

The turning of the vehicle was also analyzed in three conditions. This was accomplished by actuating only one side of the vehicle's bell and keeping the other side stationary. The first condition is a previously stationary vehicle that sits in the water column due to its neutral buoyancy. The second condition is that the vehicle is moving forwards (normally upwards in the water column). The final

condition we could see if there were unexpected changed in buoyancy or some outside force acted upon the vehicle. This condition is where the vehicle is sinking in the water column. The first two conditions showed the same response which was the vehicle turned away from the side that actuated. The last condition showed the opposite response which was that the vehicle turned towards the actuating side.

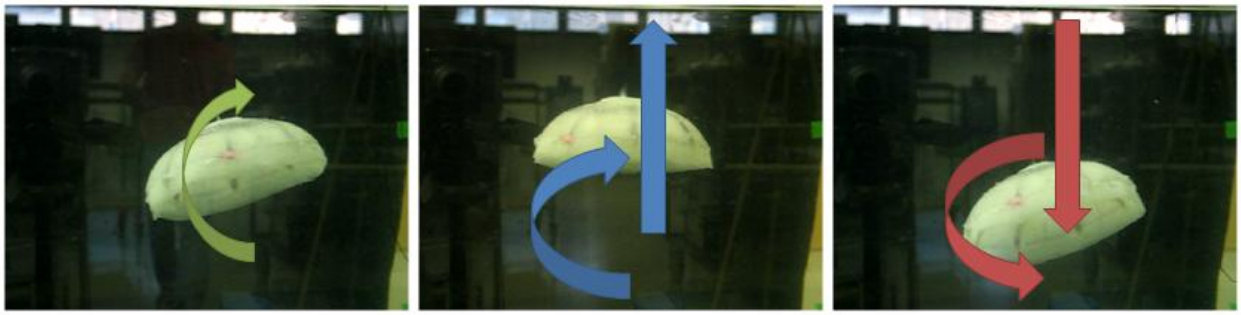

Figure 4.27: Three different turning rules depending on vehicle motion

4.5 Summary

In summary, a BISMAC actuator was characterized for tip force and displacement. A series of experiments were conducted to identify its working mechanism. The BISMAC exhibited 111% deflection with respect to the active actuator length and a blocking force of 0.061 N. The working principle of BISMAC was found to be related to a moment induced from tip attachment of the shape memory alloy rather than friction within the composite structure. Beam theory developed for BISMAC actuators reveals that this structure is highly sensitive to the distance between SMA wire and incompressible component. While SMA can be limited by either stress or strain, the limiting factor in BISMAC actuators is dependent on this separation distance. The limiting factor for the BISMACs created for duplication of medusa motion (higher number of SMA wires) was experimentally found to be strain and not force production. The actuator was compared to a variety of other smart material composite actuators and it was found that BISMAC actuator produced the greatest tip deflection among the leading smart material technologies, while providing deflections that compare well to that of natural muscular systems.

Analytical modeling in conjunction with experimental verification was used to optimize the joint dimensions. Using the materials selected in this study and optimized joint structure, the required force and energy needed to contract the bell in an artificial jellyfish UUV can be significantly reduced. It was found

through experimental testing that the artificial jellyfish joint acts to relocate material rather than compress it which is in agreement with the literature. The joint structure was also proven to reduce required contraction force as it has been proposed for the biological model. From the data shown in this study, the optimal joint configuration was found to be 3 cm high, 3 cm wide (half-width value), and described by a curvature value of C= 4. This shows that the joint structure requiring the least compressive force is relatively tall, wide, and exhibits relatively straighter sides with less curvature. To obtain a 42% contraction, typical for jellyfish species *Aurelia aurita*, the minimum required contraction force across all joint geometries was measured to be 6 N.

Chapter 5:
Conclusions and summary of bioinspired progress

In this thesis I provided analysis on the design of an underwater vehicle mimicking the propulsion mechanism and physical appearance of medusa (jellyfish). The robotic jellyfish design, morphology, and kinematics were based on the *Aurelia aurita* species. A systematic fabrication technique was developed to replicate the essential structural features of *Aurelia aurita*. The robot's body was fabricated from RTV silicone having a total mass of 242 g and bell diameter of 164 mm. The vehicle was able to generate enough thrust in static water conditions to propel itself and achieve a proficiency of 0.19 s^{-1}. The vehicle consumes an average power of 14.86 W in steady state operations.

The robotic jellyfish actuates by using bio-inspired shape memory alloy composite (BISMAC) actuators. BISMACs utilize an actuation mechanism found in the propulsion mechanism of *Cyanea capillata*. A constant cross-section BISMAC actuator was characterized in terms of bending deflection and force in conjunction with microscopy to understand its deformation mechanism. The actuator showed bending deflection of 111% with respect to the active length along with blocking force of 0.061 N. The resulting energy density of the composite actuator was 4,929 J/m^3 at the input voltage and current level of 12 V and 0.7 A, respectively. For a dry-state actuator, this performance is extremely high and represents an optimum combination of force and displacement. Experiments reveal that BISMAC's performance is related to moment induced from tip attachment of the shape memory alloy (SMA) rather than friction within the composite structure. A physics-based model of BISMAC structure is presented which shows that the actuator is highly sensitive to the distance between SMA wire and incompressible component. While SMA has both stress and strain limitations, the limiting factor in BISMAC actuators is dependent on separation distance. The limiting factor in BISMAC's suitability for mimicking the performance of medusa was experimentally found to be related to the maximum 4% strain of SMA and not its force generation.

The sub-umbrella structural and actuation features of jellyfish, artificial bell designs were created mimicking the meso-scale details and analogous propulsion mechanism. SMAs were selected for actuation because they are simple current-driven device providing moderate strain and large blocking

force. However, electrical power requirements were found to be quite high in the underwater conditions. It was identified that by including "joints" in the structural material forming the bell the overall power requirement can be reduced as it lowers the resistance to compression. An analytical model was developed that correlates the deformation achieved with the morphology of the joints. Experiments were conducted to characterize the effect of both joint shapes and structural materials on the motion. Results are compared with that of natural medusa gastrodermal lamella and analyzed using the theoretical model. By including the features inherently present in natural jellyfish, the propulsion efficiency was found to be increased.

Poly(vinyl) alcohol (PVA)-ferritin hydrogel was found to be a promising, novel material to be used as artificial mesoglea for biomimetic underwater unmanned vehicles (UUVs) modeled after jellyfish. The material exhibits similar stiffness modulus and water content. The biomimicry is intended to reduce power consumption, increase swimming efficiency, and better replicate the rowing kinematics of naturally occurring *Aurelia aurita* jellyfish. A nanocomposite hydrogel composed of a (PVA) matrix and ferritin nanoparticles has been shown to have increased durability over regular PVA hydrogels. The ferritin nanoparticles act like a spring, increasing materials modulus by increasing the surface area of the cross-linked polymer chains. To assess the viability of the hydrogel material for the UUV, compression and dielectric testing were conducted on both jellyfish and PVA hydrogels. Prior literature provides a wide range of stiffness for jellyfish mesoglea. In compressive testing *Aurelia aurita* mesoglea was found to have a highly nonlinear modulus on the range of 1.7 to 146 kPa. Natural *Aurelia aurita* were found to have a water content of 96.3% with a standard deviation of 0.57% compared to the 85% water content of PVA-ferritin hydrogels.

An artificial statocyst was also developed that replicated the natural inclinometer of the jellyfish. The statocyst was created using a series of resistors. A small voltage (5V) was applied across the circuit. Depending on where the artificial statolith landed, based upon vehicle angle, the sensor created a voltage divider. The output was then an analog 0-5V signal that linearly corresponded to vehicle tilt angle.

Chapter 6:

Future Scope

As with any large project there are many aspects yet to be tackled. The bulk of the work on this project went into the design, fabrication, and analysis of the robotic jellyfish vehicle. The vehicle itself needs to be updated in several ways. First of all, intricate turning maneuvers could be developed through software to pair sensor data with actuator output. These maneuvers could be correlated to biologically significant movements like feeding or predator evasion. In order to do these movements in the water, on board power and computing must be integrated. The difficulty comes in the small size of the current vehicle. Battery technology is also not yet to the point where a battery of usable size can fit on a prototype this small. Sensors from other universities, such as salinity sensors from Stanford should also be fully integrated and paired with robot motion. The artificial mesoglea that was developed can be used on a final prototype. This should greatly reduce the power needed to contract the BISMAC actuators. Finally the team is also working on a large-scale prototype that matches some of the largest jellyfish known in the world. This vehicle will give us the ability to study size differences in jellyfish, as well as provide ample room for onboard power and electronics.

The artificial mesoglea itself may have to be coated in a skin. This is also seen on the natural animal, as it has a dermal layer that houses the interior mesoglea. In addition there are two types of mesoglea, bell and joint. A two-material solution could be developed to mimic this. Also, currently our mesoglea has no structure. A more physical structure could be developed by controlling crystallinity or other parameters. Microfibrils could be incorporated to mimic more closely the natural jellyfish. The raw data for the bat Myotis was presented. The next genus to be investigated will be Rhinolophus, and then Pipistrellus. In future work, the viscoelastic properties such as time/temperature dependent material properties could be investigated. The relaxation of the skin wing membrane was also found to be interesting, but not yet explored. Testing at time scales that match that of each taxa's flight patterns would provide the most relevant results. Comparisons of the taxa's wing membrane material properties could be correlated to each genus' environment or other known biological factors.

Conductivity of the metallic surfaces of the artificial statocyst should be increased. This will reduce sensing errors when the metallic ball completes the circuit between the surface mount resistors and the base plate. To compliment this enhancement, a control system should be developed in software to know when the statolith has not contacted any surface. The code could then intelligently guess the inclination based on the last reading. The MEMS version of the statocyst will be manufactured with standard photolithography techniques. This sensor will increase sensitivity and resolution beyond that of the macro-scale prototype.

Lastly, the layer adhesion problem for the conducting polymer actuators must be solved. Actuators will have manufacturing problems if there is shrinkage of the PVDF layer during drying. One possible option is to use the other techniques described such as post-polym method. Additionally we want to attempt to use different ionic liquids and see if there is an output increase. Currently we have only tried to use tetrabutylammonium phosphate (TBAP).

References

Alexander R M. Visco-elastic properties of the mesoglea of jellyfish. J. Exp. Biol. (1964), 41, 363-369

Alici, G. and Huynh, N. N., "Predicting force output of trilayer polymer actuators," Sensors and Actuators A: Physical 132, 616-625 (2006).

Alici, G., Metz, P. and Spinks, G. "A methodology towards geometry optimization of high performance polypyrrole (PPy) actuators" Smart Mater. Struct. vol.15, pp. 243-252 (2006).

Arai M N 1997 A Functional Biology of Scyphozoa *London: Chapman & Hall*

ASTM Standard D575-91, 2010, "Standard Test Methods for Rubber Properties in Compression" ASTM International, West Conshohocken, PA, 2007, DOI: 10.1520/D0575-91R07, www.astm.org.

ASTM Standard D695-10, 2010, "Standard Test Methods for Rubber Properties in Compression" ASTM International, West Conshohocken, PA, 2007, DOI: 10.1520/D0575-91R07, www.astm.org.

Ayers J, Wilbur C and Olcott C 2000 Lamprey Robots *Proceedings of the International Symposium on Aqua Biomechanisms*

Ayers J, Witting J, McGruer N, Olcott C and Massa D 2000 Lobster Robots *Proceedings of the International Symposium on Aqua Biomechanisms*

Bar-Cohen Y (editor), Electroactive Polymer (EAP) Actuators as Artificial Muscles - Reality, Potential and Challenges (2nd edition), vol. PM136, SPIE Press, Bellingham, WA (2004).

Batchelor G K (1967) An Introduction to Fluid Dynamics *New York: Cambridge University Press.*

Bhushan B, Koch K and Jung Y C (2008) Biomimetic hierarchical structure for self-cleaning *Appl. Phys. Lett.* **93** 093101, DOI:10.1063/1.2976635

Bunget G, Seelecke S and Place T J (2008) Design and Fabrication of a Bio-Inspired Flapping Flight Micro-Air Vehicle *ASME 2008 Conference on Smart Materials, Adaptive Structures and Intelligent Systems* 647-654, DOI:10.1115/SMASIS2008-574

Chapman D M (1998) Microanatomy of the bell rim of *Aurelia aurita* (Cnidaria: Scyphozoa) Can. J. Zool. **77**: 34-46

Ching-Ping C, Hannaford B, "Measurement and modeling of McKibben pneumatic artificial muscles" Robotics and Automation, IEEE Transactions on, vol. 12, no.1, pp.90-102 (1996).

Clark R P and Smits A J 2006 *J. of Fluid Mech.* **562** 415-429

Colin S P and Costello J H (2002) Morphology, swimming performance and propulsive mode of six co-occurring hydromedusae *J. Exp. Biol.* **205** 427-437,

Constandinou T G, and Georgiou J 2008 Micro-Optoelectromechanical Tilt Sensor, Journal of Sensors Volume 2008, Article ID 782764, 1-7

Cook S (2010) New Zealand Coastal Marine Invertebrates *Christchurch: Canterbury University Press* pp 229-230

Dabiri J O, Colin S P and Costello J H (2005) Flow patterns generated by oblate medusan jellyfish: field measurements and laboratory analyses *J. Exp. Biol.* **208** 1257–1265

Dabiri J O, Colin SP, and Costello J H. Fast-swimming jellyfish exploit velar kinematics to form an optimal vortex wake. J. Exp. Biol. 209, 2025-2033 (2006).

Daniel T L (1983) Mechanics and energetics of medusan jet propulsion *Can. J. Zool.* **61** 1406 -1420

Davis S and Caldwell D G 2006 Braid effects on contractile range and friction modeling in pneumatic muscle actuators *The International Journal of robotics Research* **25** 359-369

Dawson M N (2003) Macro-morphological variation among cryptic species of the moon jellyfish, Aurelia (Cnidaria: Scyphozoa) *Marine Biology* **143** 369–379, DOI:10.1007/s00227-003-1070-3

DeMont, M. E. and Gosline, J. M. (1988). Mechanics of jet propulsion in the hydromedusan jellyfish, *Polyorchis penicillatus*. I. Mechanical properties of the locomotor structure. *J. Exp. Biol.* 134, 313-332.

Denton E J and Shaw T I 1961 The buoyancy of gelatinous marine animals *Proc. Physiol. Soc.* **161** 14–15

Ding, J., Liu, L., Spinks, G. M., Zhou, D., Wallace, G. G. and Gillespie J., "High performance conducting polymer actuators utilising a tubular geometry and helical wire interconnects," Synthetic Metals 138(3), 391-398 (2003).

Du, P., Lin, X. and Zhang, X., "A multilayer bending model for conducting polymer actuators," Sensors and Actuators A: Physical 163, 240-246 (2010).

Dynalloy Inc. www.Dynalloy.com

Espenschied K S, Chiel H J, Quinn R D and Beer R D 1993 *Adaptive Behavior* **1** 455-468

Gaihre, B., Alici, G., Spinks, G. M. and Cairney J. M., "Synthesis and performance evaluation of thin film PPy-PVDF multilayer electroactive polymer actuators," Sensors and Actuators A: Physical 165(2), 321-328 (2011).

Gladfelter W G (1972) Structure and function of the locomotory system of Polyorchis montereyensis (Cnidaria, Hydrozoa) *Helgol. Wiss. Meeresunters.* **23** 38–79

Gladfelter W G (1973) Structure and function of the locomotory system of the Scyphomedusa Cyanea capillata *Mar. Biol.* **14** 150–160

Guo S, Fukuda T and Asaka K (2003) A new type of fish-like underwater microrobot *IEEE/ASME Trans Mechatronics* 136–141

Gust D, Moore T A and Moore A L (2001) Mimicking Photosynthetic Solar Energy Transduction *Acc. Chem. Res.* **34** 40–48, DOI:10.1021/ar9801301

Hara, S., Zama, T., Takashima, W. and Kaneto, K., "Free-standing gel-like polypyrrole actuators doped with bis(perfluoroalkylsulfonyl)imide exhibiting extremely large strain," Smart Mater. Struct. 14(6), 1501-1510 (2005).

Hermansson AM, Ologsson P, Ekstedt S, Pihl M, Gatenholm P. Marine-inspired water-structured biomaterials. New York: Wiley-Blackwell; 2010. Chapter 28 from Water Properties in *Food, Health*, Pharmaceutical and Biological Systems. DOI: 10.1002/9780470958193.ch28

Hoerner, S. F. (1965) Fluid-Dynamic Drag. Brick Town, NJ: Hoerner Fluid Dynamics.

Hyon SH, Cha WI, Ikada Y. Preparation of transparent poly (vinyl alcohol) hydrogel. Polymer Bulletin. 1989;22(2):119-122.

Ikushima, K., John, S., Yokoyama, K. and Nagamitsu, S., "A practical multilayered conducting polymer actuator with scalable work output," Smart Mater. Struct. 18(9), 095022 (2009).

Jung H, Kim C J, and Kong S H 2007 An optimized MEMS-based electrolytic tilt sensor *Sensors and Actuators A* **139** 23–30

Kato N. 2000, "Control Performance in Horizontal Plane of a Fish Robot With Mechanical Pectoral Fins," IEEE J. Ocean. Eng., 25, pp. 121–129

Kato N. Swimming and Walking of an Amphibious Robot With Fin Actuators. Marine Technology Society Journal, Volume 45, Number 4, 2011 , pp. 181-197(17)

Katsuyama Y, Kurokawa T, Osada Y. Double-Network Hydrogels with Extremely High Mechanical Strength. Advanced materials (Weinheim). 2003;15(14):1155.

Kopecek J. Hydrogel biomaterials: A smart future? Biomaterials. 2007 Dec;28(34):5185-5192.

Kornbluh R, Pelrine R, Pei Q, Oh S and Joseph J 2000 Ultrahigh strain response of field-actuated elastomeric polymers *Proc. SPIE* **3987** 51–64

Kornbluh R, Perline R, Eckerle J and Joseph J 1998 Electrostrictive polymer artificial muscle *Proc. IEEE Robot. Autom.* **3** 2147–2154

Kramp P L (1959) Stephanoscyphus (Scyphozoa) *Galatea Report* **1** 173-185

Lazaris A, Arcidiacono S, Huang Y, Zhou J, Duguay F, Chretien N, Welsh E A, Soares J W and Karatzas C N (2002) Spider Silk Fibers Spun from Soluble Recombinant Silk Produced in Mammalian Cells *Science* **295** 472-476, DOI:10.1126/science.1065780

Lee H, Lee B P and Messersmith P B (2007) A reversible wet/dry adhesive inspired by mussels and geckos *Nature* **448** 338-341, DOI:10.1038/nature05968

Liu J, Dukes I and Hu H 2005 *IEEE/RSJ Int. Conf. on Intel. Rob. And Sys.* 807-812

Long, John H.; Koob, Tom; Schaefer, Justin; Summers, Adam; Bantilan, Kurt; Grotmol, Sindre; Porter, Marianne. Inspired by Sharks: A Biomimetic Skeleton for the Flapping, Propulsive Tail of an Aquatic Robot. Marine Technology Society Journal, Volume 45, Number 4, 2011 , pp. 119-129(11)

Lorraine Hsu, Christoph Weder and Stuart J. Rowan. Stimuli-responsive, mechanically-adaptive polymer nanocomposites. J. Mater. Chem., 2011, 21, 2812–2822. DOI: 10.1039/c0jm02383c

Lowndes A G, Percentage of Water in Jelly-Fish. Nature, 1942, 150, 234–235.

Madden J D, Vandesteeg N A, Anquetil P A, Madden P G, Takshi A, Pytel R Z, Lafontaine S R, Wierenga P A and Hunter I W 2004 Artificial muscle technology: physical principles and naval prospects *IEEE J. Ocean. Eng.* **29** 692- 695

Mandelkern L. The effect of molecular weight on the crytallization and melting of long-chain molecules. Journal of Polymer Science, Part C (Polymer Symposium). 1967;(18):51-55.

Manmohan Kumar, Lalit Varshney, Sanju Francis. Radiolytic formation of Ag clusters in aqueous polyvinyl alcohol solution and hydrogel matrix. Radiation Physics and Chemistry 73 (2005) 21–27. doi:10.1016/j.radphyschem.2004.06.006

McHenry M J (2007) Comparitive Biomechanics: The Jellyfish Paradox Resolved *Current Biology* **17** R632-R633, DOI:10.1016/j.cub.2007.06.027

McHenry M J and Jed J (2003) The ontogenetic scaling of hydrodynamics and swimming performance in jellyfish (Aurelia aurita) *The Journal of Experimental Biology* **206** 4125-4137, DOI:10.1242/jeb.00649

Megill WM. The Biomechanics of Jellyfish Swimming. Thesis for the Degree Doctor of Philosophy in the Department of Zoology at McGill University. 1991.

Megill, W., M., "The biomechanics of jellyfish swimming," Ph.D. Dissertation, Department of Zoology, University of British Columbia, 116 pp (2002).

Menciassi A and Dario P (2003) Bio-inspired solutions for locomotion in the gastrointestinal tract: background and perspectives *Phil. Trans. R. Soc. Lond. A* **361** 2287-2298, DOI:10.1098/rsta.2003.1255

Mirfakhrai, T.; Madden J.D. and Baughman, R. H. “Polymer Artificial Muscles”, *Mater. Today*, vol. 10 No. 4, pp.30-38 (2007).

Miyazaki T, Yamaoka K, Gong JP, Osada Y. Hydrogels with crystalline or liquid crystalline structure. Macromolecular rapid communications. 2002;23(8):447-455.

Mohseni K, “Pulsatile jets for unmanned underwater maneuvering,” Chicago, Illinois, AIAA paper 2004-6386, 20-23 September 2004, 3rd AIAA Unmanned Unlimited Technical Conference, Workshop and Exhibit.

Morgan N B and Friend C M 2003 *Shape Memory Alloys - A Smart Technology? of Smart technologies* ed K Worden et al. (New Jersey: World Scientific) pp 109-137

Ohara K, Yamashita I, Yaegashi T, Moniwa M, Yoshimaru M, Uraoka Y. Floating Gate Memory with Biomineralized Nanodots Embedded in High-k Gate Dielectric. Applied physics express. 2009;2(9):095001.

Omori M and Kitamura M (2004) Taxonomic review of three Japanese species of edible jellyfish (Scyphozoa: Rhizostomeae) *Plankton Biol. Ecol.* **51** 36–51

Park K, Shalabay WS, Park H. Biodegradable hydrogels for drug delivery. Lancaster, Pennsylvania: Technomic Publishing Company, Inc.; 1993

Peppas NA, Stauffer SR. Reinforced Uncrosslinked Poly (vinyl alcohol) Gels Produced by Cyclic Freezing-Thawing Processes: a Short Review. Journal of Controlled Release. 1991 Aug;16(3):305-310.

Satterlie R A, Thomas K S and Gray G C (2005) Muscle Organization of the Cubozoan Jellyfish Tripedalia cystophora Conant 1897 *Biol. Bull.* **209** 154-163

Seelecke, S. and Müller, I. “Shape memory alloy actuators in smart structures: Modeling and simulation” *Appl. Mech. Rev.*, vol. 57, Issue 1, pp.23-46(2004).

Seibel B A and Drazen J C (2007) The rate of metabolism in marine animals: environmental constraints, ecological demands and energetic opportunities *Phil. Trans. R. Soc. B* 362 2061-2078, DOI:10.1098/rstb.2007.2101

Seipe K. Schmid V, “Evolution of striated muscle: Jellyfish and the origin of triploblasty”, Dev. Biol. 282, 14 – 26 (2005).

Shahinpoor M and Wang G 1995 *Proc. SPIE* **2447** 291

Shin M K, Kim S I, Kim S J. Controlled magnetic nanofiber hydrogels by clustering ferritin. *Langmuir* **2008**, *24*, 12107-12111.

Shin M K, Spinks G M, Shin S R, Kim S I, and Kim S J. Nanocomposite Hydrogel with High Toughness for Bioactuators. Advanced Materials. 2009, 21, 1712–1715.

Smith C and Priya S (2010) Bio-inspired unmanned undersea vehicle Proc. SPIE 7644 76442A, DOI:10.1117/12.847761

Tadesse Y, Grange R W and Priya S 2009 Synthesis and cyclic force characterization of helical polypyrrole actuators for artificial facial muscles *Smart Mater. Struct.***18** 085008

Tadesse Y, Moore D, Thayer N and Priya S 2009 *Proc. SPIE* **7287**, 728709

Tadesse Y, Priya S, Chenthamarakshan C R, de Tacconi N R and Rajeshwar K 2008 Polypyrrole–polyvinylidene difluoride composite stripe and zigzag actuators for use in facial robotics *Smart Mater. Struct.***17** 025001

Tadesse, Y., Brennan, J., Smith, C., Long, T. E. and Priya, S.,"Synthesis and characterization of polypyrrole composite actuator for jellyfish unmanned undersea vehicle," Proc. of the SPIE 7642, 764222-764222-11 (2010).

Takehisa T. Nanocomposite hydrogels: A unique organic-inorganic network structure with extraordinary mechanical, optical, and swelling/de-swelling properties. Advanced materials (Weinheim). 2002;14(16):1120-1124.

Tang L, Zhang K, Chen S, Zhang G, and Liu G 2009 MEMS inclinometer based on a novel piezoresistor structure *Microelectronics Journal* **40** 78–82

Trask R S, Williams H R and Bond I P (2007) Self-healing polymer composites: mimicking nature to enhance performance *Bioinspir. Biomim.* **2** P1, DOI:10.1088/1748-3182/2/1/P01

Triantafyllou M S and Triantafyllou G S, "An efficient swimming machine," Scientific American, vol. 272, pp. 64–70, Mar. 1995.

Trieu H. H., Qutubuddin S. Polyvinyl alcohol hydrogels I. Microscopic structure by freeze-etching and critical point drying techniques. Colloid and Polymer Science (1994) 272: 301-309.

Tsagarakis N and Caldwell D G 2000 Improved modeling and assessment of pneumatic muscle actuators *Proc. IEEE Int. Conf. Rob. Autom.* **4** 3641-3646

Turner T L, Lach C L and Cano R J 2001 *Proc. SPIE* **4333** 343

Villanueva A A, Joshi K B, Blottman J B and Priya S (2010a) A bio-inspired shape memory alloy composite (BISMAC) actuator *Smart Mater. Struct.* **19** 025013

Villanueva A A, Joshi K B, Blottman J B and Priya S 2010 *Smart Mater. Struct.* **19** 025013

Villanueva A and Priya S (2010) BISMAC control using SMA resistance feedback *Proc. SPIE* **7642** 76421Z, DOI:10.1117/12.847788

Villanueva A, Anna C, Smith C and Priya S (2010b) Robojelly Bell Kinematics and Resistance Feedback Control *The 2010 IEEE International Conference on robotics and Biomimetics (ROBIO2010)* In press

Villanueva A, Bresser S, Chung S, Tadesse Y and Priya S (2009) Jellyfish inspired underwater unmanned vehicle *Proc. SPIE* **7287** 72871G, DOI:10.1117/12.815754

Villanueva, A., Joshi, K. B., Blottman, J. B. and Priya, S. "A bio-inspired shape memory alloy composite (BISMAC) actuator" *Smart Materials and Structures*, vol. 19, 025013 (17pp), (2010).

Wallace, Gordon G,Spinks, Geoffrey M " Conducting polymers: A bridge across the bionic interface" Chemical Engineering Progress, (2007).

Wang G and Shahinpoor M 1997 *Smart Mater. Struct.* **6** 214–221

Wang H, Brown H. Jellyfish gel and its hybrid hydrogels with high mechanical strength. Soft matter. 2011;7(1):211-219.

Wang Z, Hang G, Wang Y, Li J and Wei D (2008) Embedded SMA wire actuated biomimetic fin: a module for biomimetic underwater propulsion *Smart Mater. Struct.* **17** 025039

Whitaker J. D., King R. and Knott D., Sea Science An Information/Education Series from the Marine Resources Division South Carolina Department of Natural Resources. "Jellyfish" Columbia, South Carolina 29202

Xiaobo Tan; Kim, D.; Usher, N.; Laboy, D.; Jackson, J.; Kapetanovic, A.; Rapai, J.; Sabadus, B.; Xin Zhou. An Autonomous Robotic Fish for Mobile Sensing. Intelligent Robots and Systems, 2006 IEEE/RSJ International Conference on. 2006. page(s): 5424 - 5429. DOI: 10.1109/IROS.2006.282110

Xuezhen Wang, Huiliang Wang and Hugh R. Brown. Jellyfish gel and its hybrid hydrogels with high mechanical strength. Soft Matter, 2011, 7, 211. DOI: 10.1039/c0sm00632g

Yang X, Liu Q, Chen X, Yu F, Zhu Z. Investigation of PVA/ws-chitosan hydrogels prepared by combined [gamma]-irradiation and freeze-thawing. Carbohydrate Polymers. 2008 Aug 1;73(3):401-408.

Yang Y, Ye X and Guo S (2007) A New Type of Jellyfish-Like Microrobot *Proceeding of the 2007 IEEE Intl. Conference on Integration Technology*

Yao, Q., Alici, G. and Spinks, G. M., "Feedback control of tri-layer polymer actuators to improve their positioning ability and speed of response," Sensors and Actuators A: Physical 144(1), 176-184 (2008).

Yasrebi M, Kim G H, Gunnison K E, Milius D L, Sarikaya M and Aksay I A (1990) Biomimetic processing of ceramics and ceramic-metal composites *Better Ceramics through Chemistry IV* **180** 625–635

Yokoyama F. Morphology and structure of highly elastic poly(vinyl alcohol) hydrogel prepared by repeated freezing-and-melting. Colloid and polymer science. 1986;264(7):595-601.

Zama, T., Hara, S., Takashima, W. and Kaneto, K., "Comparison of Conducting Polymer Actuators Based on Polypyrrole Doped with BF_4^-, PF_6^-, $CF_3SO_3^-$, and ClO_4^-," Bull. Chem. Soc. Japan Vol. 78(3), 506-511 (2005).

Appendix A: Mechanical testing of natural bat membrane

The custom designed test setup is comprised of a linear actuator to drive the sample between two ABS plastic sample holders. A stationary, high precision load cell measures the output force and eliminates inertial errors. GigE cameras record the strain of the sample from both perpendicular directions – top and side. This data as well as the load cell and linear actuator position are fed through a NI-FPGA into a PC which gathers data. LabVIEW software is used to acquire the signal. Ensemble Motion Controller is used to command the linear actuator. JAI Control Tool is used to setup and record the data from the GigE cameras.

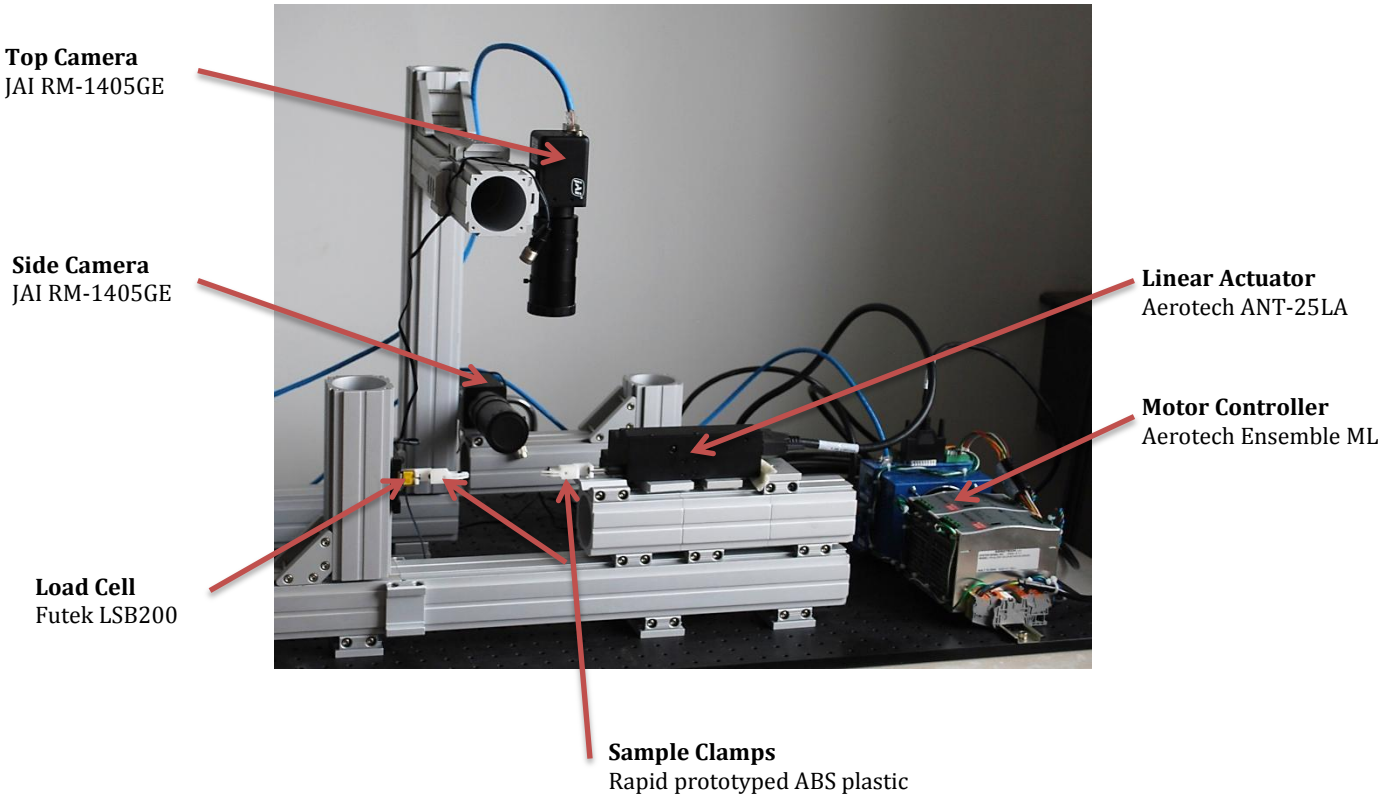

Figure 3.12: Test setup for bat wing membrane tests

3.5.1 Methods

Stress and strain are calculated from the position and force data along with the cross sectional area which is mathematically extracted from the video images through a custom MATLAB code.

Maximum Young's Modulus as well as strain at failure are reported for the four different wing regions, dactylopatagium, propatagium, plagiopatagium, and uropatagium, from the genus Myotis.

Figure 3.13: The main wing corrugations can be easily seen as lighter lines in the plagiopatagium.

Samples were also tested both in the direction perpendicular as well as parallel to the major wing corrugations to investigate wing anisotropy. These corrugations can easily been seen in the wing when it is stretched and allowed to have light shine through it as can be seen in Figure 3.13 . Each sample was first preconditioned at 10% strain for 10 cycles and then ramp loaded to 100% strain at 0.1 mm per second. All samples failed completely before the displacement limit was reached.

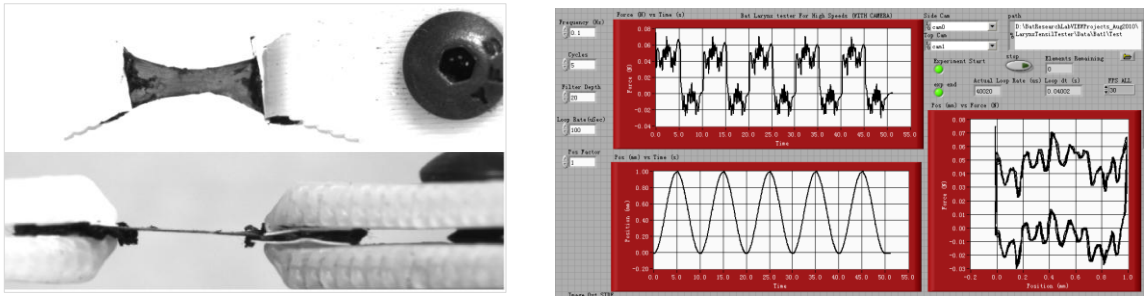

Figure 3.14: Top and side views of the wing membrane sample. Front panel of the custom-designed software recording stress and strain

3.5.2 Results

The uropatagium showed the greatest stiffness among the wing regions. This compares well to Swartz 1996, "Because the uropatagium is responsible for forcibly propelling prey, the skin must be strong enough to perform this task without failure. Some insects may also have pointed projections on their body or limb surfaces, maximizing the importance of puncture resistance in this region."

When the wing membrane is tested perpendicular to the corrugations, the modulus is much higher compared to when it is tested parallel to corrugations. Also, in general, the failure strain is maximum parallel to the corrugations. Both of these points agree with Swartz 1996.

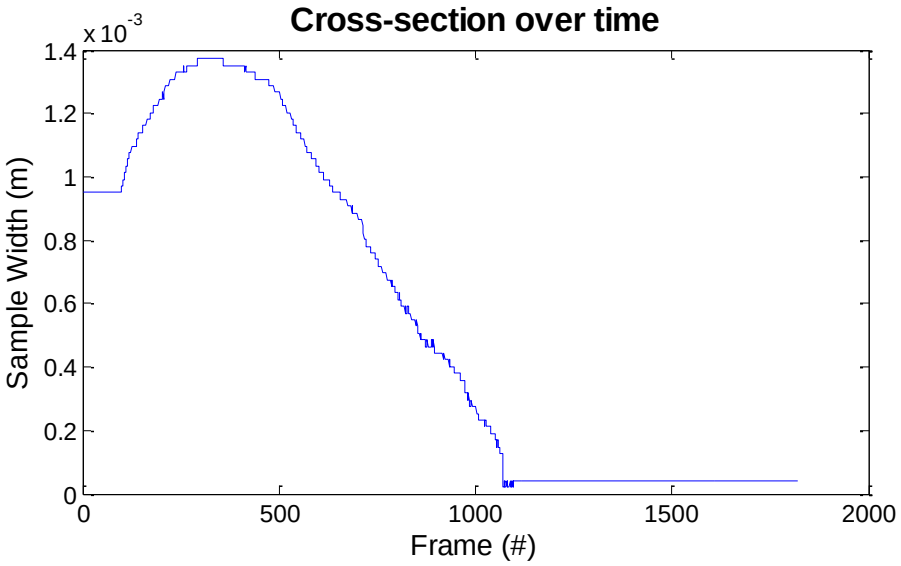

Figure 3.15: Representative plot of the cross-section of the wing membrane sample over time

Table 3.1: Young's modulus (E), Myotis wing skin membrane

Perpendicular to Corrugations		Parallel to Corrugations	
Region	*Maximum Modulus*	*Region*	*Maximum Modulus*
Dactylopatagium	45 MPa	Dactylopatagium	6.3 MPa
Propatagium	38 MPa	Propatagium	17 MPa
Plagiopatagium	21 MPa	Plagiopatagium	12 MPa
Uropatagium	60 MPa	Uropatagium	70 MPa

Table 3.2: Failure strain, Myotis wing skin membrane

Perpendicular to Corrugations		Parallel to Corrugations	
Region	*Failure Strain*	*Region*	*Failure Strain*
Dactylopatagium	0.47	Dactylopatagium	0.40-0.65
Propatagium	0.49	Propatagium	0.65
Plagiopatagium	0.39	Plagiopatagium	0.23-0.75
Uropatagium	0.47	Uropatagium	0.72

It is noted that the dactylopatagium had the greatest anisotropy in modulus compared to all of the wing regions, showing an 86% decrease in stiffness going from testing perpendicular to the major corrugations to parallel with them. The membrane of the uropatagium showed little anisotropy and it is noted that in concert with this there was very little visual evidence of corrugations in the skin material.

From this point is it surmised that the corrugations themselves have an important role in the anisotropic nature of the bat wing membrane. This point is interesting and has never been specifically proven, however more research is necessary.

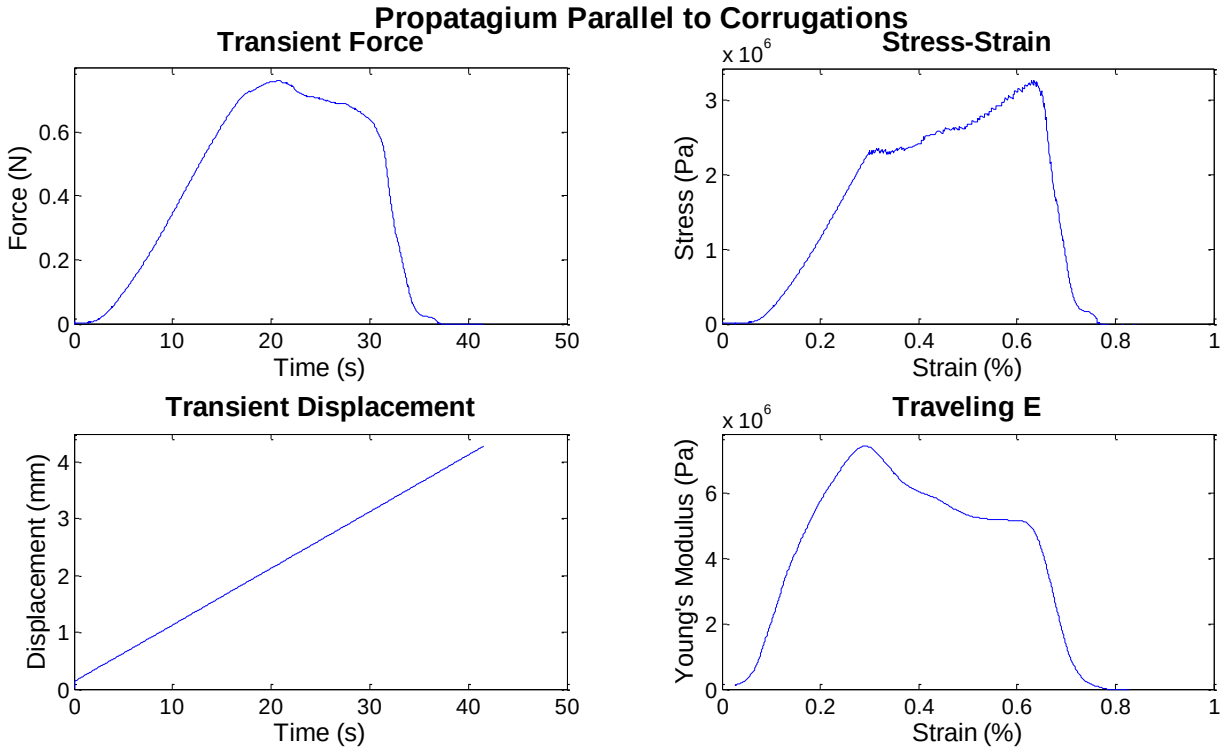

Figure 3.16: Representative data set for the propatagium with tensile force applied parallel to the main wing corrugations

The results data for Myotis is shown. We are also investigating the taxa Rhinolophus and Eptesicus. In future work, the viscoelastic properties such as time/temperature dependent material properties could be investigated. The relaxation of the skin wing membrane was also found to be interesting, but not yet explored. Testing at time scales that match that of each taxa's flight patterns

would provide the most relevant results. Comparisons of the taxa's wing membrane material properties could be correlated to each genus' environment or other known biological factors.

Figure 3.17: Myotis, Rhinolophus, and Eptesicus.

Dactylopatagium Perpendicular to Corrugations

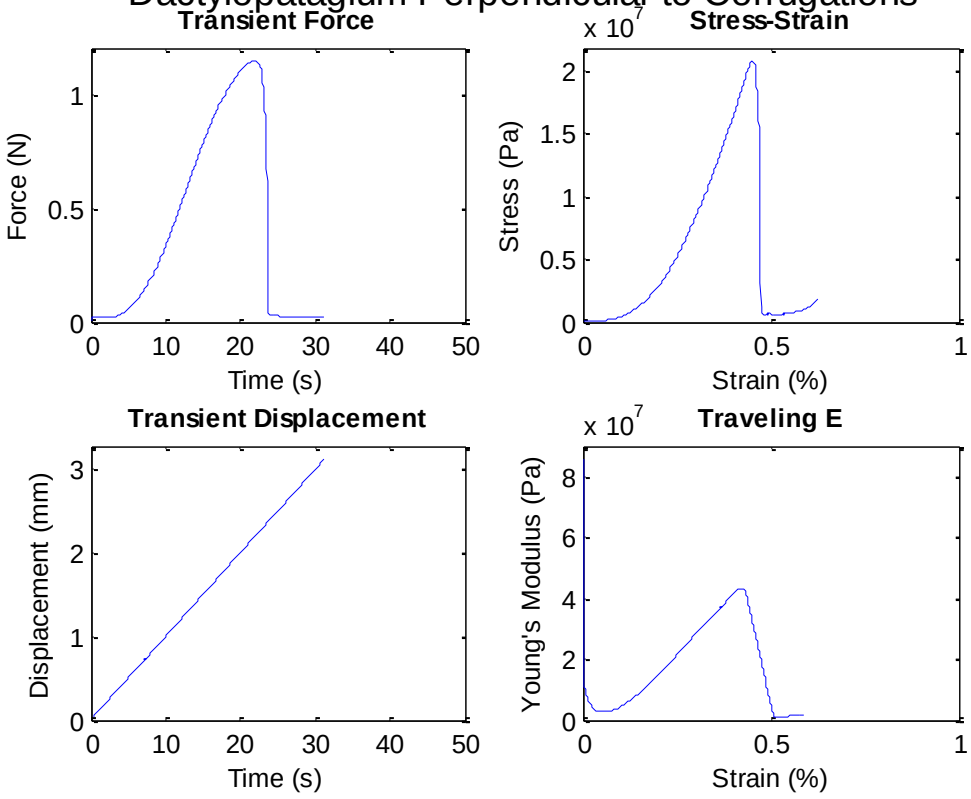

Propatagium Perpendicular to Corrugations

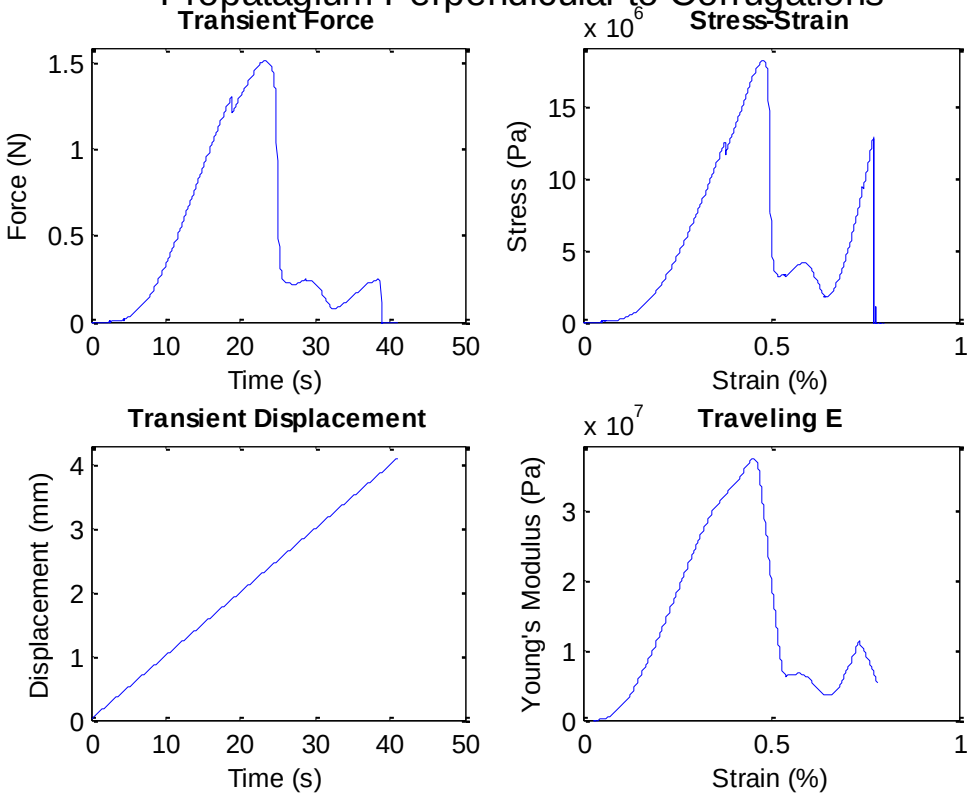

Plagiopatagium Perpendicular to Corrugations

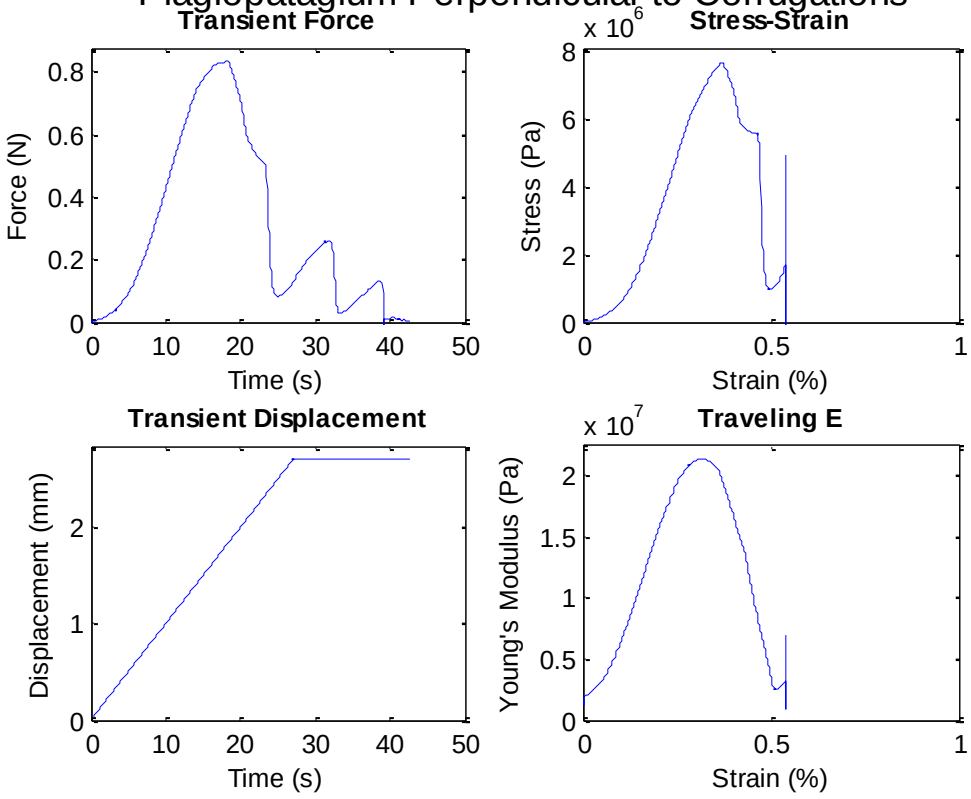

Uropatagium Perpendicular to Corrugations

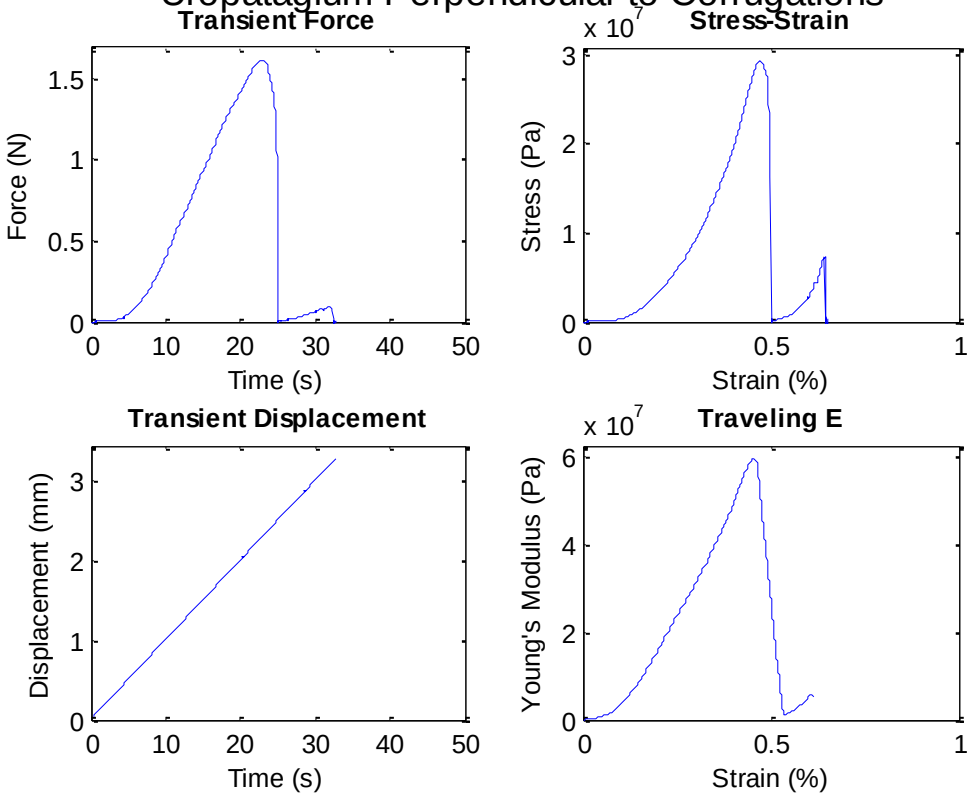

Dactylopatagium Parallel to Corrugations

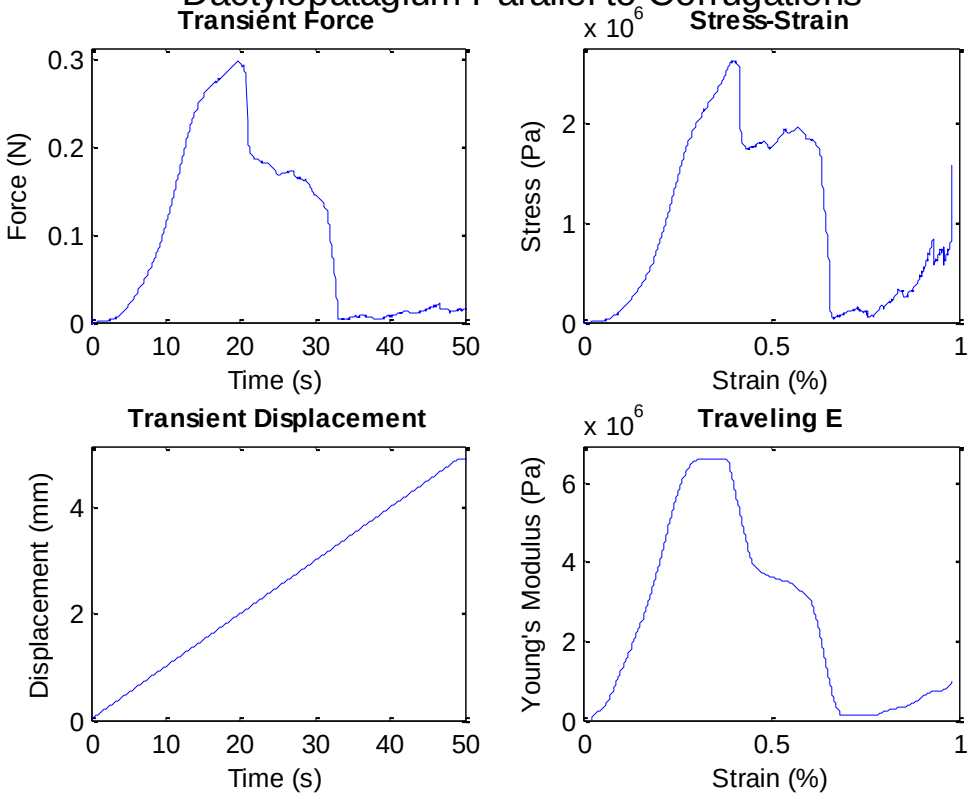

Propatagium Parallel to Corrugations

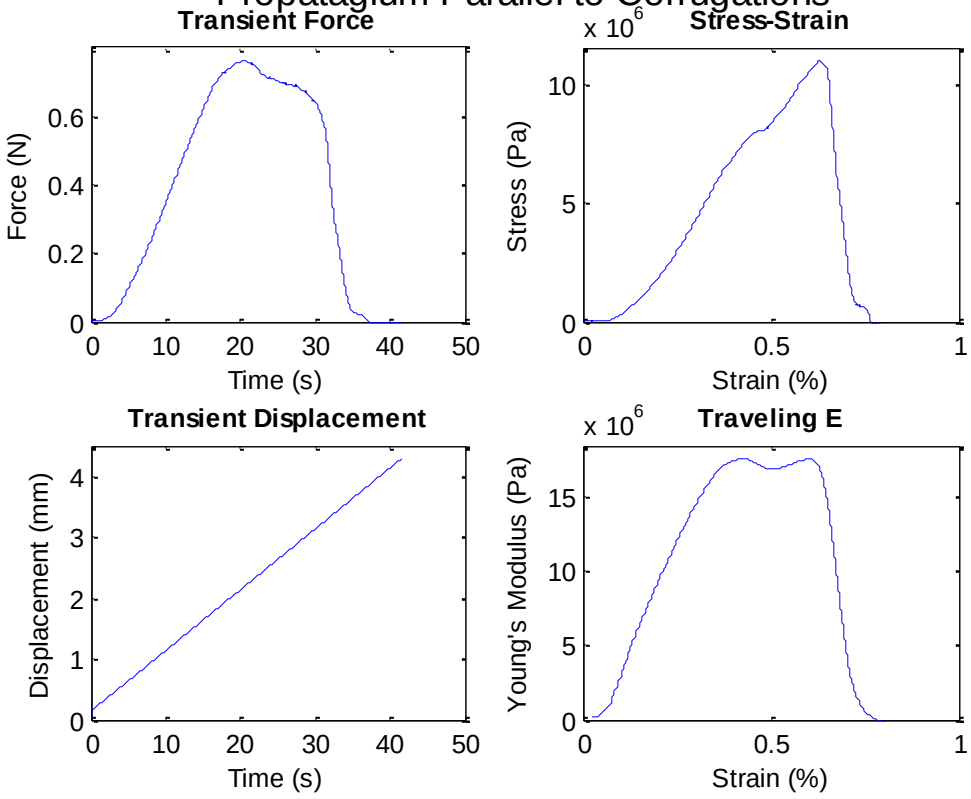

Plagiopatagium Parallel to Corrugations

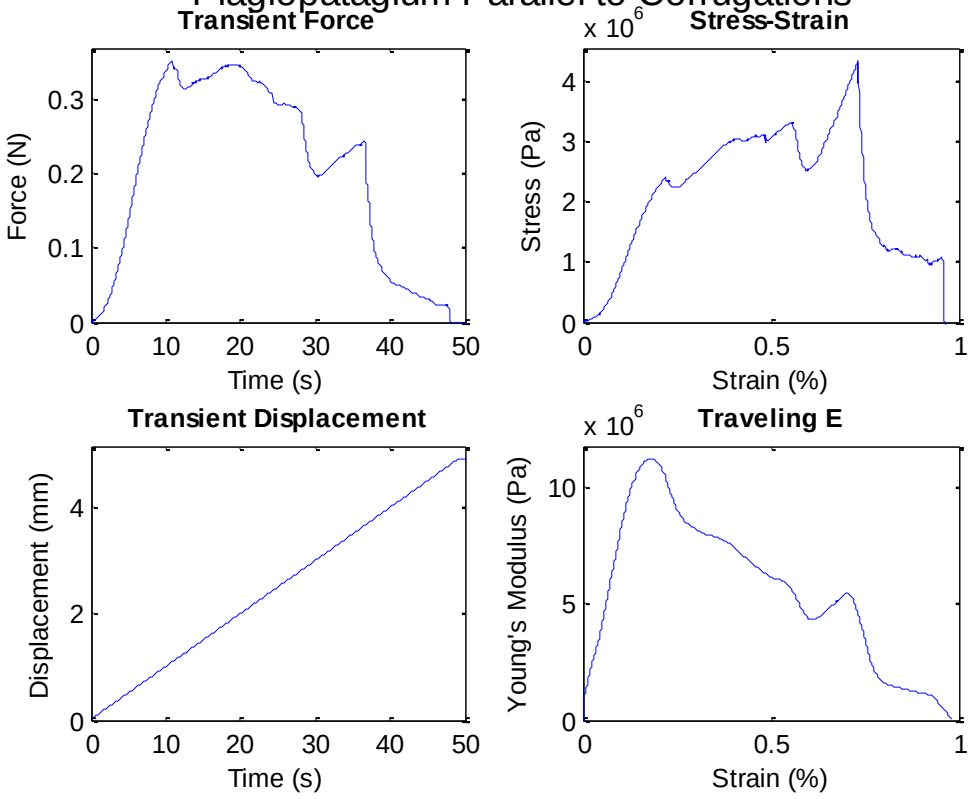

Uropatagium Parallel to Corrugations

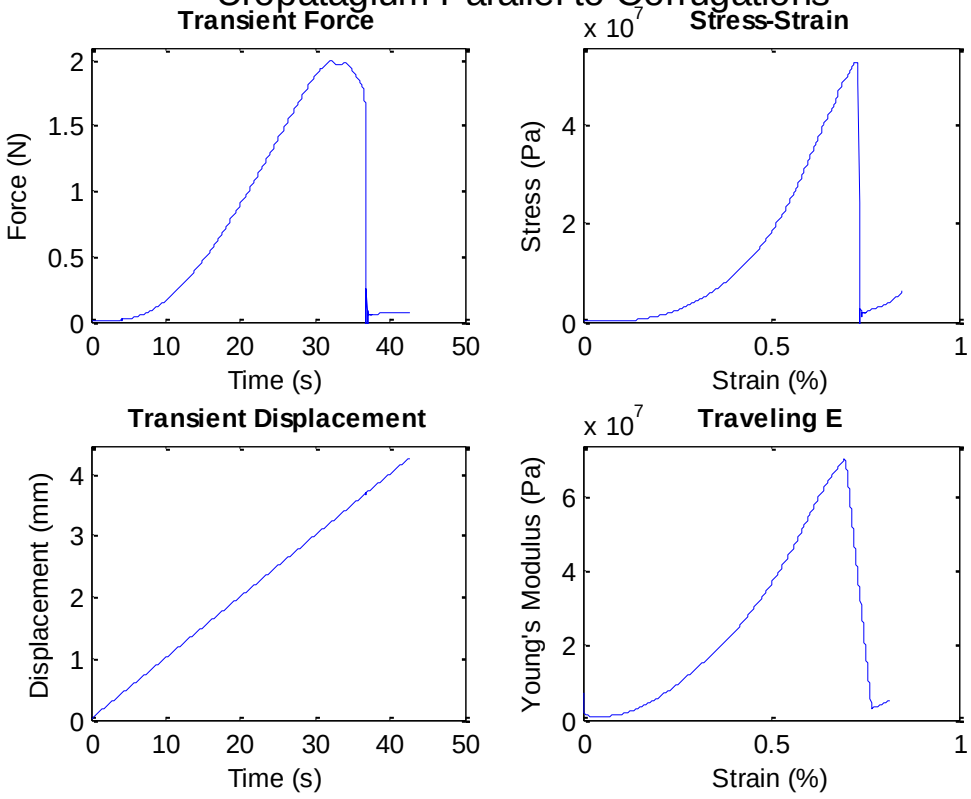

Appendix B: MATLAB image tracking of vehicle position

```
close all

% Read Video

video = mmreader('F5V.avi');

numframes = get(video,'NumberOfFrames')

TH = 0.423;
stp = 1;
skip = 10;


for i=1:stp:1

I = read(video,i);

% B = imrotate(I,90);    %Image rotation 90 degrees

% Image Convergion

gray_im_r = rgb2gray(I);
BW_im_r = im2bw(gray_im_r,TH);

% % MASK
% BW_im_r(1:480,1:411)=1;
% BW_im_r(1:480,449:640)=1;
%
% BW_im_r(1:239,1:640)=1;
% BW_im_r(264:480,1:640)=1;
%
for j=260:-1:235
    for k=456:-1:408
        if BW_im_r(j,k)==0
            movement(i)=k;
            k=407;
            j=234;
        end
    end
end

% figure
% imshow(gray_im_r);

 figure
 imshow(BW_im_r);


end
```

Appendix C: MATLAB code to plot vehicle position, velocity, and acceleration

```
close all;
t=0:.1:29.8;
% figure;
% plot(t,unfiltered,'r');
% hold;

amount = .085;

[b,a]=butter(2,amount);
movement5v_f=filter(b,a,movement5v(1:300));

[b,a]=butter(2,amount);
movement4v_f=filter(b,a,movement4v(1:300));

[b,a]=butter(2,amount);
movement3v_f=filter(b,a,movement3v(1:300));

% plot(t,filtered);


 movement5v_shifted=1:0:300;
for i=4:1:300
    movement5v_shifted(i)=movement5v(i-3);
end
movement5v_shifted(1:4)=0;

plot(time,(movement3v(1:300)/14)-30.40,'red');
hold on;
plot(time,(movement4v(1:300)/14)-30.36,'green');
plot(time,(movement5v_shifted(1:300)/14)-30.36,'blue');
axis([6, 22, -.4, .6]);
```

Appendix D: SEM of single PVDF fibers

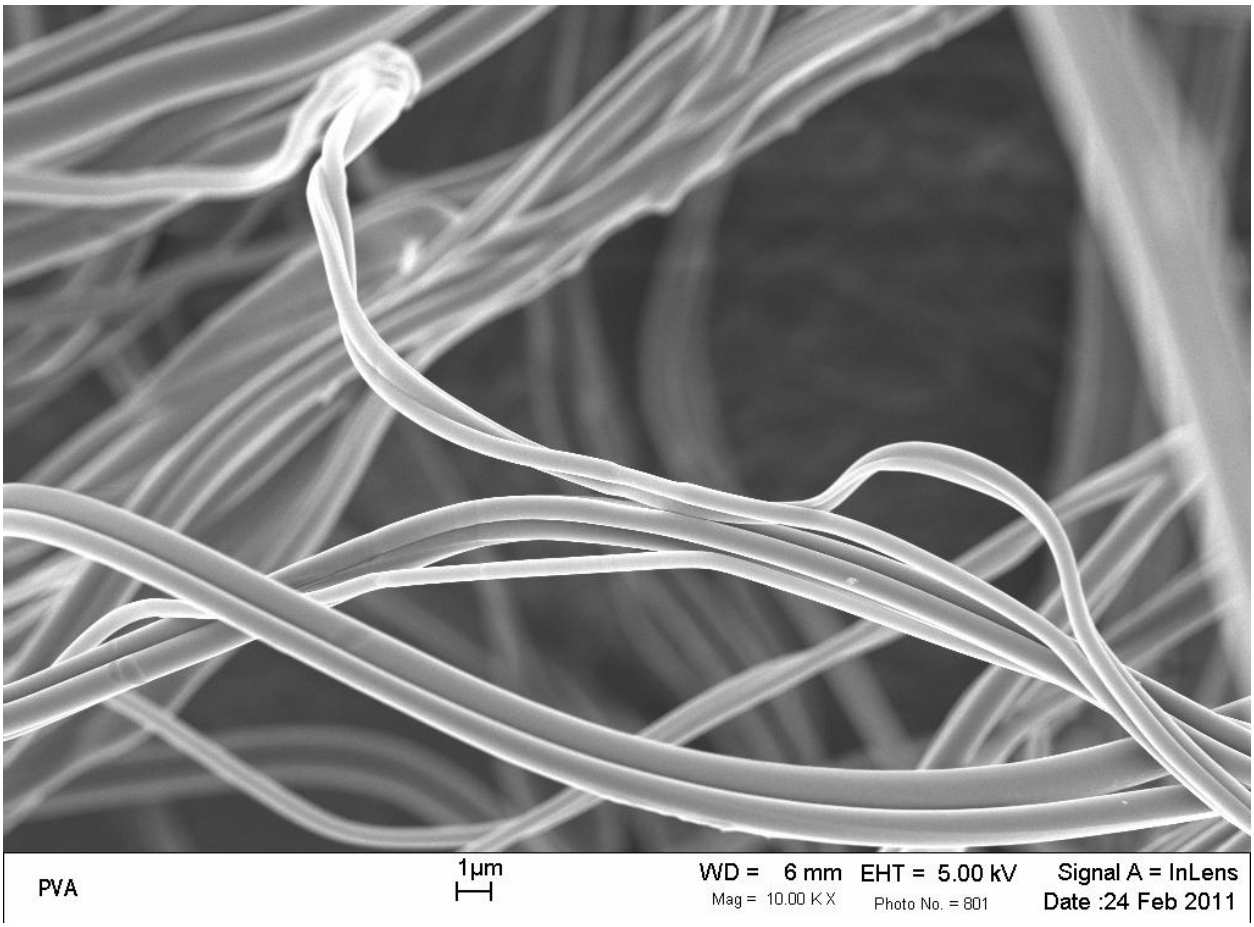

Appendix E: SEM of multiple PVDF fibers

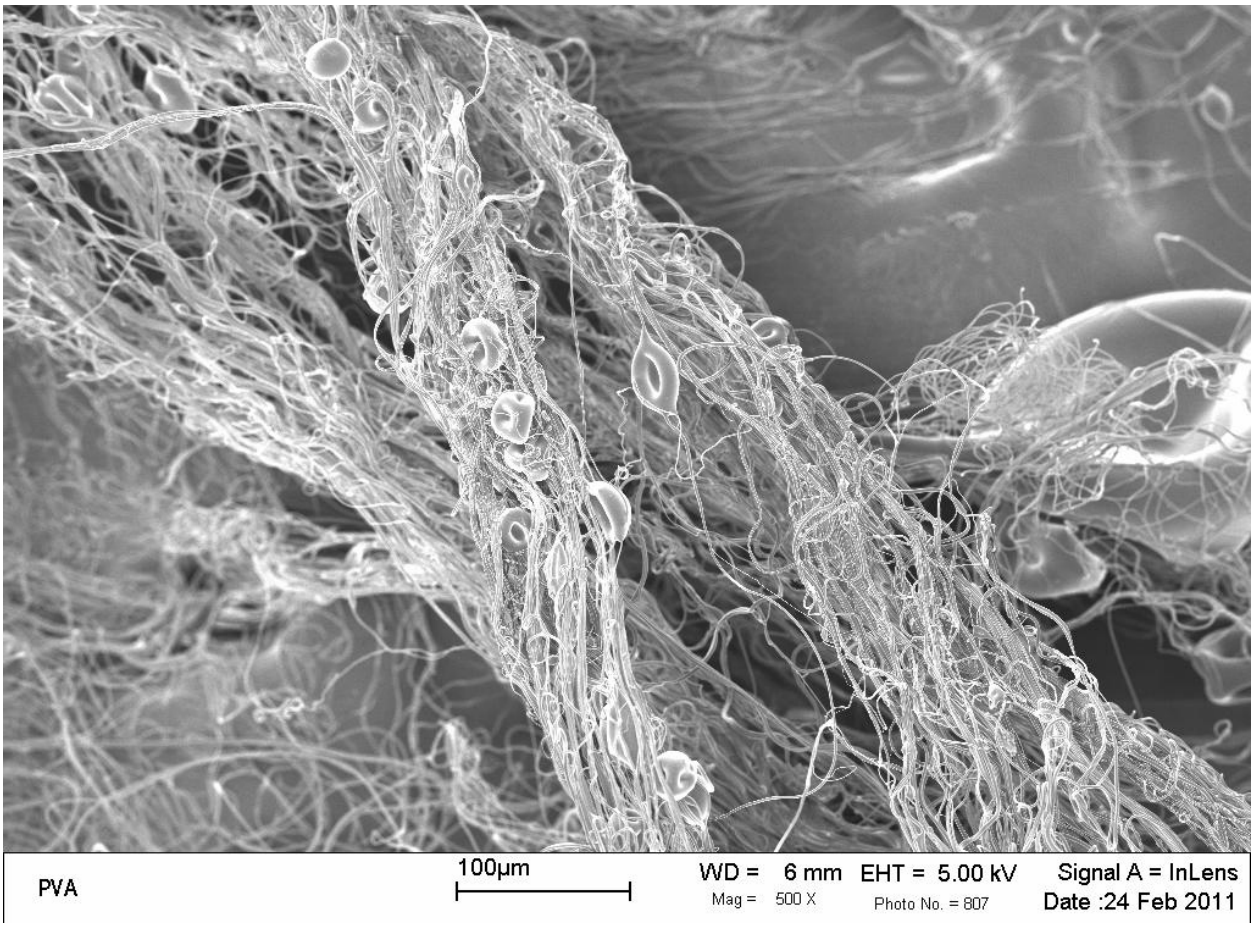

Appendix F: SEM of PVDF fibers forming a mat

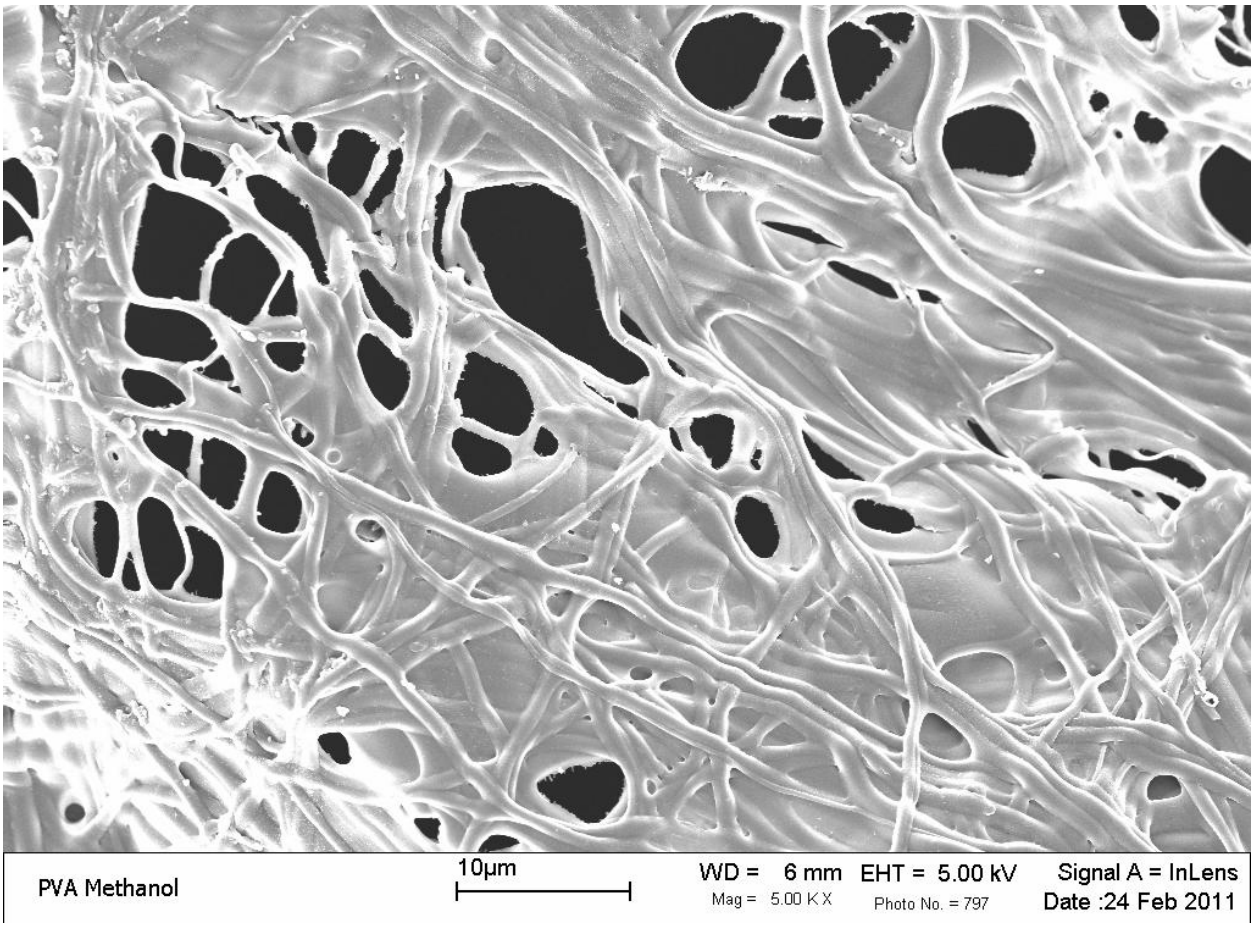

Appendix G: SEM of PVDF film showing pore size

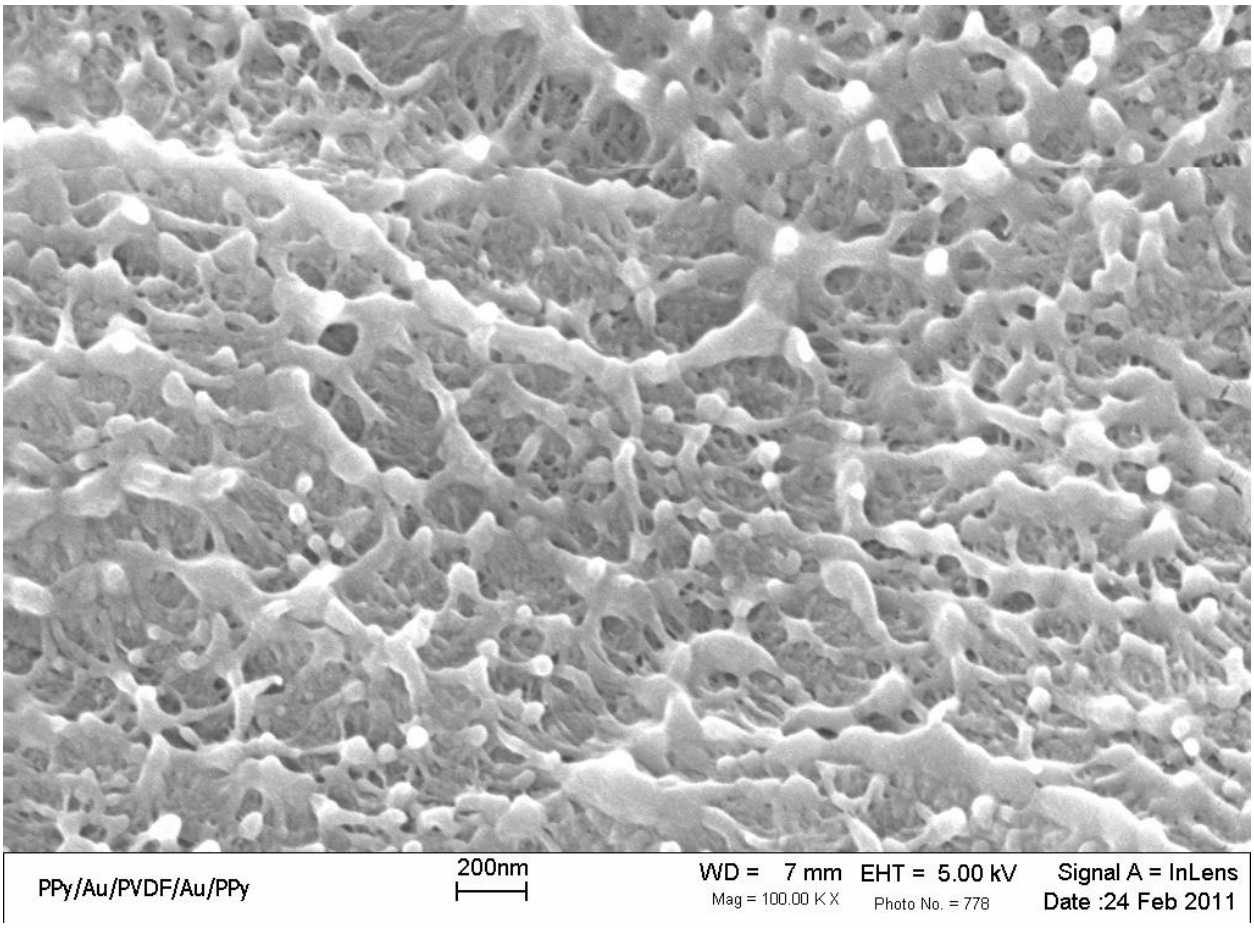

Appendix H: Photograph of PPy jellyfish testing setup

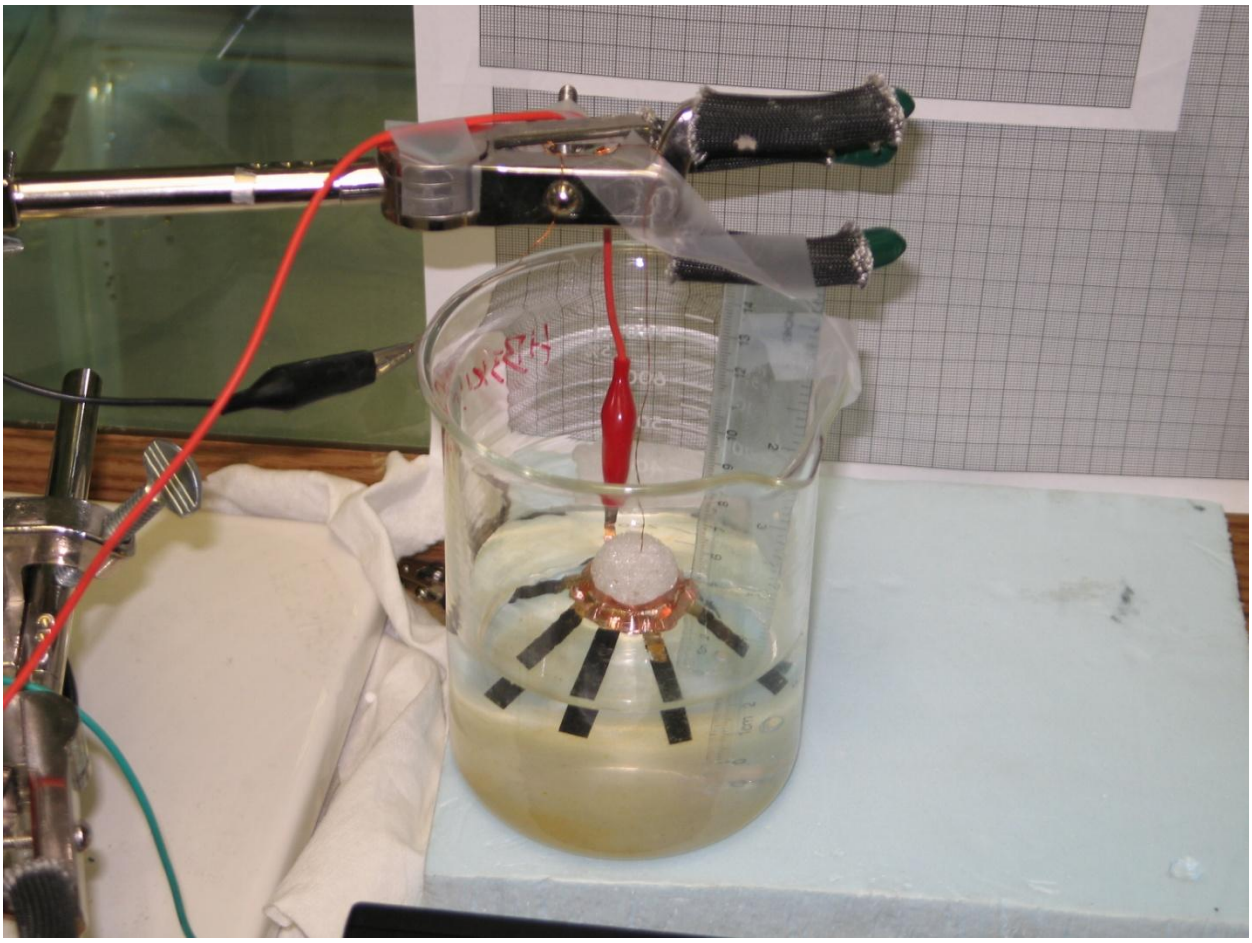

Appendix I: Photograph of PPy cyclic voltammetry setup

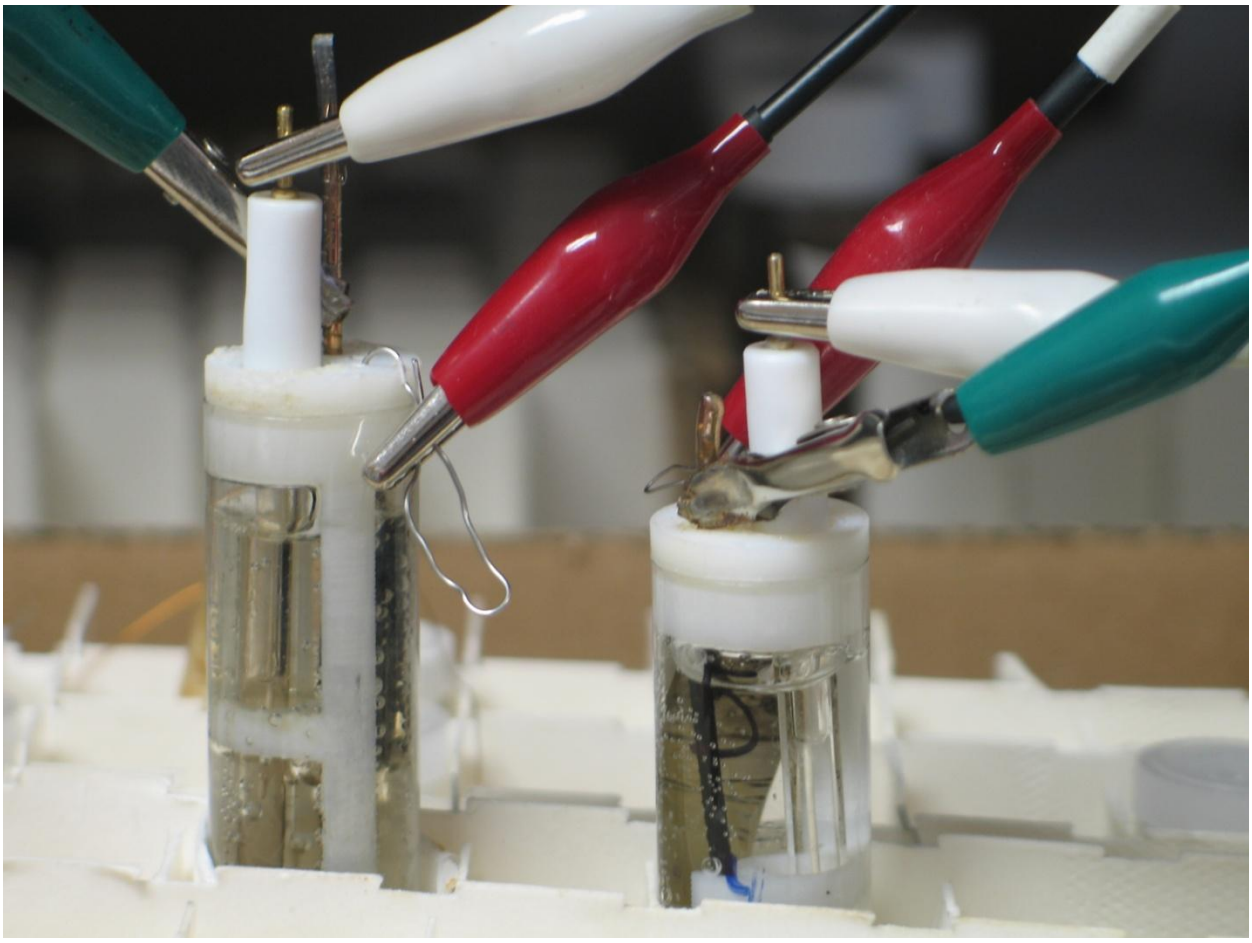

Appendix J: LabView code showing 3D representation of jellyfish vehicle

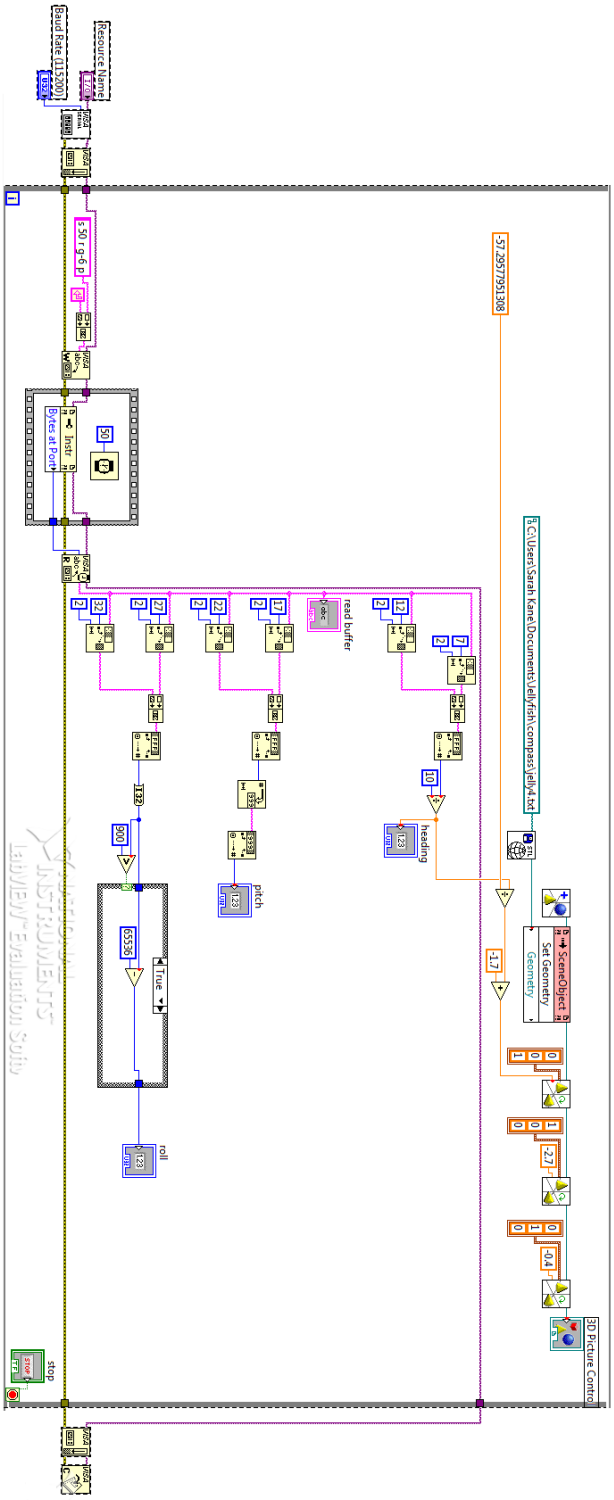

Appendix K: LabView front panel showing 3D representation of jellyfish vehicle

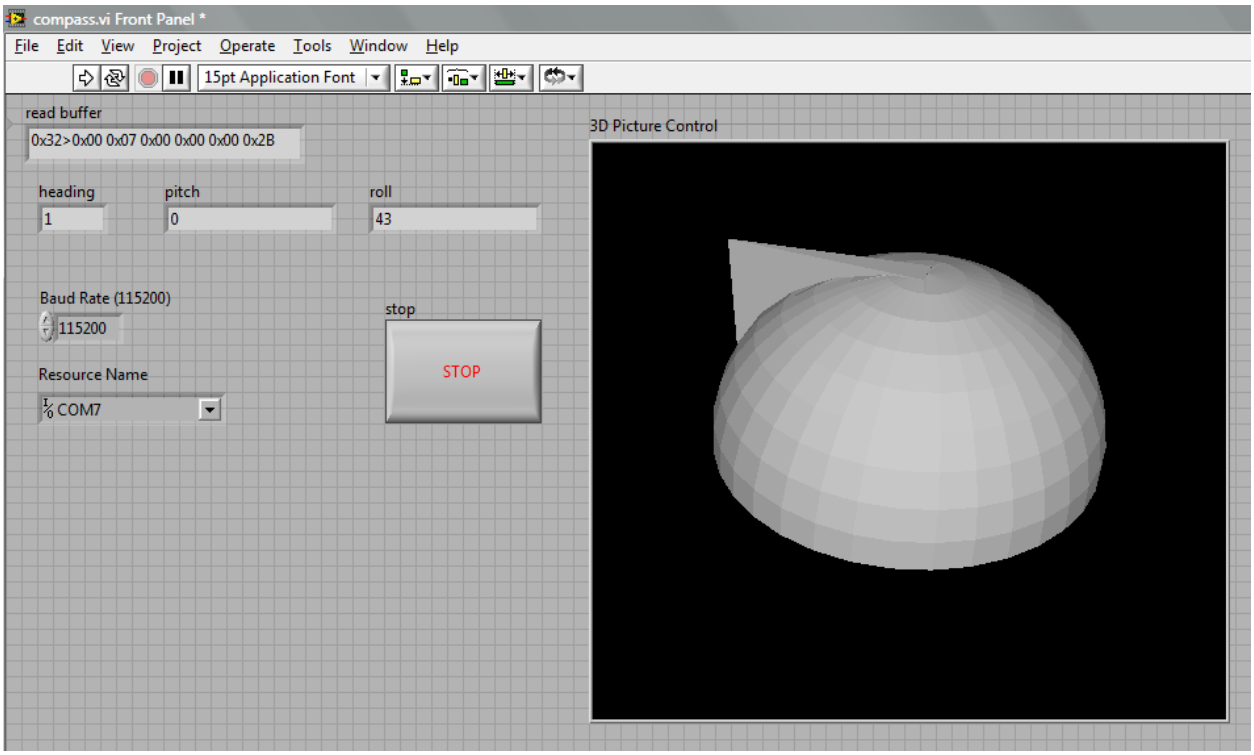

Appendix L: Circuit diagram of the power splitter

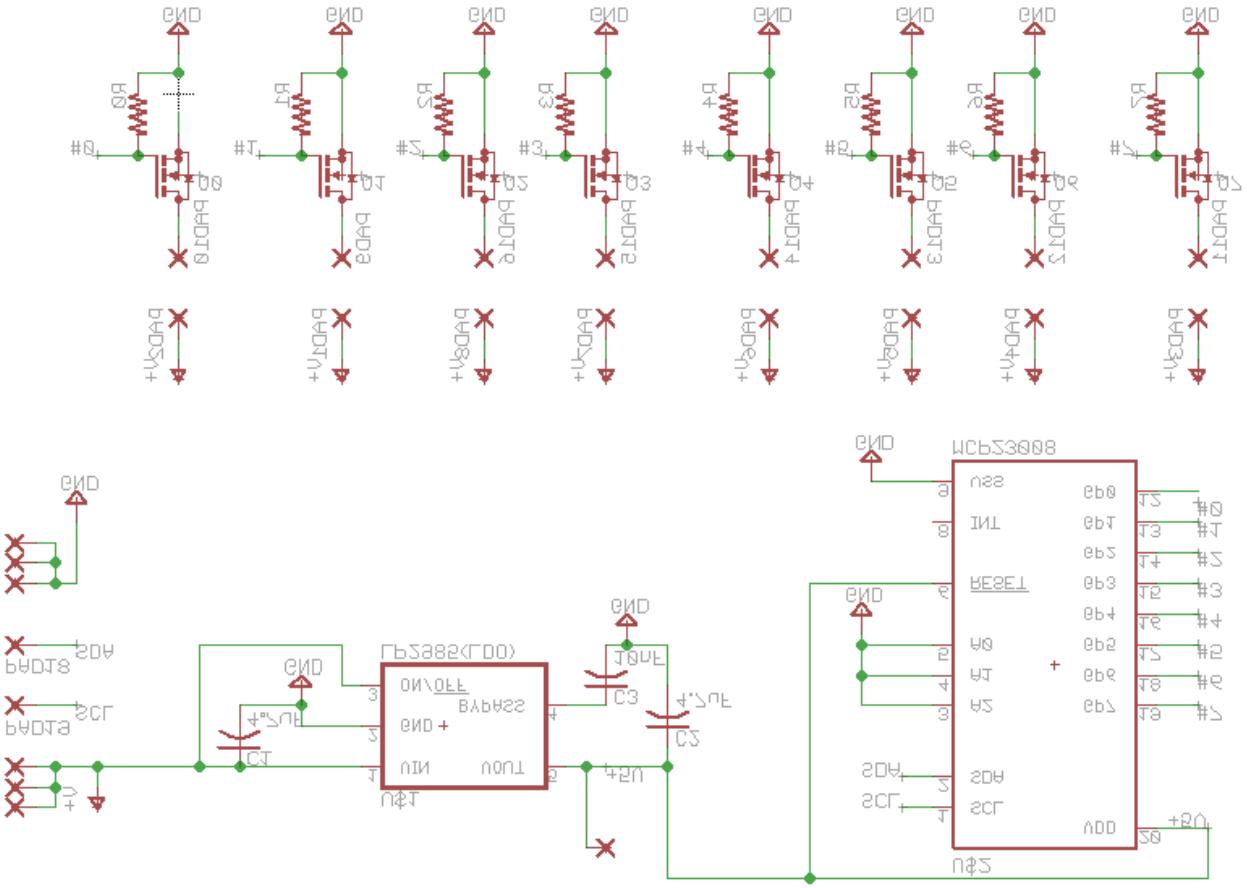

Appendix M: Circuit layout of the power splitter

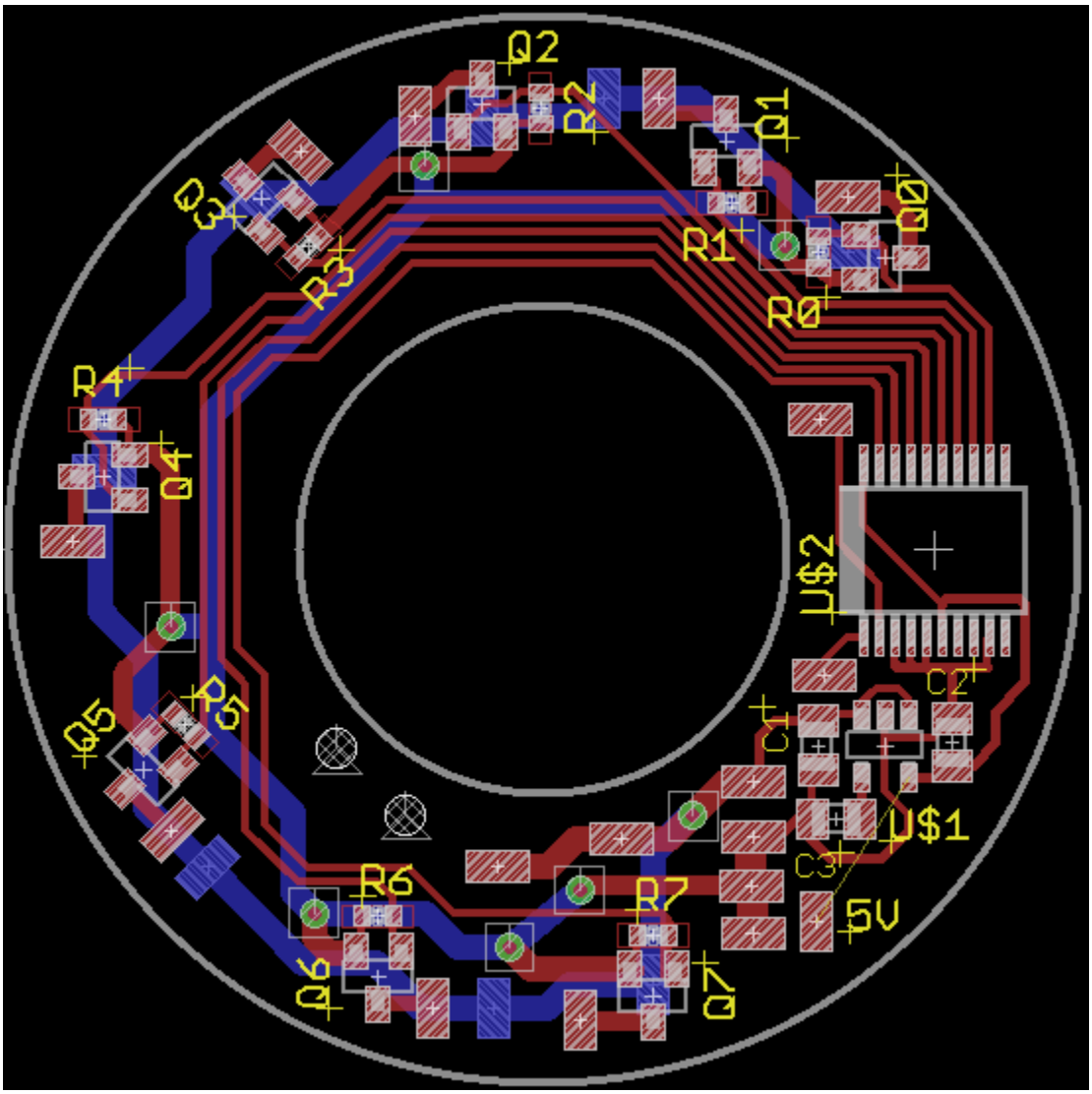

Appendix N: Cross-sections of the two-part jellyfish mold

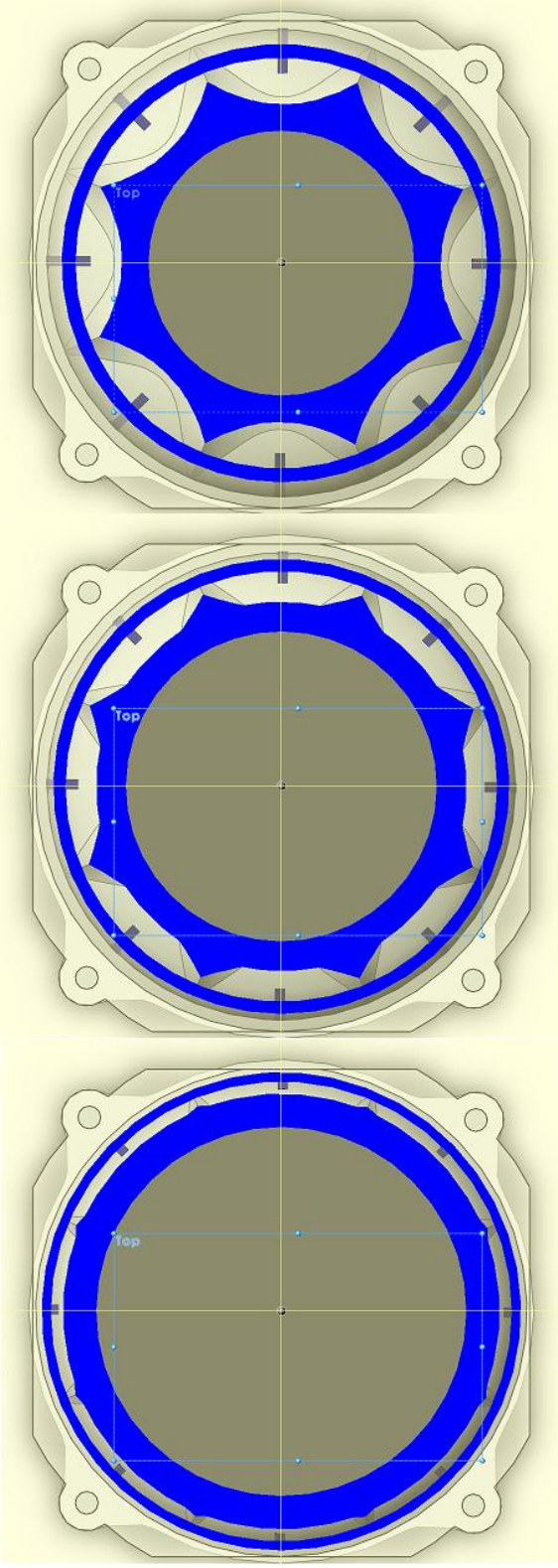

Appendix O: Photograph of side view of internal structure of jellyfish robot

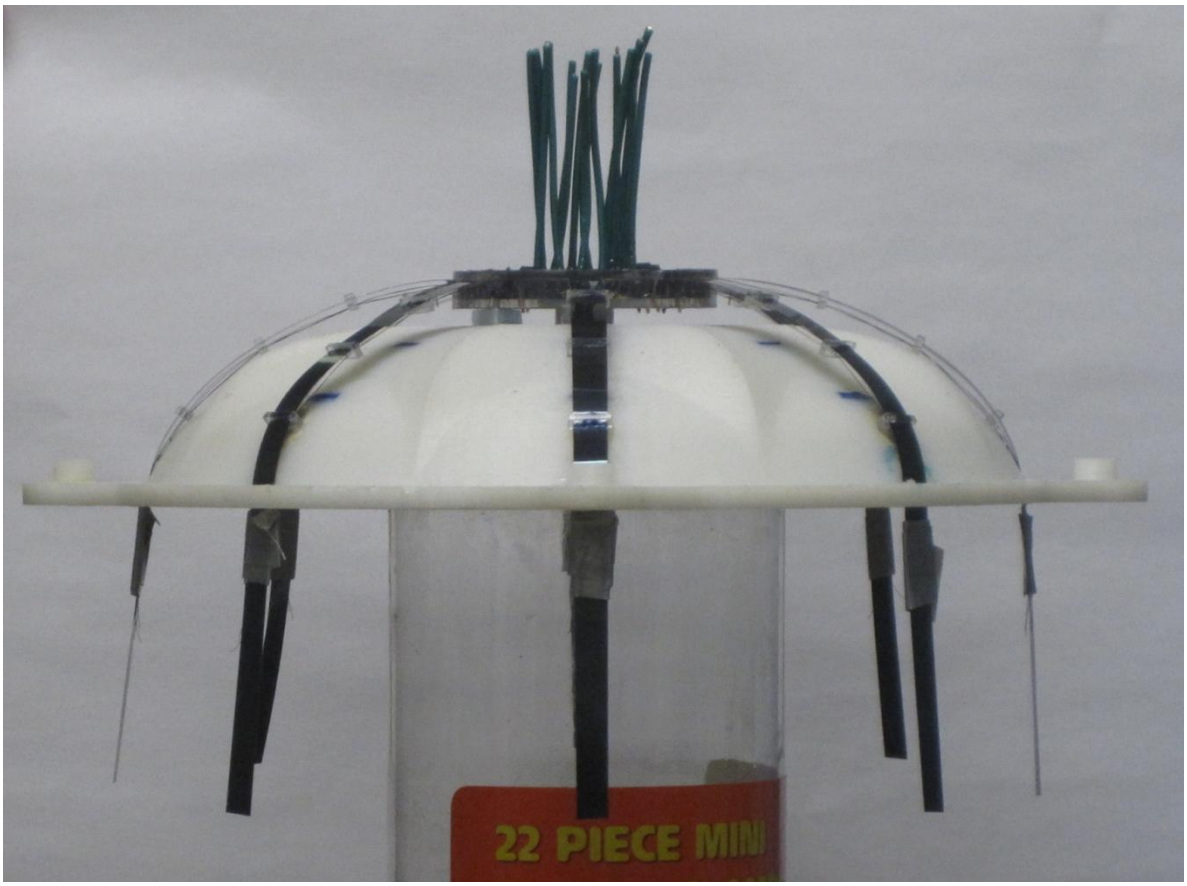

Appendix P: Mathematica script for joint geometry

$$\text{Manipulate}[\text{Plot}[\{-\frac{c(-3+x)}{c-x}, -\frac{c(-3-x)}{c+x}\}, \{x, -3,3\}, \text{AxesOrigin} \to \{0,0\}, \text{BaselinePosition} \to \text{Axis}, \text{PlotRange} \to \{0,3\}, \text{AspectRatio} \to .5, \text{Exclusions} \to \{c, -c\}, \text{ExclusionsStyle} \to \text{Red}], \{c, -4, -0.001\}]$$

$$\text{Manipulate}[\text{Plot}[\{\frac{c * j(k-x)}{c * k - j * x}, \frac{c * j(k+x)}{c * k - j * -x}\}, \{x, -3,3\}, \text{AxesOrigin} \to \{0,0\}, \text{BaselinePosition} \to \text{Axis}, \text{PlotRange} \to \{0,3\}, \text{ExclusionsStyle} \to \text{None}, \text{Exclusions} \to \{(k * c)/j\ , -(k * c)/j\}, \text{AspectRatio} \to .5, \text{PlotStyle} \to \{\text{AbsoluteThickness}[3]\}, \text{ImageSize} \to \{300,300\}], \{\{j, 3, \text{"Y} - \text{intercept"}\}, 0.001,3\}, \{\{k, 3, \text{"X} - \text{intercept"}\}, 0.001,3\}, \{\{c, -0.1, \text{"Curvature"}\}, -10, -0.01\}]$$

Appendix Q: Zoomed-out SEM of multiple *Aurelia* statoliths

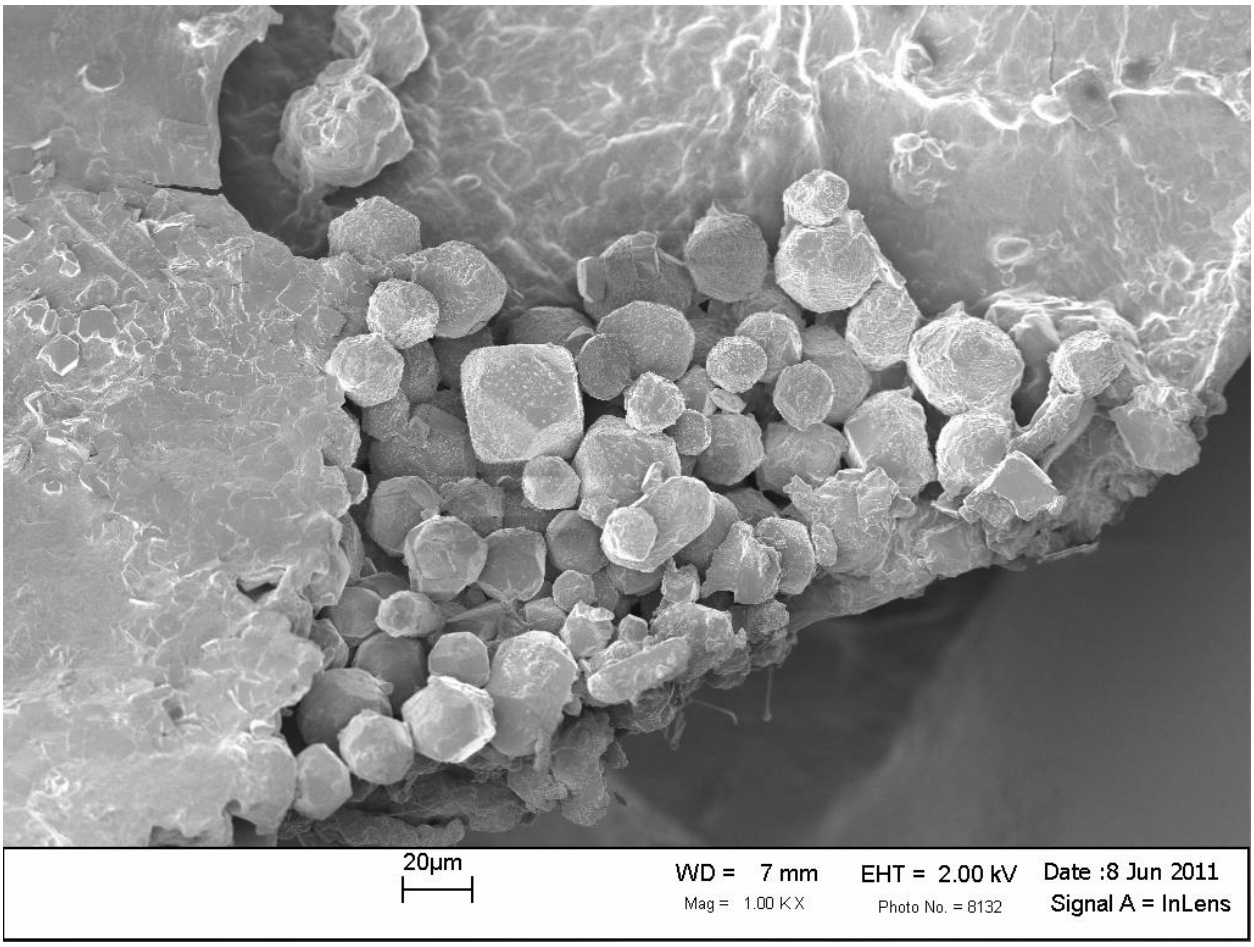

Appendix R: SEM image of probable nematocyst